

2001-09-01

## Development and Construction of a White Light Profiler for Industrial Applications

Martin Somers  
*Technological University Dublin*

Follow this and additional works at: <https://arrow.tudublin.ie/scienmas>



Part of the [Physics Commons](#)

---

### Recommended Citation

Somers, M. (2001). *Development and construction of a white light profiler for industrial applications*. Masters dissertation. Technological University Dublin. doi:10.21427/D7589X

This Theses, Masters is brought to you for free and open access by the Science at ARROW@TU Dublin. It has been accepted for inclusion in Masters by an authorized administrator of ARROW@TU Dublin. For more information, please contact [arrow.admin@tudublin.ie](mailto:arrow.admin@tudublin.ie), [aisling.coyne@tudublin.ie](mailto:aisling.coyne@tudublin.ie), [vera.kilshaw@tudublin.ie](mailto:vera.kilshaw@tudublin.ie).

DEVELOPMENT AND CONSTRUCTION  
OF A  
WHITE LIGHT PROFILER  
FOR  
INDUSTRIAL APPLICATIONS

by  
Martin Somers B.Sc.

A thesis submitted for the degree of Master of Philosophy to the School of Physics  
Dublin Institute of Technology

Supervisor: Dr. Brian Bowe

September 2001

### **Declaration of Originality**

I certify that this thesis which I now submit for the examination for the award of Master of Philosophy is entirely my own work and has not been taken from the work of others save and to the extent that such work has been cited and acknowledged within the text of my work.

This thesis was prepared according to the regulations for postgraduate study by research of the Dublin Institute of Technology and has not been submitted in whole or in part for an award in any other Institute or University.

The Institute has the permission to keep, to lend or to copy this thesis in whole or in part, on condition that any such use of the material of the thesis be duly acknowledged.

Signature Martin Somers Date: 8/10/22

**Martin Somers**

## Acknowledgements

With so many people to thank writing such a small segment won't do justice to those that have contributed in any small way in helping me complete this thesis. First and foremost I would like to thank my supervisor Dr. Brian Bowe for his constant support and motivation in getting me to the finish line. I am eternally grateful also to the help given by Dr. Vincent Toal and Dr. Suzanne Martin in completing on time.

I would also like to thank my research colleagues both past and present for their constructive input into the project and special thanks must go to Mr. Michael O' Hora for proof reading and Mr. Gavin King for their encouragement.

I would also like to thank the staff of the School of Physics who would always lend a hand in helping out, in particular to Mr. Joe Keogh. Also thanks to Mr. James Callis who was always able to iron out all those computer problems that I had. Also thanks must go to Ms. Linda Moore for allowing me the time to profile the contact lens that she is working on.

Finally I would like to thank my family and friends.....

# Development and Construction of a White Light Profiler for Industrial Applications

by

Martin Somers

## Abstract

With the ever decreasing tolerances in modern manufacturing processes it has become more important to define surface topography measurements quickly and accurately. Though contact methods, using the stylus probe, have been used for a long time more optical techniques are being brought into the market place. The advantages in using optical methods is obvious; no contact with the surface eliminates damage due to a probing tip and also the surface may be scanned in a matter of seconds. Optical techniques also have the advantage that a full field of view may be acquired, unlike point measurement where the surface must be scanned many times to build up a 3 dimensional view of the surface.

This thesis is concerned with the work carried out in the design and construction of a portable, low cost non-contact profiler that is based on the analysis of interference fringe patterns produced by a Michelson interferometric setup. One system has been designed with the incorporation of two LabVIEW programs, with one program having the capability of profiling discontinuous smooth surfaces and the other having the capability of profiling smooth continuous surfaces.

The algorithm used for profiling discontinuous smooth surfaces is based on the degree of mutual coherence that exists between two interacting beams. It analyses the visibility of the interference fringes to obtain a 3 dimensional profile of the surface. The second algorithm is based on phase shifting interferometry and uses a minimum of four intensity frames to calculate the relative phase difference of the two interfering beams. By calculating the phase difference of the two beams in the interferometer it is possible to extract the surface height of the sample.

The profiler has a field of view of  $3 \text{ mm}^2$ , a lateral or spatial resolution of approximately  $4 \mu\text{m}$  with a vertical resolution between  $5 \text{ nm}$  and  $0.06 \mu\text{m}$  depending on the algorithm being used to acquire a profile. The design process and algorithms will be explained in greater detail in the proceeding chapters, also the limitations and advantages of the system will be discussed.

## Objectives

From earlier it is seen that the main objective of this thesis is the design and construction of a system that integrates hardware and software in the construction of a white light profiling system. For the system to have real industrial applications both software and hardware must seamlessly work in tandem in order for the user to be efficient in the operation of the instrument. Therefore all aspects of the design of the program must be intuitive to the user, many of the systems operations must be computer controlled including the gathering and processing of data from the camera, the control of the DC motor and the control of the voltage source for the piezo-electric transducer. Further information on these routines will be discussed in further detail later in the thesis.

The objectives in the construction of a profiler would include a system that is portable, costs less than €10000 to construct and has a maximum working range achievable while also maximising the field of view of the camera. The main concern with this approach is that as the working range is decreased the field of view increases thus there is an increase in the lateral resolution achieved. Therefore there is a limit to the maximum attainable working distance for a set field of view. Ideally the system constructed should have a large working range of approximately 100 mm and a lateral resolution of approximately 1  $\mu\text{m}$ .

Initially a test system will be constructed and the software tested to ensure that the developed code is efficient and free of errors. Once this is complete it is hoped that it may be possible to maximize the field of view while maintaining a low lateral resolution.

## Table of Contents

<b>CHAPTER 1: BACKGROUND THEORY</b>	<b>7</b>
1.1 Introduction	7
1.2 The Superposition of Waves	8
1.3 Young's Slits Experiment	14
1.4 Michelson Interferometer	16
1.5 White Light Fringes	19
<b>CHAPTER 2: METROLOGY METHOD</b>	<b>21</b>
2.1 Surface Profiling	21
2.1.1 Contact versus Non-contact methods	21
2.1.2 Scanning Tunnelling Microscope and Atomic Force Microscope	22
2.2 Interferometric Method	23
2.2.1 Phase Shifting Interferometer	25
2.2.2 Vertical Scanning or Coherence Peak Detection	27
2.2.3 Fourier Analysis	28
2.2.4 Digital Signal Processing	29
2.2.5 White light Phase Shifting	30
2.3 Optical Stylus	30
2.4 Moiré Fringes	31
2.5 Other Surface Profiling Methods	32
2.6 Optical Configuration for Interferometric Microscopes	33
<b>CHAPTER 3: PHASE-MEASUREMENT INTERFEROMETRY</b>	<b>36</b>
3.1 Introduction	36
3.2 Means of Phase Shifting	37
3.3 Four Bucket Algorithm Derivation	39
3.4 Optical Path Difference Techniques	41
3.5 Algorithm Performance and Selection	43
3.6 Removal of phase ambiguities	46

3.6.1 Phase unwrapping	47
3.7 Phase-Shifter Calibration	49
3.8 Phase Shifting using White Light	50
<b>CHAPTER 4: DEVELOPMENT OF WHITE LIGHT PROFILOMETER.</b>	<b>52</b>
4.1 Optical setup	52
4.2 Algorithms	55
4.2.1 Coherence Peak Detection	58
4.3 Results	61
4.3.1 Optical Steps	63
4.3.2 Silica Steps	65
<b>CHAPTER 5: PHASE STEPPING INTERFEROMETRY</b>	<b>72</b>
5.1 Introduction	72
5.2 PZT Calibration	72
5.3 Calibration Program Design	73
5.3.1 Program No. 1: Voltage Calibration Fringe Detection	74
5.3.2 Program No. 2: Voltage Calibration Peak Detection	76
5.3.3 Program No. 3: Voltage Calibration Fringe Subtraction	77
5.4 Phase Stepping Results	81
5.5 Contact Lens	84
<b>CHAPTER 6: DESIGN OF THE USER INTERFACE</b>	<b>87</b>
<b>CHAPTER 7: CONCLUSIONS</b>	<b>99</b>
<b>REFERENCES</b>	<b>101</b>
<b>APPENDIX A- EQUIPMENT</b>	<b>106</b>



## CHAPTER 1: BACKGROUND THEORY

### 1.1 Introduction

The motivation for this research is to harness the phenomena of interference in the development of a surface profiler using interferometric methods. In explaining how such methods may be used in the construction of a profile it is first necessary to give some background information on the interaction of light and the mathematics involved, this will be discussed in greater detail further on in this chapter. Also outlined is a brief history of the area of interference and the early pioneers who gathered so much valuable information and made some landmark discoveries.

The nature of light had been an enigma to scientists until the middle of the 17th century when James Clerk Maxwell formulated the four equations that defined both electricity and magnetism and brought them together to form Maxwell's equations<sup>1</sup>. The end result is called the wave equation and can be seen in its one dimensional form equation 1.1

$$\frac{\partial^2 \psi}{\partial x^2} = \frac{1}{c^2} \frac{\partial^2 \psi}{\partial t^2} \quad (1.1)$$

The equations define light as an electromagnetic wave travelling along the x-axis that has a coupled electric and magnetic field fluctuating perpendicular to the direction of propagation, where  $c$  is the speed of propagation. The speed of the waveform may be written as an expression of the wavelength  $\lambda$  and frequency  $\nu$  of the source.

$$c = \nu\lambda$$

Where  $c$  is a constant for all wavelengths in the visible region, and in a vacuum has a value of:

$$2.997925 \times 10^8 \text{ ms}^{-1}$$

with  $\lambda$  written in nanometres, where  $1\text{nm} = 10^{-9} \text{ m}$ ; although the micrometer ( $1\mu\text{m} = 10^{-6} \text{ m}$ ) is often used while the old form of angstrom ( $1\text{\AA} = 10^{-10} \text{ m}$ ) can be found in texts. The wavelength of visible light is between 400nm and about 700nm of the spectrum.

As of yet, due to the high frequency ( $\sim 5 \times 10^{14} \text{ Hz}$ ) of the E field of the visible region it is impossible to measure the optical disturbance directly. It is been shown that irradiance is proportional to the square of the amplitude of the E-field<sup>1</sup> as in equation (1.2)

$$I = \frac{c\epsilon_0}{2} E^2 \quad (1.2)$$

Though it is not possible to measure the E field directly it is possible to find the intensity of the light falling on a surface using a photo sensor. By determining the intensity of light falling on a unit of area it is possible to calculate the electric field of the light.

## 1.2 The Superposition of Waves

Following on from Maxwell's one-dimensional wave equation 1.1, a solution to the wave equation that is both differentiable with respect to both  $x$  and  $t$  is shown below equation (1.3.)

$$\psi(x,t) = A \sin(kx - \omega t)$$

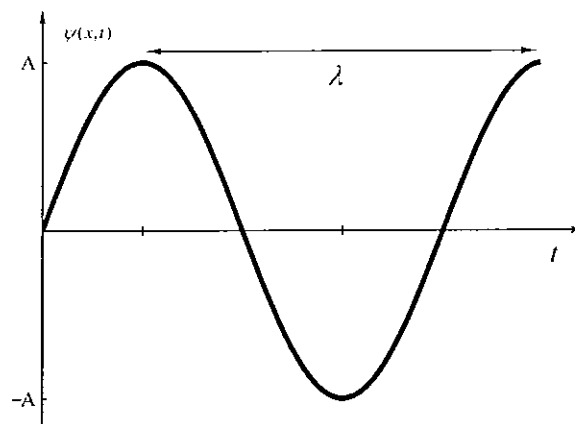


Fig 1.1. 1-D profile of an electromagnetic wave.

In equation 1.3  $A$  is the amplitude,  $k$  the propagation constant and  $\omega$  the angular frequency of the wave. The form of the wave equation in equation 1.1 reveals an appealing property of waves over that of a stream of particles. Suppose that two wavefunctions  $\psi_1$  and  $\psi_2$  are solutions to the wave equation, then it is reasonable to assume that  $(\psi_1 + \psi_2)$  is also a

solution. This is known as the Principle of Superposition and states that the resultant disturbance at any point in a medium is the algebraic sum of the separate constituent waves. This can be easily shown as follows.

$$\frac{\partial^2 \psi_1}{\partial x^2} = \frac{1}{v^2} \frac{\partial^2 \psi_1}{\partial t^2} \quad \text{And} \quad \frac{\partial^2 \psi_2}{\partial x^2} = \frac{1}{v^2} \frac{\partial^2 \psi_2}{\partial t^2}$$

$$\frac{\partial^2 \psi_1}{\partial x^2} + \frac{\partial^2 \psi_2}{\partial x^2} = \frac{1}{v^2} \frac{\partial^2 \psi_1}{\partial t^2} + \frac{1}{v^2} \frac{\partial^2 \psi_2}{\partial t^2}$$

$$\frac{\partial^2}{\partial x^2} (\psi_1 + \psi_2) = \frac{1}{v^2} \frac{\partial^2}{\partial t^2} (\psi_1 + \psi_2)$$

Since the general equation of wave motion is a linear equation, the sum of any number of solutions is also a solution to the wave equation. If this were not the case the principle of superposition would need to be modified. When two sets of waves interact with each other interesting and complicated effects may be observed. This interaction has come to be known as interference. It is important to note that as the beams interact, the propagation of one is completely unaffected by that of the other. One example of interference in nature is the result of dropping two stones into a pond. It can be seen that there are regions in which the disturbance of the water is greater than either of the original waves while in other regions the disturbance is practically zero.

As previously mentioned light is an electromagnetic wave with a sinusoidal profile. If two interacting waves that have the same frequency and amplitude with no phase difference between them are superimposed on one another, the problem can be resolved to a particle undergoing two simple harmonic motions at the same time. Note that displacement due to the waves will take place in the y direction and the terms  $a_1$  and  $a_2$  are the individual amplitudes of the interacting waves. The two waves  $y_1$  and  $y_2$  are described by equation 1.4.

$$y_1 = a_1 \sin(\omega t - \alpha_1)$$

$$y_2 = a_2 \sin(\omega t - \alpha_2)$$
(1.4)

Since both waves have the same frequency,  $\omega$  is the same in both cases. The resultant displacement  $y$  therefore is the sum of  $y_1$  and  $y_2$ , from the principle of superposition.

$$y = a_1 \sin(\omega t - \alpha_1) + a_2 \sin(\omega t - \alpha_2) \quad (1.5)$$

From the addition of two sine functions the expression of equation 1.5 is rewritten.

$$\begin{aligned} y &= a_1 \sin \omega t \cos \alpha_1 - a_1 \cos \omega t \sin \alpha_1 + a_2 \sin \omega t \cos \alpha_2 - a_2 \cos \omega t \sin \alpha_2 \\ &= (a_1 \cos \alpha_1 + a_2 \cos \alpha_2) \sin \omega t - (a_1 \sin \alpha_1 + a_2 \sin \alpha_2) \cos \omega t \end{aligned} \quad (1.6)$$

$a_1$  and  $\omega$  are constants and so equation 1.6 can be rewritten as:

$$\begin{aligned} a_1 \cos \alpha_1 + a_2 \cos \alpha_2 &= A \cos \theta \\ a_1 \sin \alpha_1 + a_2 \sin \alpha_2 &= A \sin \theta \end{aligned} \quad (1.7)$$

By squaring both sides of equation (1.7)

$$\begin{aligned} A^2 &= \cos^2 \theta + \sin^2 \theta = a_1^2 (\cos^2 \alpha_1 + \sin^2 \alpha_1) + a_2^2 (\cos^2 \alpha_2 + \sin^2 \alpha_2) \\ &\quad + 2a_1 a_2 (\cos \alpha_1 \cos \alpha_2 + \sin \alpha_1 \sin \alpha_2) \end{aligned} \quad (1.8)$$

$$A^2 = a_1^2 + a_2^2 + 2a_1 a_2 \cos(\alpha_1 - \alpha_2) \quad (1.9)$$

$$\tan \theta = \frac{a_1 \sin \alpha_1 + a_2 \sin \alpha_2}{a_1 \cos \alpha_1 + a_2 \cos \alpha_2} \quad (1.10)$$

Both equations (1.9) and (1.10) show that the values of  $A$  and  $\theta$  satisfy equation (1.7). Substituting equation (1.7) into equation (1.5)

$$y = A \cos \theta \sin \omega t - A \sin \theta \cos \omega t \quad (1.11)$$

Equation 1.11 can be further reduced to:

$$y = A \sin(\omega t - \theta) \quad (1.12)$$

From the resultant waveform we see that it has the same form of the two original waves equation (1.4), but contains a new amplitude  $A$  and a new phase constant  $\theta$ . This is an important observation as it shows that the resultant of two simple harmonic motions with the same frequency results in another simple harmonic motion of the same frequency. From electromagnetic theory, the intensity of a wave is proportional to the square of the electric field of the light wave, equation (1.2). To calculate the intensity of the resultant waveform, we look at equation (1.9). It is seen that the new intensity depends on the sum of  $a_1$  and  $a_2$  of the original waves and on the additional contribution  $2a_1a_2\text{Cos}(\alpha_1 + \alpha_2)$  called the interference term. When two beams of light are brought together the intensity of the light at any point is proportional to the square of the resultant amplitude. If we assume that the amplitude of the waves to be the same  $a_1 = a_2$ , as in the arms of a Michelson interferometer<sup>1</sup>, and the phase difference ( $\alpha_1 - \alpha_2 = \delta$ ). Then the intensity of the resultant wave any point is given as follows:

$$I \approx A^2 = 2a^2(1 + \text{Cos}\delta) = 4a^2\text{Cos}^2\frac{\delta}{2} \quad (1.13)$$

If the assumption is made that both intensities are equal and the phase difference  $\delta = \pi$ , the resultant intensity would be zero. At first glance this would seem to violate the principle of the conservation of energy. But on closer inspection of equation (1.13), there are intensity values that are less than the sum of the separate intensities and also there are other intensity values that are greater than the sum of the separate intensities. Therefore the resultant intensity produced by two interfering beams depends on the phase difference at any particular point on the waves as shown figure 1.2.

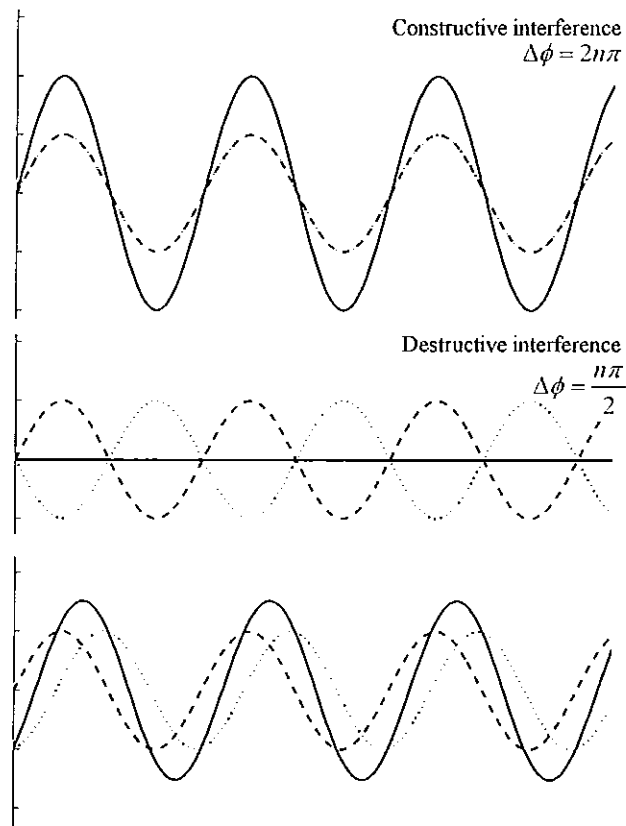
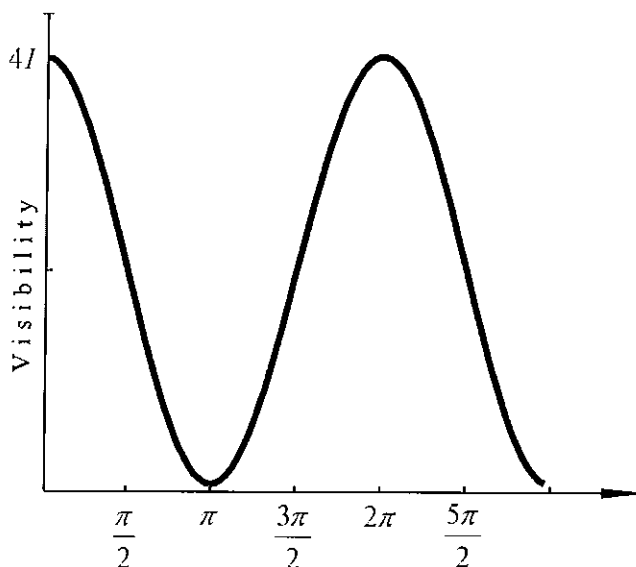


Fig 1.2 Waves undergoing constructive and destructive interference.

From figure 1.2 the diagrams show waves that are both in phase  $\delta = 2n\pi$  and out of phase with each other i.e.  $\delta = n\pi/2$ . Notice how waves that are in phase tend to amplify their parent signals while waves out of phase diminish their original signal.

From the previous discussion, when two waves of the same frequency are superimposed on one another they may not be in phase but the phase difference between them is constant, the resultant intensity of the interacting waves may be given by equation 1.9. Though usually more than two waves are interacting at single point in space. As the waves interfere in space the generated intensity pattern may be perceived in the spatial plane as bands of alternating bright and dark regions that are more commonly known as interference fringes. The intensity in the region of superposition varies from point to point between a maxima which may exceed the sum of the intensities, and minima which may be zero. From figure 1.3 it is seen that the intensity is dependant on the phase difference between the interacting waves. When the phase difference is  $\delta = 2n$ , where  $n=0,1,2,3,\dots$ , the intensity is four times that of the original wave, and is termed constructive interference. If  $\delta = (2n + 1)\pi$ ,

$n=0,1,2,3\dots$  the intensity is zero, and destructive interference is said to have occurred figure 1.3.



**Fig. 1.3 Plot of fringe visibility against phase.**

One important consideration in the interference phenomena is the coherence length of the light source. In general a light source emits a wave of finite length due to the excitation of the atoms at the surface with the emission of a photon. This photon emission from the surface is a random process. If the phase variation of the emitting photons is not constant the source is said to be incoherent, though if all emitted photons from the surface of the source have a constant phase variation the source is said to be coherent. The duration that the phase difference of emerging photons remains constant from the source is known as the coherence time.

As stated when two beams interact an intensity distribution may be produced, though this is only possible when the optical path difference between the two beams is less than the coherence length of the light source used, where the coherence length is the distance light travel during the coherence time.

This is the reason why no interference may be observed for two independent filament light sources set side by side. The instantaneous intensity that is seen is given by equation 1.9 and the sudden changes in phase occurring in very short intervals  $\approx 10^{-8}$  seconds. Interference fringes may exist but due to the fact that the phase changes so quickly, the fringes will also

change position. The eye and optical sensors are unable to detect such variations as the intensity is averaged over a finite duration of less than a millisecond, with the result that no fringes may be seen.

It was not until 1960 that an independent coherent light source was developed based on the ruby crystal. Early ruby lasers had a coherence length of approximately 5 mm but now lasers can have a coherence length of several hundred metres and the capacity of producing high amounts of power e.g. CO<sub>2</sub> and YAG laser for example.

### 1.3 Young's Slits Experiment

The problem for early physicists investigating interference phenomena was how to make two sources mutually coherent enough so that interference could take place. This was overcome with the work of Thomas Young when he applied Huygen's Principle<sup>2</sup> to the problem. The original experimental set-up is shown figure 1.4.

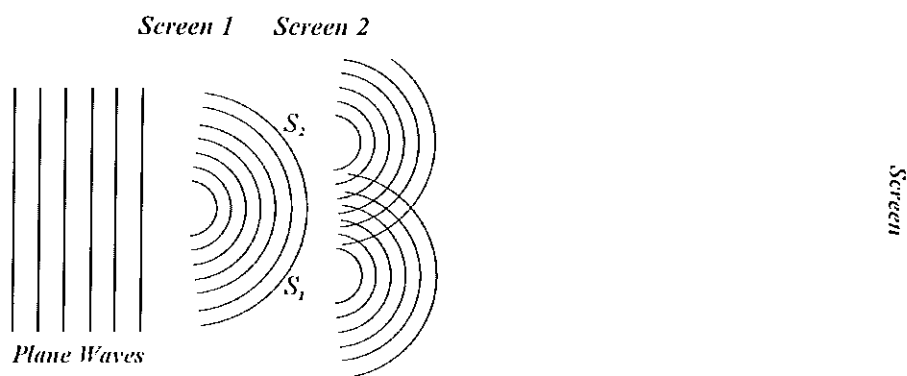
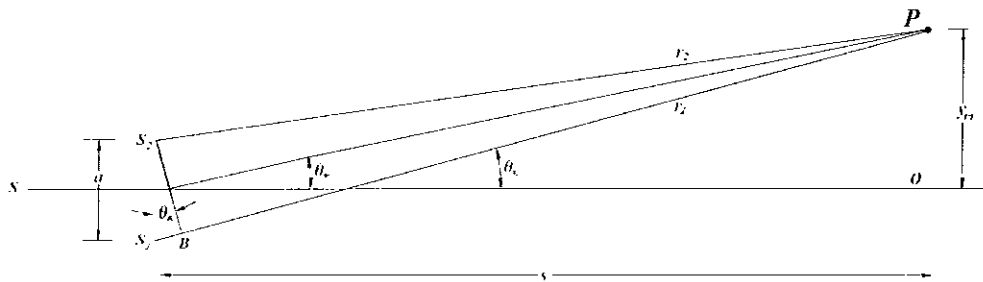


Fig 1.4 Experimental setup Of Young's slits experiment.

Before going through Young's experiment it would be best to look at Huygen's Principle's that first appeared in a written paper in 1690 by the Dutch physicist Christian Huygens. It states that every point on a propagating wavefront serves as a source of secondary waves. This simple statement had far reaching effects on both interference and diffraction theory where it explained why waves after passing through an aperture or obstacle would spread out to some extent into the region that was not in the direct line of the wave.



Using sunlight as a light source Young placed a pinhole in the first screen, to act as an aperture, and thus act as a source of secondary spherical waves. Some distance away a second screen has two pinholes  $S_1$  and  $S_2$  placed side by side, that generate more spherical waves. The waves emerging from the pinholes  $S_1$  and  $S_2$  are of the same phase and frequency figure 1.5.. The emerging waves from the two slits interfere both constructively and destructively to generate an intense pattern on the screen. On closer examination of the intensity pattern it is seen that light and dark bands alternate with a maximum bright band in the centre.



**Fig 1.5 Optical diagram of Young's slits experiment.**

The equation for the position of intensity seen at any point P on the screen will be given below. From the diagram it is seen that the two waves  $S_1P$  and  $S_2P$  transverse different distances before their interaction at point P on the screen, this change in optical path resulting in a varying intensity pattern.

The path difference may be worked out as:

$$S_1B = S_1P - S_2P$$

$$S_1B = r_1 - r_2$$

In terms of the angle  $\theta_m$

$$r_1 - r_2 = a\theta_m$$

Where the assumption that for small angles  $\sin \theta = \theta$

$$\theta = \frac{y}{s}$$

$$r_1 - r_2 = \frac{a}{s} y$$

From what is known, constructive interference  $r_1 - r_2 = m\lambda$

Using the last two relations

$$y_m = \frac{s}{a} m\lambda$$

This equation can now predict where bright fringes should occur on the screen. A follow on from this, in relating the angle  $\theta$  is:

$$m\lambda = a \sin \theta$$

Young's slits experiment demonstrates the wave nature of light due to the diffraction when passing through small apertures and the interference effects observed by the intensity pattern produced on the screen. Interferometric setups may be broken into two main categories, those that are based on division of wavefront and those that are based on division of amplitude. Young's setup would fall into the first category of division of wavefront, other systems include Fresnel's bi-prism<sup>1</sup> and Lloyd's mirror<sup>1</sup>, in that the wavefront is divided laterally into segments by mirrors or apertures. Many examples of division of amplitude interferometers exist and by far the most important example of this category is the Michelson interferometer.

#### 1.4 Michelson Interferometer

It is probably correct to say that no other instrument in history has had such an impact on so many areas of physics as the Michelson Interferometer. It has laid the foundation in many fields such as theory of relativity (Michelson-Morley experiment), establish the existence of the hyper-structure in line spectra, evaluation of the metre in terms of wavelengths, foundation of modern precision metrology and the tidal effect the moon has on the earth<sup>3</sup>. With slight variations in its setup the interferometer has found use in a wide range of applications. It has been turned into an interference microscope for the examination of the topography of microstructures and used widely in the testing of optical components. This versatility in so many areas is due to its simplicity, versatility and stability.

In 1881 Michelson developed his interferometer though over the years there have been some variations on its original construction. It basically consisted of a half silvered mirror,

with a very thin deposit of silver allowing the transmission and reflection of light in equal amounts. In modern setups of the Michelson interferometer the half-silvered mirror is sometimes replaced with a beamsplitter cube.

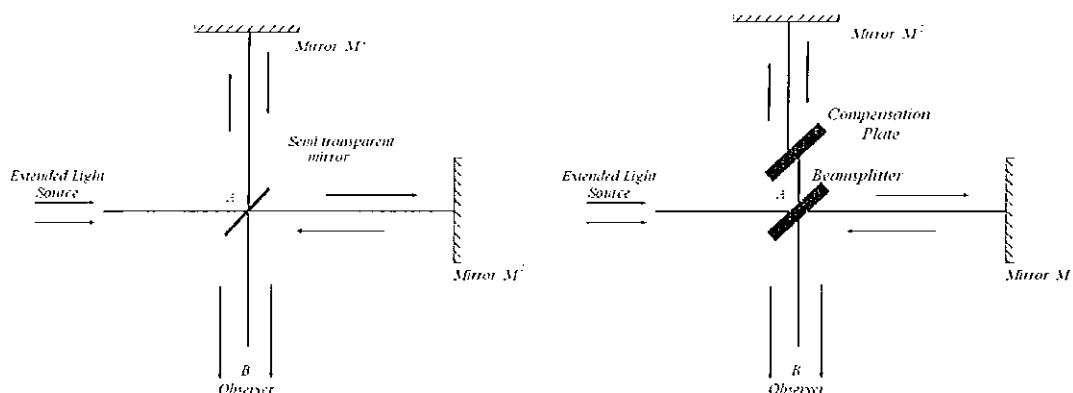


Fig. 1.6 Michelson interferometer optical configuration.

The two beams that are produced by the amplitude division are sent in different directions  $AM_1$  and  $AM_2$ , as seen in figure 1.6. The half silvered mirror serves the purpose of dividing the incoming beam of light into two composite beams that maintain the same frequency and phase as the original wave. Once the two beams transverse the optical path between the mirrors they are recombined to form interference fringes if certain conditions are maintained i.e. the optical path difference transverse by the beam is less than the coherence length of the source.

In some Michelson setups the reflector is replaced with a glass plate that is silvered on the front surface. This has the effect of increasing the optical distance in the  $AM_2$  arm. To compensate for the fact that the two optical paths are not equal a compensation plate, with the same thickness as the glass plate must be placed in one arm of the interferometer. If the glass plate is silvered on the back surface the compensation plate must be placed in the  $AM_1$  beam as illustrated in figure 1.6. The question might be asked why not move one of the mirrors an amount equal to the optical thickness that was introduced by the glass plate. Indeed this can be done, though only for a monochromatic source. When using the instrument with white light moving the mirror is not a solution because of the dispersion effects of the glass<sup>3</sup>. If the mirror was moved to give equal paths for red light, an equal path no longer exists for blue light. Therefore the only way to ensure that there are equal paths for all wavelengths is by the

insertion of a compensation plate in one of the arms that has the same thickness as the glass plate.

Michelson carried out several experiments that yielded many observations. Fizeau had noticed fluctuations in the fringe visibility with sodium light when the components of Newton's rings were progressively separated. This effect may also be observed using the Michelson interferometer as one of the mirrors is slowly moved in relation to the other. Michelson observed this effect on circular fringes, and derived a quantity for the visibility that may be seen from equation 1.14.

$$V = \frac{I_{Max} - I_{Min}}{I_{Max} + I_{Min}} \quad (1.14)$$

Where  $I_{Max}$  and  $I_{Min}$  are the maxima and minima intensity of the fringe pattern and  $V$  the visibility function. The visibility function was defined by comparing the appearance of the rings with patterns of a known visibility. It was found that the visibility varied in relation to the wavelength that was used in obtaining the measurement. Michelson tested line widths from various sources and found that the red line in the spectrum of cadmium gave the best visibility due to its narrow line width. This can be explained by the fact that the more gradual the changes are in the visibility the sharper the line width of the source.

Another important interferometer that has been adapted from the Michelson interferometer is the Twyman-Green interferometer. In 1916 Twyman and Green made a slight modification to the setup that was first used by Michelson. It has now become one of the most valuable interferometers in the testing of optical components. The essential feature that distinguishes it from the Michelson is the introduction of Fizeau-type collimation. The Michelson design normally requires an extended light source but the Twyman-Green uses a collimated beam of light from a point source that is expanded by an achromatic lens. This minor adjustment affects the shape of the fringes produced by the interferometer. Using a Michelson setup the fringes produced by the extended light source are a set of circular fringes. By using the collimated point source as used in the Twyman-Green setup, it leads to a field of uniform tilt. This results in the fringes being of equal thickness. Therefore if the mirrors have

any defects or irregularities, localised contour variations of the interference fringes will be seen and this deviation may be analysed to give surface information such as shape roughness or surface profile.

### 1.5 White Light Fringes

When using white light as a source in an interferometer setup no fringes will be seen unless the path difference between the mirrors is so small that it is not greater than a few wavelengths of the source. A central dark fringe should be seen at the zero order and 5 to 6 coloured fringes may also appear either side of this central location "0" or the optical path difference of zero. It is known that the separation between the fringes is proportional to  $\lambda$ , hence the fringe pattern depends on the wavelength of the source. Note that depending on the optical steep i.e. if a cube beamsplitter is replaced into the setup the central fringe will in fact be bright. If a monochromatic source is used the fringes would appear equidistant for different wavelengths of light, as illustrated in figure 1.7.

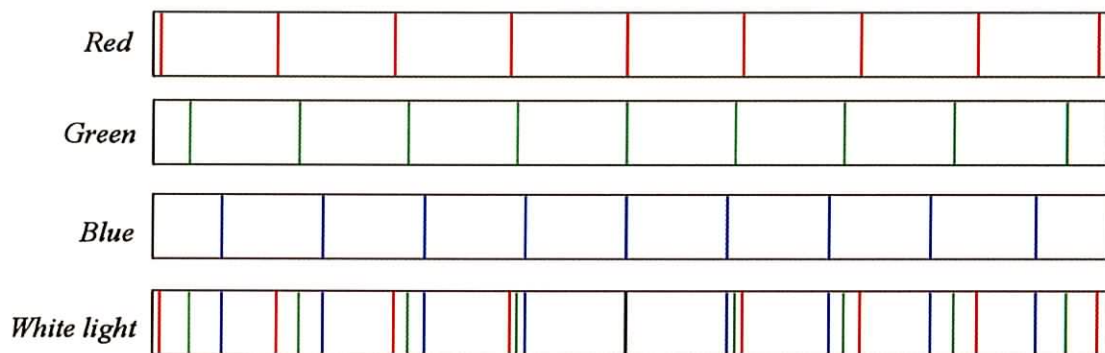


Fig 1.7 Formation of white light fringes.

White light is composed of a number of different wavelengths ranging from 400nm to 700nm. As the wavelength increases the spacing between the fringes becomes more widely spread as in figure 1.7. It is seen that there is one dark central band "0" that is flanked by alternating colour bands. As one moves away from this central region the spacing increases and the fringes merge into one another to form white light. Therefore other than the zero order fringe very few other fringes may be seen, indicating an important property of white light that

allows the identification of the zero order. If using a monochromatic source all fringes appear alike and it would be very difficult to identify the zero order fringe location.

White light on the other hand has an extremely short coherence length, in the range of  $2\mu\text{m}$ . This is due to the large spectral bandwidth of the source. Good contrast fringes will be obtained only when the two paths in the interferometer are closely matched in length. Therefore the optical path difference between two interacting coherence regions must be less than  $2\mu\text{m}$  in order for interference to occur between them.

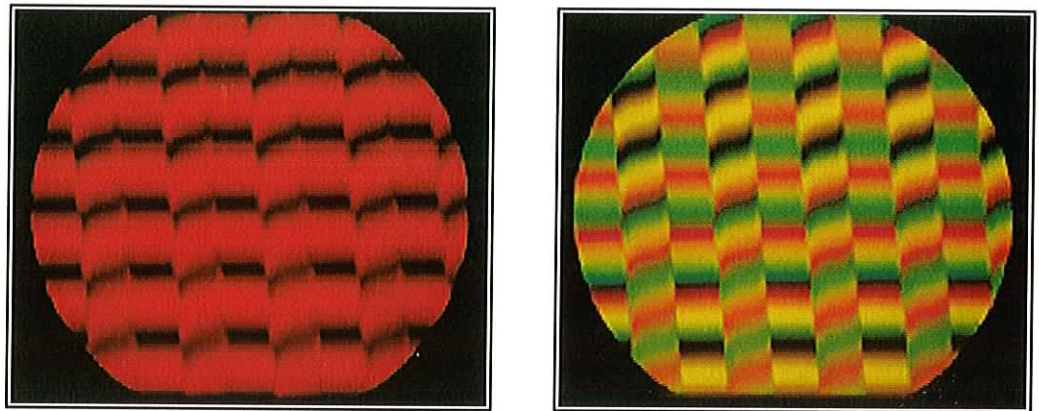


Fig 1.8 Monochromatic fringes v.'s white light fringes.

As white light has such a small coherence region compared to a monochromatic source it is possible to use the property of varying fringe contrast in acquiring the profile of the surface. The same principle may not be used with monochromatic source as it is impossible to differentiate the zero order fringe from the other fringe orders in the viewing plane. From figure 1.8 it can easily be seen the difference of obtaining fringes using a monochromatic source and using white light. The figure consists of a mirror that consists of 2 varying step height steps across the surface. When using monochromatic light it is impossible to differentiate the fringe order from the contrast of the image but if the source is replaced with a white light source it is easier to located the region where the optical path is zero. The principles of using white light for surface profiling shall be discussed in greater detail in the following chapter.

## **CHAPTER 2: METROLOGY METHOD**

### **2.1 Surface Profiling**

In the field of surface profilometry many different types of instruments exist to accurately acquire a three dimensional profile of a surface. The following chapter shall present a detailed study of metrology methods that are used for surface profilometry with an emphasis on optical methods. Different techniques and setups that are used in acquiring and analysing interferograms shall also be outlined. Over the last few decades with the ever-decreasing tolerances in industry it has become more important to be able to define surface characteristics of finished components. Many surface instruments have been developed to help quality control departments in acquiring the characteristics of surfaces in the sub-micrometer range depending on the situation and resolution required. The surface that is to be characterised plays a major role in selecting the instrument that is to be used in obtaining the surface profile, what the range and resolution required must be and whether the surface is opaque to ordinary white light will be important in selecting a profiler.

#### **2.1.1 Contact versus Non-contact methods**

In acquiring the topography of a surface in the range of nanometers to centimetres there are two main methods that one can use, a stylus probe or an optical method. The main difference between the two is that optical methods are non-contact while the stylus probe method involves contact with the surface to be profiled. Both means of attaining a profile have advantages and disadvantages. One contact method of profiling consists of a diamond stylus that measures height variations by moving either the stylus or translating the surface in relation to the stylus<sup>4</sup>. The displacement that the stylus undergoes to maintain contact with the surface is recorded to build up a line profile for the scan. If a surface undergoes several raster scans a 3D profile of the surface can be obtained. The lateral resolution of the diamond probe depends on both the stylus radius and the slope of the surface. A vertical resolution of about 0.2 nm is achievable though if the probe drags along the surface it is possible to damage a delicate material while if the surface is harder than that of the stylus it is possible to damage the probe itself<sup>5</sup>. A major disadvantage of using this technique is that both the vertical and the spatial resolution are limited by the size of the stylus tip. The main advantages of optical

methods are increased spatial resolution, no contact with the test surface, speed of data acquisition and full field of view.

Many different types and varying principles have been applied in the measurement of surface shapes or height profiles using optical methods. These optical contouring techniques include moiré<sup>6</sup>, interferometry<sup>7</sup>, holography<sup>8,9</sup> and speckle<sup>10</sup>.

### **2.1.2 Scanning Tunnelling Microscope and Atomic Force Microscope**

The range and resolution may be important to the type of instrument used in profilometry, should the instrument have the capability to measure in the mm to  $\mu\text{m}$  range or should the instrument concentrate in the sub micrometer range. Such devices that are adept at performing measurements in this sub micrometer region are the scanning tunnelling microscope (STM) and the atomic force microscope (AFM).

In 1981, Gerd Binnig and Heinrich Rohrer of the IBM Zürich Research Laboratory invented the STM<sup>11</sup>. This device used quantum tunnelling to obtain a surface profile with the capacity to image individual atoms, and won Binnig and Rohrer the Nobel Prize in Physics for 1986. If a small bias current is applied between the sample and the tip of the STM (usually it's only one atom in diameter) a small tunnel current will flow when the gap is a few atomic diameters. The STM operates on either constant current or constant height mode. In constant current the tip is scanned across the surface when the tunnelling current is maintained at a constant value.

One of the most recent developments in the profiling of the sub micrometer range is the AFM developed in 1985 by Binnig and Christoph Gerber of IBM Zurich, along with Calvin Quate of Stanford<sup>12</sup>. With the AFM it is possible to profile non-conductive specimens including biological materials by detecting the atomic forces of interaction between its scanning tip and the sample's surface atoms. Since their inception there have been new developments in the field of scanning probe microscopes. It is now possible to image regions on magnetic surfaces, measure temperature at microscopic sites, and monitor the progress of chemical reactions.



## 2.2 Interferometric Method

Optical methods have long been used for the purpose of surface characterisation. One common practice is the inclusion of an interferometric attachment to microscopes to measure the surface roughness of a specimen<sup>13</sup>. Early interference microscope used point measuring heterodyne techniques in order to extract surface roughness from interference fringes. With the advent of computers such techniques have been abandoned in favour of full field phase shifting interferometer (PSI), resulting in systems that give excellent accuracy and measurement speed.

Interference microscopy may be broken into 2 main categories:

Interferometers that measure the surface height variation directly.

Interferometers that measure the differential of the surface height variations<sup>13</sup>.

Both systems have their advantages and disadvantages in the complexity of their setups and the duration of measurement. Differential setups are usually simpler and are less sensitive to vibrations. However, they are also less accurate for measuring surface heights variations than interferometers that measure the height variations directly, and since they measure surface slope errors in only one direction, sample orientation is also very important<sup>14</sup>.

One of the first interferometric setups that used digitised fringe data in the computation of surface profiles was developed by Bruning<sup>15</sup>. This early device comprised of a photodiode array containing 1024 elements, that was used to measure the phase of the interference pattern to  $\lambda/100$ . This system was based around the Twyman-Green interferometer and was used in the profiling of lenses and optical components. Using the data contained by the 32\*32 matrix of values the phase was calculated at each individual point by fast Fourier transform (FFT). Since the early days of surface profilometry substantial technological improvements in both the hardware and software design process have occurred. In the modern era the interferometric intensity values are now recorded using a solid-state detector (CCD cameras, charged coupled device) that have typical array sizes of between 512×512 and 1024×1024. Software has also changed quite dramatically from the early days with the development of many different algorithms and approaches used to acquire relevant

information about surface characteristics. Most software concentrates on taking the human error out of the measurements and giving a system more automation capabilities. In an article in *Laser Focus*<sup>16</sup> (1985) the author predicted that within 10 years a normal interferometric setup would be 10% optical, 10% mechanical, 20% electronics, 60% software; this appears to be the case. The bulk of software developments focus on the reduction of errors, filtering images to reduce signal to noise ratio, image processing, digital processing and the elimination of tilt errors to name just a few.

During the late 70's and early eighties significant research was carried out by Wyant and his colleagues into the development of a non-contact technique for the characterisation of polymeric surfaces, i.e. magnetic tape<sup>17</sup>. One of the main reasons for the development of a non-contact profiler was that the commonly used stylus tool was inadequate for profiling certain types of surfaces and certain ranges. Though the stylus was adequate for smooth hard surfaces offering excellent accuracy and lateral resolution, when used for the purpose of scanning a polymer material to acquire a profile i.e. the stylus "digs" into the surface and therefore the measurement does not represent a true micro topography of the surface.

In modern interference microscope instruments the optical configuration are usually based on one of the three following setups Michelson, Mirau<sup>18</sup>, Linnik<sup>19</sup> if not the incorporation of all three<sup>20</sup>. For such a system the magnification varies from 1.5X (Michelson) to 100X (Linnik) where the Mirau falls somewhere in the midrange of Michelson and Linnik setup (10X-50X). The working range or limit will also vary as the closer the objective lens is to the surface the higher the magnification. The working distance varies between 9.5 mm to 0.3 mm for the Wyko NT2000, with a vertical resolution of 0.1nm to 150  $\mu\text{m}$ . Even though the Linnik has such a high magnification the main drawback of using the setup is that the two objective lenses must be of almost identical quality.

One element that is common to all these profilers is that an interferometric system is used to generate an interferogram of the surface, after which the interferograms are analysed to measure different physical quantities e.g. surface profile. Two main techniques are used in generating this profile, phase shifting and vertical scanning interference. These systems have the capacity to rapidly measure 3D surface height variations with a resolution of 0.1 nm.

### 2.2.1 Phase Shifting Interferometer

Interferometric methods of phase shifting interferometer (PSI) for the analysis of surface profiles were developed in the 1950's. The main developments since the 50's are the means by which the data is collected and analysed. Back then much of the calculations were carried out by hand while now the task is carried out by high speed computers. In the pioneering years prior knowledge of interference patterns was useful as it could save time in highlighting the important points on the interferograms that need to be calculated. With the vast improvements in solid-state detectors and the evolution of high-speed computers, PSI techniques are becoming more popular. Phase shifting interferometry<sup>21,22</sup> can obtain measurements with a precision as high as  $\lambda/100^{43}$  where  $\lambda$  is the wavelength of the light source. PSI may be used with almost any two-beam interferometer and results in a phase map in the range of  $-\pi$  to  $\pi$ . This phase map must be unwrapped to change the range between  $-\pi$  and  $\pi$  to  $0 - 2\pi$  that represents the phase difference across the surface caused by the height variations. From which the height variation across the surface may be extract it the wavelength of the light is known see chapter 3.

Although this technique is easy to implement and very efficient to process it has an unwrapping ambiguity, which is a result of the periodic interference pattern and the discrete sampling. The unwrapping problem or the phase ambiguity is caused when there is a phase difference of greater than  $\pi$  in consecutive or neighbouring pixel caused by the surface height variations or an optical path difference of not greater than  $\lambda/2$ . If such a phase ambiguity is present it is impossible to unwrap the image properly, as the errors would propagate through the remaining phase map. As a result phase shifting is most accurate on optically smooth continuous surfaces that do not have discontinuities greater than  $\lambda/4$ , as the beam has to transverse the optical axis twice i.e. in a Michelson setup. If the step is greater than  $\lambda/4$  between adjacent detector pixels half-wavelength height ambiguities are introduced and the fringe order may not be determined illustrated figure 2.1.

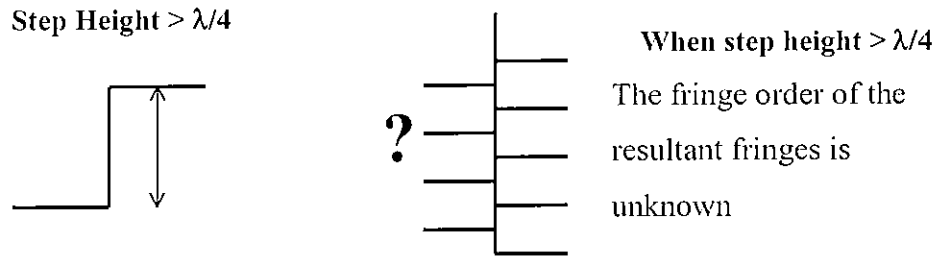


Fig 2.1 Surface height  $> \lambda/4$  results in indistinguishable fringe order

Though PSI suffers from phase ambiguity problems that limits the height difference between two adjacent points to  $\lambda/4$ . Other variations on the phase shifting theme that exist include heterodyne interferometer and multiple wavelength interferometer where the latter may be used to extend the limit of  $\lambda/4$  though there is a loss in resolution<sup>24</sup>. Both methods involve the mixing of two or more wavelengths and using the resultant synthetic frequency for the interferometer measurements<sup>23</sup>. If measurements are performed using two wavelengths  $\lambda_1$  and  $\lambda_2$  it can be shown that the maximum height difference between two consecutive data points is  $\lambda_{eq}/4$  where  $\lambda_{eq}$  is given by:

$$\lambda_{eq} = \frac{\lambda_1 \lambda_2}{|\lambda_1 - \lambda_2|}$$

Multiple wavelength interferometer provides the precision of the wavelengths in use and the dynamic range of the equivalent wavelength. It is then possible to increase the dynamic range to hundreds and even to thousands of micrometers with the selection of two wavelengths. By using multiple wavelengths or the beat wavelength the  $2\pi$  ambiguity may be shifted out thus increasing the size of the step that might be measured, though a reduction in the resolution will occur. While multiple wavelength interferometry works well on step heights it performs poorly on rough surfaces. A much better approach is to use a broad range of wavelengths and the coherence peak detection detailed in the following section.

### 2.2.2 Vertical Scanning or Coherence Peak Detection

One method that is not affected by phase error is vertical scanning<sup>25</sup> or coherence peak<sup>77</sup>. The intention in coherence peak is that as the two beams approach zero optical path difference a maximum and minimum value will appear in the interference envelope as can be seen from figure 2.2.

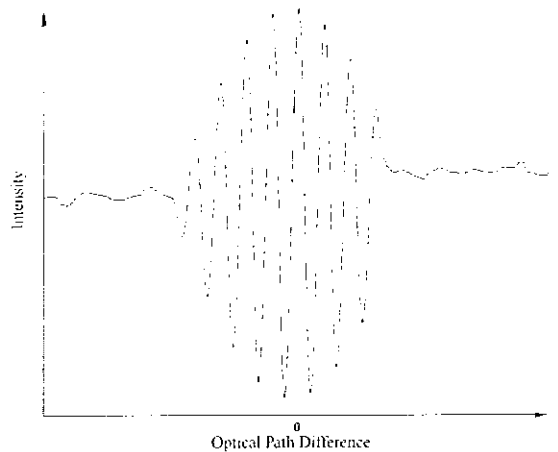


Fig. 2.2. Irradiance at a single point as two beams approach zero optical path difference.

Therefore by writing a program in such a way that it records the frame position that has the highest degree of mutual coherence in a complete scan of the surface it would be possible to work out the profile of the sample. With this method it has been possible to achieve a root mean square height resolution of  $2 \text{ nm}$ <sup>25</sup> comparing this to a value of  $0.5 \text{ nm}$ <sup>26</sup> using phase shifting on highly smooth surfaces. However the algorithm can be used on discontinuous surfaces with a theoretically unlimited range.

There are many algorithms that have been developed for finding the coherence peak which have lead to improved height resolution. As white light has a short coherence length typically of the range of  $1\text{-}2\mu\text{m}$  the resultant interferograms permit the optical path difference between test and reference beams to be measured without the  $2\pi$  ambiguity. One of the first commercial coherence probe microscopes was described in a paper in 1987<sup>19</sup>. This profiler was used mainly in the semiconductor fabrication industry and was based around the Linnik setup.

### 2.2.3 Fourier Analysis

The ideal way to analyse an interferogram is to capture all possible data available though at some point there will be a limit to the amount of data that may be captured and analysed. This is particularly true while using white light interferometer in the profiling of surfaces using coherence scanning methods. Kino<sup>18</sup> and Chim used Fourier analysis to determine where the peak of the coherence function was at its maximum, by isolating the correlation term. Once the coherence function or the visibility envelope function had been extracted in the frequency domain the inverse of the transform is determined. The result is then expressed in the spatial domain hence the position of the coherence peak could be determined. A further development was made to the common path interferometer where the Fourier transform was replaced by a Hilbert transforms. This improvement shortened the duration of the calculation<sup>27</sup>.

Another derivation on Fourier analysis appeared in a paper by Groot and Deck using frequency domain analysis to extract the profile from the interferogram<sup>28</sup>. The traditional method to obtain the surface profile would be to analyse the contrast of the coherence function and correlate the maximum contrast to the surface height for each pixel in the array. Typically 3-5 samples per fringe must be taken to ensure the data will conform to the Nyquist sampling theory (at least 2 samples per fringe). The advantage of using spatial frequency analysis for a broadband source is that sub Nyquist sampling may be performed; one sample point may be taken per fringe without distortion or loss of quality in the final profile. The surface profile by frequency domain analysis may be calculated by determining the rate of change of the interferometric phase with wave number. A broad band source may be looked at as a collection of superimposed single-frequency interference patterns. Each of these may be represented by the following equation.

$$I = 1 + \text{Cos}(\phi)$$

$$\phi = kZ$$

$k$  = angular wave number  $Z$  = phase velocity path difference in the interferometer

Rewriting:

$$Z = \frac{d\phi}{dk}$$

Therefore it is possible to calculate the distance by calculating the rate of phase change with spatial frequency. This rate of change may be provided by the Fourier transform of a white light interferogram. By using such an algorithm in scanning white light interferometers a measurement repeatability of 10 nm has been claimed<sup>28</sup>. As it is possible to define the thickness of a transparent thin film, research has also been carried out into the construction of a 3D volumetric map of the film layer<sup>29</sup>. By using the frequency-domain analysis of white light it is possible to acquire data for the top and bottom surfaces of the thin film in one scan. If the reflection coefficients and the refractive index are precisely known for the material it is possible to calculate the phase difference, as it is a function of the wave number, and thus the wavelength and the film thickness. The system has a vertical resolution in the nanometer range with capacity to measure film thickness that exceeds 0.05 $\mu\text{m}$ . It is hoped that with the help of better linear regression that films less than 0.05 $\mu\text{m}$  may be profiled<sup>29</sup>.

#### 2.2.4 Digital Signal Processing

Another approach to the extraction of the correlation envelope involves the use of communication theory in the form of digital signal processing (DSP) to demodulate the coherence envelope of the signal<sup>30</sup>. The advantage of such a system is that the demodulation of the fringe signal from the interferometric microscope using DSP hardware may be acquired in real time as the measurement is taking place. This technique produces very fast accurate results, for a 256 $\times$ 256 array with a scan height of 10 $\mu\text{m}$  the sample can be scanned in less than 20 seconds. Though the disadvantage is that dedicated DSP hardware is expensive and the working range of the piezo electric transducer limits the scan height to 100  $\mu\text{m}$ . A further development to the Fourier approach was proposed by de Goot and Deck<sup>31</sup> involving the location of the envelope peak in the frequency domain by using phase information.

### 2.2.5 White light Phase Shifting

A natural progression from the well-established phase measuring algorithms of monochromatic interferometry was to apply these techniques to white light interferometry. Larkin<sup>32</sup> proposed an adaptive non-linear algorithm of five-buckets and Sandoz<sup>33</sup> suggested a seven-bucket phase-measuring algorithm. These algorithms allow the measurement of the phase and of the fringe contrast. Though the fringe visibility modulation due to the variations in the coherence function prevents the direct application of classical phase calculation algorithms as the phase is assumed constant over the central fringe. Sandoz<sup>34</sup> also investigated the possibility of adopting wavelet transform as a new alternative method for fringe peak detection.

More modern algorithms have combined PSI with coherence peak and the idea that the advantages of both, high precision and a large dynamic range may be combined in one system<sup>35</sup>. Two profiles are obtained one from the coherence-peak-sensing technique and the other from phase measurement at the maximum modulation contrast. The two profiles are compared and the phase ambiguities removed from the PSI profile by introducing the surface profile obtained from the coherence peak detection method.

## 2.3 Optical Stylus

While contact stylus is available to scan a surface it is also possible to use an optical stylus to achieve similar results. Many different setups<sup>36,37</sup> are available but just two will be discussed below<sup>38,39</sup>. The system developed by Zhang and Cai consists of a commercially available optical head similar to that available in CD-ROM drives. This optical pickup is used in conjunction with a dynamic laser focusing mechanism in the measurement system. Dynamic focusing is carried out through a closed-loop system comprising of the optical head, the tested surface and a PZT that is used to translate the optical pickup. The optical head is therefore only used in the determination of whether the optical beam is in focus and provides the defocusing signal that is used to drive the translation stage. The PZT follows the profile of the tested surface and keeps the objective lens of the optical head at a constant distance from the tested surface. Therefore the movement of the translation stage represents changes in the surface profile.



A similar principle of the optical stylus is discussed by Downs<sup>39</sup>. The system is based around a common path interferometer that utilises a birefringence lens as an interferometer beamsplitter. When the beam of laser light is passed through the birefringent lens the beam is “split” into two states of polarisation, the O and E states. When the surface under test is placed in one of these focus planes of polarisation, light of either the E or O polarisation states is reflected from an area corresponding to the resolution limit of the microscope objective. As a result light for the other polarisation state is out of focus and reflected from a greater area. After reflection from the surface both beams recombine and the resultant beam therefore consists of two orthogonally-polarized components. The phase of one component is determined by the surface level at the focused spot of light, whilst the phase of the other is a reference level integrated over the larger area of the defocused beam. As the surface is scanned this phase difference between the two components varies according to the surface profile hence a 3D view of the test object is constructed from these phase values.

## 2.4 Moiré Fringes

Moiré topography methods are becoming more and more popular. These techniques are based on the superposition of grating lines either directly or by projection. Due to the mathematical similarities with interference fringes similar processes may be used in the extraction of the relevant data from moiré fringes. A well-known technique entitled shadow moiré is used in the profiling of 3D objects. Shadow moiré involves the evaluation of moiré fringes formed by the grating and its own shadow. This method offers a wide working range of height measurements and resolutions of 1µm are achievable. This technique uses a grating that is placed above the sample and light illuminated onto the surface. Height information between moiré fringes may be calculated from the equation below.

$$\Delta z = \frac{d}{(\tan \alpha_s + \tan \alpha_o)}$$

Where d is the period of the grating,  $\alpha_s$  angle of illumination,  $\alpha_o$  angle of observation direction.

To achieve a resolution of  $1\ \mu\text{m}$  a short grating spacing is required, though diffraction effects become dominant and spoil classical shadow moiré analysis for 3D objects other than quasi-flat surfaces. Shadow moiré is mainly used in surface characterisation such as thermal surface deformation analysis, checking flatness or structural deformation analysis. In recent development phase shifting interferometer has been applied to shadow moiré<sup>40</sup>. By acquiring four moiré fringes with different phases it is possible to process the image and acquire a height map of the surface.

## 2.5 Other Surface Profiling Methods

Another non-contact means of measuring the surface profile is measuring the light that is scattered off the surface. This represents a simple and straightforward approach yet it does not measure surface structure directly<sup>41</sup>. The simplest instrument of this type is the glossometer and measures the spectral reflectance of the surface at a fixed angle. The refractive index and smoothness of the test surface has an impact on the final readings for such an instrument. Therefore the resultant data from a glossometer do not give a true representation of the surface topography; at best it gives an average surface topography

Another area in which profilers have been used extensively over the past decade is in the conservation and preservation of many art works<sup>42</sup>. What Spannolo proposed was a novel diffractive optical element (DOE) system. The advantages are clear over current systems available as the system is small, compact, light weight and easy to assemble and disassemble. Fringes generated by the DOE interferometer are projected onto the surface under test and are then analysed by a fast Fourier transform (FFT), and a phase unwrapping algorithm based on least squares formulation is used to unwrap the images to produce the 3 D profile of the surface.

## 2.6 Optical Configuration for Interferometric Microscopes

The coherence scanning microscope is based on a white light interferometer where the object or the reference mirror is scanned in the longitudinal direction as in figure 2.3. All scanning white light microscopes are based on the three main setups that have been mentioned before, Michelson, Mirau and Linnik. Monitoring one point in the image during a scan results in white light fringes and the coherence function is given by the envelope of these fringes. By determining the peak amplitude of the envelope the location of the surface of the object can be found with a high accuracy resulting in the acquisition of a 3-D profile of the surface.

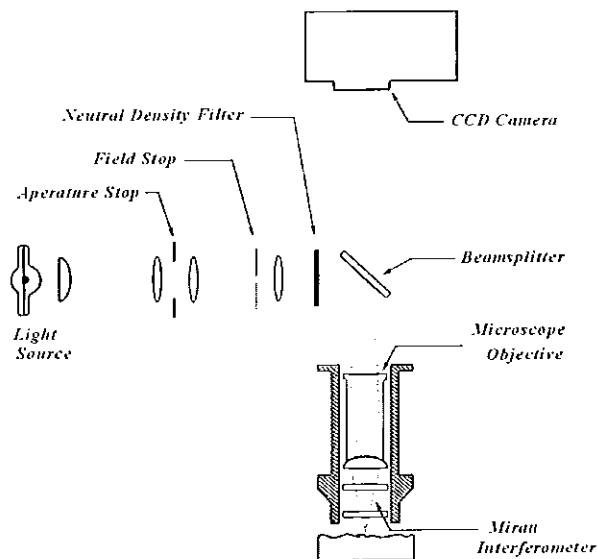


**Fig 2.3** Optical configuration of coherence scanning microscope.

The type of setup used in a scanning coherence microscope will depend on the resolution and the field of view required as the magnification may vary from 1.5X to 100X.

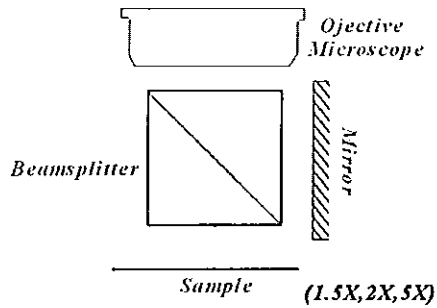


Fig. 2.4. Optical Configuration for Michelson Interferometer.

The simplest of all optical configurations is that of the Michelson interferometer figure 2.4. The disadvantage though of the Michelson is the poor magnification and spatial resolution that is achievable with the configuration and the beamsplitter limits the working range of the device. Though the configuration does allow a large field of view, magnification of 1.5X, 2.5X and 5X are the most commonly used for the Michelson. The most versatile design for a profiler of all interferometric setups is that of the Mirau configuration shown in figure 2.5. The advantage of using the Mirau interferometer over any other profiling system is that interference fringes are only formed when the reference and measurement path are almost equal, this reduces the ambiguity in the object position though the setup suffers due to a limited numerical aperture.

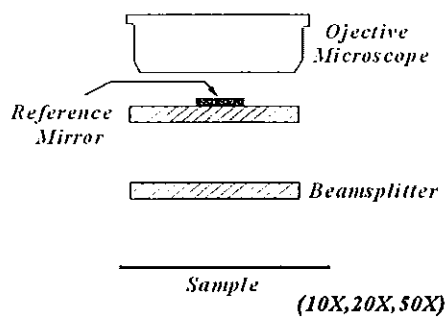
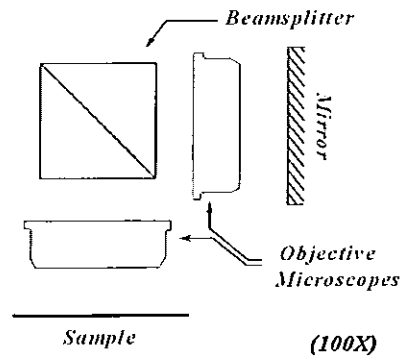


Fig 2.5 Optical configuration for the Mirau interferometer.

Due to its common path configuration vibration and environmental effects are reduced in comparison to other interferometric setups and the measurement is not polarisation dependent. Usually the planar beam splitter is constructed by the deposition of a thin film that allows the partial transmission and reflection of the interacting beams.



**Fig 2.6 Optical Configuration for Linnik Interferometer.**

Looking at the optical setup of the Linnik, figure 2.6. Similarities may be drawn with the optical construction of the Michelson interferometer. The main addition to the configuration is the addition of two objective lenses in both the object and reference arms of the interferometer. These objective lenses give the setup high magnification with a large numerical aperture, but due to the high magnification the configuration has a reduced field of view in comparison to the Michelson and Mirau setups. As mentioned earlier both the objectives must be matched to reduce error in the measurement and this tends to make the setup expensive.

## CHAPTER 3: PHASE-MEASUREMENT INTERFEROMETRY

### 3.1 Introduction

Most optical techniques applied to profilometry and metrology rely on the analysis of a fringe pattern distribution. Within this intensity distribution lies the phase information of the interfering beams and the relative differences in the optical paths are encoded in the phase of the fringe pattern. By unlocking these phase values and by reconstruction it is possible to find the missing parameter i.e. surface height<sup>43</sup>. Phase-measurement interferometer (PMI) is used to measure wavefront phase in an interferometric configuration. Usually the phase is determined by arctangent tan function. Once the phase is calculated it is in the region of  $-\pi$  to  $\pi$ , the range of the arctangent function and for this information to be of any practical use it must be unwrapped to a continuous phase distribution i.e. 0 to  $2\pi$ . Once the phase has been calculated across the entire field of view it is possible to calculate the height variation across the surface. This calculation will be outlined in greater detail later in the chapter. Not all PMI techniques need to be unwrapped, techniques that do not include unwrapping include phase-locked loop<sup>44</sup> and the complex phase tracing method<sup>45</sup>. PMI is a powerful tool for rapidly acquiring accurate and highly repeatable measurements provided that the instrument is properly adjusted and is operating in a quiet environment. The principles of this technique have been around since the late 1960's and early 70's. With the advances in technology, increase in CPU speed and developments of high quality CCD detectors, PMI has become an important tool for metrologist's worldwide. Many different types of algorithms have been developed, including Carrie<sup>46</sup>, Bruning<sup>47</sup> and Wyant<sup>48</sup> who all have made major contributions in the area over the years. These algorithms shall be discussed later as there are advantages and disadvantages associated with each depending on speed of data analysis and immunity to errors.

PMI techniques can be divided into two categories, temporal PMI (TPMI) and spatial PMI (SPMI). The main differences between the two techniques are the methods used in obtaining the data. For TPMI the data is taken sequentially while SPMI measurements are taken simultaneously. There are many variations on the TPMI idea but there is a common thread with all in that a phase shift is introduced in relation to the object and reference beams. Then by acquiring a number of frames from the detector it is possible to calculate the phase of

the wavefront. In spatial methods the phase is separated out in the image plane and is recorded in one frame time. Both methods have advantages in different applications.

Most of the wavefront measurements are now performed by analytical means and high speed computers. A detector or CCD camera is placed in the plane of the interference signal and the interferogram is grabbed and converted to an array of integers and then processed to find the wavefront phase. This type of measurement can have repeatability of one hundredth of a fringe<sup>43</sup>. In the early days most of these calculations were carried out by electronic means and hardware included zero-crossing detectors<sup>48</sup>, phase-lock loops and up-down counters. Most setups utilised a single detector therefore the phase measurement is performed at a single point and in order to measure an area the surface must either be scanned or there must be a set of multiple detectors to perform the task. As this technique essentially involves the counting of fringes as they pass the detector point loss of the signal for any reason caused the whole measurement to be repeated. Nowadays these techniques are used extensively in distance measurements where a calculation at a point is required in real time e.g. stepper motor used in lithography.

### **3.2 Means of Phase Shifting**

Phase measuring techniques can be implemented into virtually any type of interferometer as long as there is some means of modulating the phase between the reference and test wavefronts though this phase modulation is usually accomplished in the reference beams. The nature of the phase shift may be continuous or as a discrete phase shift between the object and reference beams, depending on whether phase shifting or phase stepping is to be used which will be discussed later. In practice accurate application of predetermined phase steps are difficult as steps of  $\lambda/8$  or less are required. There are many methods of introducing a phase modulation into the reference beam, as illustrated figure 3.1 including a moving mirror, translating or rotating grating, rotating wave plate, electro-optical modulators, multiple gratings, laser frequency modulation or rotating glass plate

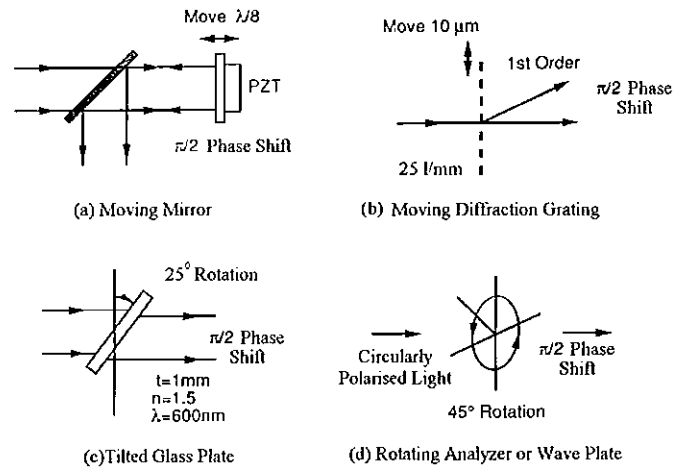


**Fig 3.1 Means of achieving a phase shift of  $90^\circ$ .**

The simplest and most common approach of all phase inducing setups is that of moving a mirror. A piezoelectric transducer using a ferroelectric ceramic, such as lead zirconate is attached to the reference mirror which can be translated along the optical axis, and in the process introduce a uniform phase change across the entire reference wavefront. The PZT is connected to a high voltage amplifier that linearly ramps the voltage from 0 to several hundred voltage to drive the PZT. PZT transducers however, are difficult to calibrate on such a small scale and the PZT materials tend to behave nonlinearly.

A glass plate may also be used, this is done by placing a piece of glass in either the object or the reference arm of the interferometer. As the glass plate is rotated through different angles phase shifts are induced into the interferometer by changes in the optical thickness of the glass. One disadvantage of using such a system is that the plate must be of a high optical quality and care must be taken so that the optical path is the same across the entire beam diameter<sup>49</sup>.

Another phase modulation technique involves continuously moving a diffraction grating in one arm of the interferometer. When a diffraction grating with a spatial frequency  $f$  is moved with a velocity  $v$  a frequency shift is produced in the  $n^{\text{th}}$  diffracted order of  $nvf$ <sup>[49]</sup>. One final technique comprises of rotating a half-wave plate. The output of the interferometer will produce a frequency shift of twice its rotation frequency, i.e. a rotation of  $45^\circ$  will yield a  $\pi/2$  phase shift<sup>49</sup>.



### 3.3 Four Bucket Algorithm Derivation

Over the years many different algorithms for calculating the wavefront phase have been developed<sup>46,47,50</sup>, and these algorithms may be broken into two groups; the first of these programs step the phase a discrete amount between intensity measurements and thus is known as phase stepping while others linearly ramp the phase while integrating the intensity measurements, these are known as phase shifting techniques.

An electromagnetic wave may be mathematically modelled as:

$$U(z,t) = a(z) \exp[-i(kz - \omega t + \phi)]$$

Therefore if two beams arrive at in the same point in space they superimpose.

$$U_R = U_1 + U_2$$

The resultant irradiance pattern is given by:

$$\begin{aligned} E(z) &= \langle |U_R|^2 \rangle = \langle (U_1 + U_2)(U_1 + U_2) \rangle \\ &= E_0(z) \left[ 1 + V \cos\left(\frac{2\pi\Delta z}{\lambda} + \Delta\omega t + \phi\right) \right] \end{aligned} \quad (3.1)$$

Where:

$E_0$  = Irradiance amplitude

$V$  = Visibility

$\Delta z$  = Optical path difference between the two waves

$\Delta\omega$  = Optical frequency difference between the two waves

$\phi$  = Phase difference between the two waves

If  $z = 0$ , and  $\phi = 0$ ,  $\Delta\omega = 0$ , and  $V=1$  the measured irradiance will be  $2E_0$

$$E = E_0 \left[ 1 + \text{Cos} \left( \frac{2\pi}{\lambda} \Delta z \right) \right] \quad (3.2)$$

Giving bright fringes when:  $\Delta z = n\lambda$  (3.3)  
and dark fringes when:  $\Delta z = \left( n + \frac{1}{2} \right) \lambda \quad n = 0, 1, 2, \dots$

If one of the above parameters, either the optical path, optical frequency or the phase difference changes, then the E field varies between  $2E_0$  (constructive interference) and 0 (destructive interference). By controlling one of  $\Delta z$ ,  $\Delta\omega$  or  $\Delta\phi$  it is possible to find the other values by making at least three irradiance measurements. For example by controlling  $\Delta z$  the following four equations result.

Rewriting equation 3.1  $= E_0(z) [1 + \text{Cos}(k\Delta z + \phi)]$

$$E_1 (\Delta z = 0) = E_0 (1 + \text{Cos} \phi)$$

$$E_2 (\Delta z = \lambda/4) = E_0 (1 - \text{Sin} \phi)$$

$$E_3 (\Delta z = \lambda/2) = E_0 (1 - \text{Cos} \phi)$$

$$E_4 (\Delta z = 3\lambda/4) = E_0 (1 + \text{Sin} \phi)$$

These four equations may be rearranged to the more recognisable standard 4-bucket technique to solve for the phase  $\phi$  equation 3.4.

$$\phi = \text{Tan}^{-1} \left[ \frac{E_4 - E_2}{E_1 - E_3} \right] \quad (3.4)$$

As mentioned the phase shift or modulation of phase in an interferometer may be induced by moving a mirror, tilting a glass plate, moving a grating or rotating a half-wave plate or analyser. These phase shifts may be continuous as well as discrete shifts between the object and reference beams. Though all methods have the same result in that by changing the optical path or by shifting the optical frequency difference between the beams an intensity variation may be seen as the result<sup>51</sup>.

### 3.4 Optical Path Difference Techniques

When the two interfering beams have the same frequency  $\Delta\omega = 0$  but have transversed different optical paths  $\Delta z$  the resultant intensity value is written as:

$$E = E_0[1 + V\cos(k\Delta z)]$$

The magnitude of the intensity is therefore dependent on the optical path difference between the beams.

Unlike the phase stepping procedure where the phase changes by discrete amounts phase shifting relies on the phase being linearly increased. For simplicity in phase shifting the intensity at a pixel for each data frame may be written as:

$$E = E_0[1 + V\cos(\phi + \alpha)]$$

For  $I_0$  intensity,  $V$  fringe visibility,  $\phi$  wavefront phase,  $\alpha$  difference in relative phase between the test and the reference beams. With three unknowns it is possible by taking a minimum of 3 measurements to calculate the unknown phase value. The phase shift between any consecutive measurements may be any value from 0 to  $\pi$ . But in phase shifting interferometer the output signal at the detector is solely analysed. This phase shift is assumed to change during the integration time and also this shift is assumed to be the same during each frame acquisition. Detectors do not measure an instantaneous irradiance but a time average value.

### 3.4 Optical Path Difference Techniques

When the two interfering beams have the same frequency  $\Delta\omega = 0$  but have transversed different optical paths  $\Delta z$  the resultant intensity value is written as:

$$E = E_0 [1 + V \cos(k\Delta z)]$$

The magnitude of the intensity is therefore dependent on the optical path difference between the beams.

Unlike the phase stepping procedure where the phase changes by discrete amounts phase shifting relies on the phase being linearly increased. For simplicity in phase shifting the intensity at a pixel for each data frame may be written as:

$$E = E_0 [1 + V \cos(\phi + \alpha)]$$

For  $I_0$  intensity,  $V$  fringe visibility,  $\phi$  wavefront phase,  $\alpha$  difference in relative phase between the test and the reference beams. With three unknowns it is possible by taking a minimum of 3 measurements to calculate the unknown phase value. The phase shift between any consecutive measurements may be any value from 0 to  $\pi$ . But in phase shifting interferometer the output signal at the detector is solely analysed. This phase shift is assumed to change during the integration time and also this shift is assumed to be the same during each frame acquisition. Detectors do not measure an instantaneous irradiance but a time average value.

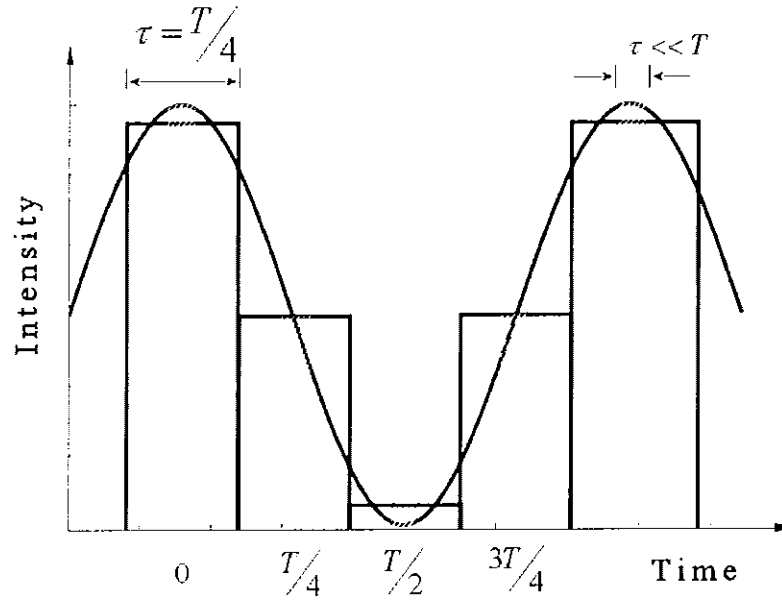


Fig. 3.2 Integration of irradiance for phase shifting interferometer.

Assuming that the phase shift is known, the initial phase difference may be determined by observing the irradiance signal at four specifically known times of the beat period  $T$  ( $0$ ,  $T/4$ ,  $T/2$ ,  $3T/4$ ) for a  $90^\circ$  shift, as illustrated in figure 3.2. The phase value is continually changing during the measurement therefore the result is that the signal suffers a contrast reduction.

$$E = E_0 [1 + V \text{Sinc}(\Delta \nu \tau) \text{Cos} \phi]$$

where:

$$\text{Sinc}(\Delta \nu \tau) = \frac{\text{Sin}\left(\frac{2\pi\Delta \nu \tau}{2}\right)}{\frac{2\pi\Delta \nu \tau}{2}} = \text{Sinc}\left(\frac{\tau}{T}\right)$$

and

$$\tau = \text{Integration time, } T = \text{Modulation Period}$$

This technique is called a bucket or integrating bucket because of the time averaging at the detector. It is important to note that the only difference between integrating the phase and stepping the phase is a reduction in the fringe visibility after detection by  $\text{Sinc}(\tau/T)$ . For example when the integration time is one quarter of the modulation period then the reduction factor is 0.83. If the integration time is made infinitely short or the modulation period

infinitely long then irradiance measurements would be equivalent to phase stepping measurements as the sinc function would have a value of one. At this stage it is important to point out that the irradiance amplitude, the fringe visibility and sinc() terms all cancel out of the phase calculation. This results in the sinc() term reducing the signal to noise ratio, hence increasing measurement repeatability.

$$E(t) = E_0[1 + V\cos(\phi + \omega t)]$$

$$I = \int_{t-\tau/2}^{t+\tau/2} E(t) dt$$

$$= I_0[1 + V \operatorname{sinc}(v\tau)\cos(\phi + \omega t)]$$

note sinc() = visibility reduction due to phase-shift during integration time

### 3.5 Algorithm Performance and Selection

It has been known for some time that the selection of a phase algorithm can greatly affect the performance of a system<sup>52</sup>. For many years due to the low processing power in comparison to modern computers many three and four step algorithms were used as they required minimum storage capacity. The best algorithms were those considered for their speed and not their accuracy. Unfortunately the faster algorithms were more prone to phase errors. When selecting an algorithm for a phase measuring application it is also important to take into account the error inherent in the algorithm<sup>53,54</sup>. The error in the phase measurement is introduced if the desired phase steps are not achieved. Since phase shifting devices are subject to inherent errors of reproducibility, hysteresis, nonlinearity or temperature and age dependence a number of calibrating techniques have been designed<sup>55,56,57,58</sup>. In the modern era with increased computational power, algorithms are being designed that use more data points but at the same time are more resilient to environmental errors<sup>59</sup>.

Thus far only one algorithm has been discussed in any great detail i.e. equation 3.4. To implement it correctly a phase shift of  $90^\circ$  must be induced in one arm of the interferometer,

although this algorithm is not the only phase shifting algorithm as will be shown in the following section. Two important parameters must be considered in defining a phase algorithm, though both stem from one another. Firstly the phase increment between intensity readings must be chosen, increments include  $90^0$ ,  $120^0$  and  $45^0$  and secondly the number of intensity frame readings that are to be taken to calculate the wavefront phase must be decided<sup>60</sup>. As stated earlier the lower limit on the number of readings to be used for computation is three while there is no limit on the number of readings taken for the upper limit but for the processing power of the computer used.

A  $90^0$  phase shift is probably one of the most used. Below are some of the algorithms that use such a phase increment.

$$\phi = \text{Tan}^{-1} \left[ \frac{(I_1 + I_3) - 2I_2}{I_1 - I_3} \right] = \text{Tan}^{-1} \left[ \frac{I_3 - I_2}{I_1 - I_2} \right] \text{ (Three Bucket)} \quad (3.5)$$

As the three-bucket algorithm in equation 3.5 uses the fewest number of intensity measurements, it is mainly used in applications that are time dependent. Systems using the three-bucket algorithm are usually prone to vibrations and temperature variations. Though with one common variable in the numerator and the denominator the algorithm suffers from a noise correlation problem.

$$\phi = \frac{1}{2} \left\{ \text{Tan}^{-1} \left[ \frac{I_3 - I_2}{I_1 - I_2} \right] + \text{Tan}^{-1} \left[ \frac{I_4 - I_3}{I_2 - I_3} \right] \right\} \text{ (3+3 Bucket)} \quad (3.6)$$

An evolution of the 3-bucket algorithm is the 3+3 bucket algorithm in equation 3.6. By averaging two phase estimates it is possible to reduce the effect of phase shift and ghost errors<sup>51</sup>.

$$\phi = \text{Tan}^{-1} \left[ \frac{[3(I_2 - I_3) - (I_1 - I_4)][(I_2 - I_3) + (I_1 - I_4)]^{1/2}}{[(I_2 + I_3) - (I_1 + I_4)]} \right] \text{ (Carré)} \quad (3.7)$$

One advantage of using the popular Carré algorithm in equation 3.7 over many of the others is that unlike the other algorithms where the phase shifter must be calibrated to

increment a set amount each time the Carré algorithm just requires the phase modulation to be linear. It does not matter if the phase increment is  $90^0$  or  $95^0$  as long as the phase increment remains constant. The disadvantage of using the Carré algorithm is that it is sensitive to quadratic phase shift errors and is complicated to implement. Detailed error analysis has been carried out to investigate the relationship between the actual step used by the Carré method and the phase error associated with the step. The accuracy of the Carré algorithm has been investigated using computer<sup>61</sup> simulations and theoretical analysis<sup>62</sup> with a phase step of  $\pi/2$ . By using a linear approximation of the Taylor expansion on the phase function it has been shown that the most appropriate step to use is  $110^0$  in the minimisation of phase errors<sup>63</sup>.

$$\phi = \text{Tan}^{-1} \left[ \frac{I_2 + I_4}{I_3 - \frac{(I_5 - I_1)}{2}} \right] \quad (3.8)$$

or

$$\phi = \text{Tan}^{-1} \left[ \frac{2(I_2 + I_4)}{2I_3 - (I_5 - I_1)} \right] \quad (3.9)$$

The most widely used algorithm in surface metrology is the five-frame algorithm Schwider<sup>65</sup> shown in equation 3.8 or Hariharan<sup>64</sup> in equation 3.9. These algorithms are essentially the same but for some minor alterations in the calculation of the phase value. Unlike the Carré technique the five-bucket algorithm is insensitive to quadratic and linear errors. It does require the phase shifter to be calibrated in that it demands a phase shift as close to  $90^0$  as possible. This algorithm is designed to reduce the possibility of having the numerator and the denominator tend to zero. Note also that the algorithm takes a fifth frame. This extra frame is used in comparison to the first frame so as to reduce phase modulation errors.

Other algorithms using phase increments other than  $90^0$  include the eight bucket  $45^0$  algorithm, the sixteen-bucket algorithm and the three bucket  $120$  algorithm. One final algorithm of note developed by Vikhagen<sup>66</sup> was originally used for TV-holography and requires the collection of many frames of interferograms with random phase shifts. With each new frame the maximum and minimum intensity value at each pixel point is determined. As the number of frames increases these values will approach the maximum and minimum



intensities  $I_{\max}$  and  $I_{\min}$ . Once these values are established the phase and the fringe visibility may be found using:

$$\phi = \text{Cos}^{-1}\left(\frac{I_i - I_0}{\gamma I_0}\right) \text{ where}$$

$$I_0 = \frac{I_{\max} - I_{\min}}{2} \text{ and } \gamma = \frac{I_{\max} - I_{\min}}{I_{\max} + I_{\min}} = \frac{I_{\max} - I_{\min}}{2I_0}$$

Once a large number of frames have been recorded the phase may be calculated as each new intensity frame is acquired.

### 3.6 Removal of phase ambiguities

In the application of any of the algorithms that have been discussed it is important to note that some minor alterations need to be made to the phase in order to use the data to obtain a 3D profile of a surface. Theory indicates that the wavefront phase is calculated modulo  $2\pi$ , though the calculation of  $\Delta\phi$  from the algorithms does not comply. The reason for this is that the inverse tan function has two discontinuities caused when the cosine goes through zero, see the phasor diagrams in table 3.1.

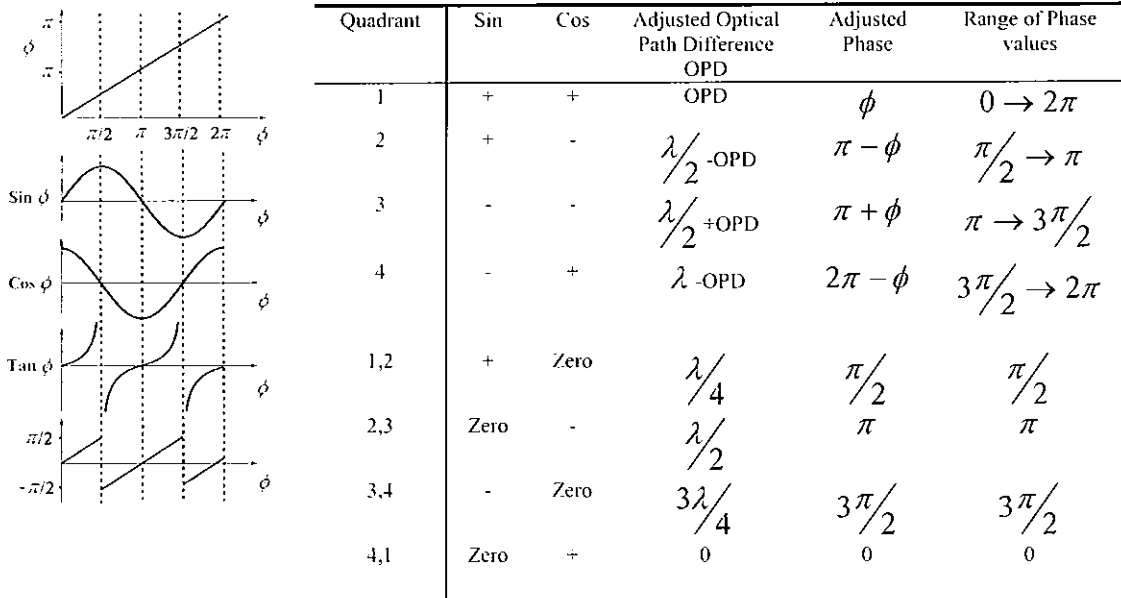


Table 3.1. Correction to the phase values.

As a result the equations presented for phase determination only calculate the phase for modulo  $\pi$ . To extend this range to  $2\pi$  the signs of the numerator ( $\sin \phi$ ) and denominator ( $\cos \phi$ ) must be examined and the appropriate value added or subtracted to bring the value into the  $2\pi$  range as in table 3.1.

This approach works for all techniques but for Carré's. For Carré algorithm simply looking at the numerator and the denominator is not sufficient to determine phase modulo  $2\pi$ <sup>67</sup>. Here the signs of the quantity proportional to  $\sin \phi$  and  $\cos \phi$  must be examined.

### 3.6.1 Phase unwrapping

Interferometric techniques such as phase stepping and Fourier analysis of carrier fringes result in the phase values being calculated. The phase maps must be unwrapped to extract the height information for the image. Given a noise free map it is enough to search the column by column and row by row looking for phase variations of greater than  $\pi$  between neighbouring pixels<sup>68</sup>. If such a difference of  $\pi$  is found between neighbouring pixels a value of  $2\pi$  is added or subtracted until collateral pixels have a difference of less than  $\pi$ . When the phase at each point in the waveform has been found it is possible then to calculate the surface height  $H$  at each location  $(x,y)$  where  $\theta$  and  $\theta'$  the angles of illumination with respect to the viewing surface as illustrated in figure 3.4.

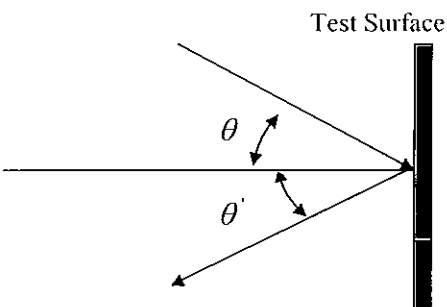
$$H(x, y) = \frac{\phi(x, y)\lambda}{2\pi(\cos \theta + \cos \theta')}$$


Fig 3.4 Calculation of the surface using extracted phase values.

The relationship between the phase and the height obtained will depend on the specific setup of the interferometer for example using a Fizeau interferometer or Twyman-Green interferometer the above equation relating the phase to the surface height may be rewritten as:

$$H(x, y) = \frac{\lambda}{4\pi} \phi(x, y)$$

The above example demonstrates the ideal case in that the set of fringes used in the calculation of the phase map suffers from no noise and the phase map itself has no discontinuities. The main problem with the row by row and column by column unwrapping is that when unwrapping phase maps that have large amounts of noise, unwrapping propagates errors to regions that are far removed from the original localised noise source. Depending on the given phase map there are many algorithms to choose from. Most algorithms are based on the local gradient of an individual pixel, by comparing the local gradient of neighbouring pixels it is possible to determine the search path along which the image may be unwrapped. There are many unwrapping programs to choose from tile methods<sup>69</sup>, cellular methods<sup>70</sup>, graph theory approaches<sup>71</sup> and fringe pattern bandwidth techniques<sup>72</sup>. All unwrapping routines are sensitive to noise while some have the capacity to handle certain errors on certain types of phase map, though no single algorithm can do everything. The above algorithms do breakdown when discontinuities caused by shadows or holes occur and when fringes do not cover regions of the object. Evaluations of many unwrapping techniques have appeared in many papers<sup>73,74</sup> which outline the advantages and disadvantage of several methods.

### 3.7 Phase-Shifter Calibration

The value of the phase shift may be determined in a number of different ways but the simplest of all is by simply looking at the frames.

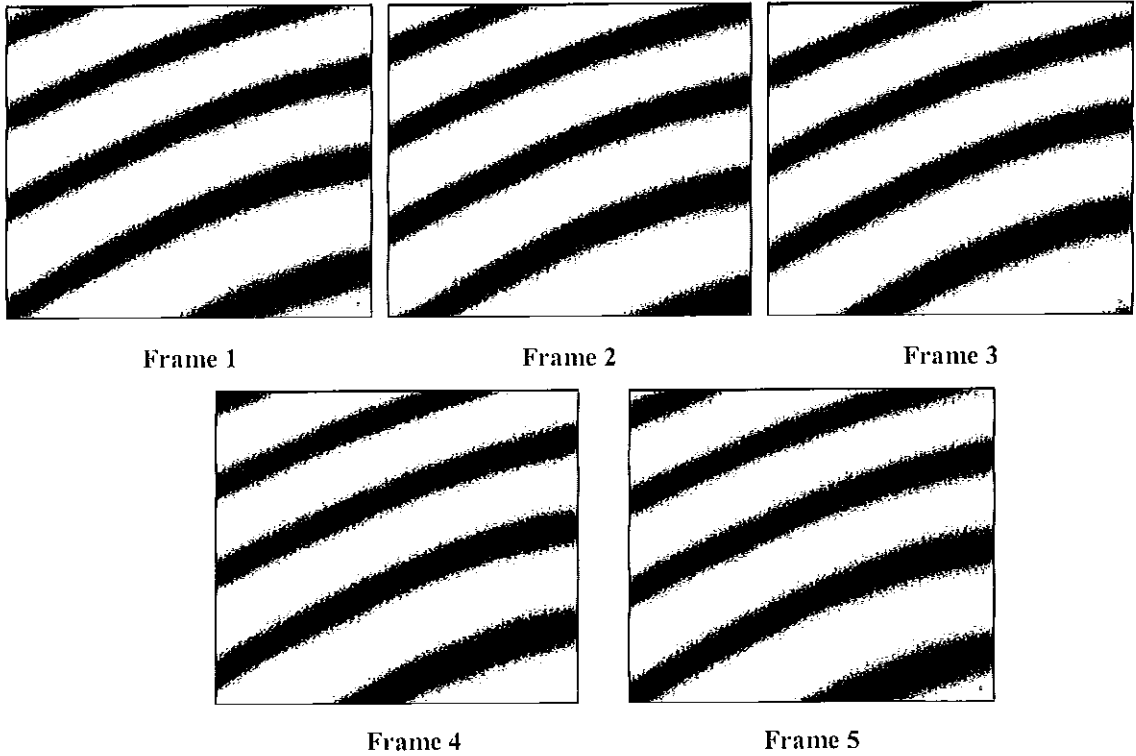


Fig 3.5 Five intensity maps with a phase shift of  $90^{\circ}$  between each frame.

Figure 3.5 contains five frames with different fringe modulations depending on the amount the shifter has been displaced from the starting point in frame one. Each frame has been shifted  $90^{\circ}$  in relation to the previous frame. i.e. frame 1 and frame 5 should look the same as a  $360^{\circ}$  phase shift has been induced in one arm of the interferometer. Frame 1 and frame 3 should have a complimentary intensity pattern to one another because they are shifted by  $180^{\circ}$  as should frames 4 and frame 2.

The above method is just an estimation; a more accurate approach is to calculate the phase directly for each pixel. A simple equation using 5 intensity values is used in the calculation of the phase and is shown below equation 3.10.

$$\alpha = \text{Cos}^{-1} \left[ \frac{1}{2} \left( \frac{I_5 - I_1}{I_4 - I_2} \right) \right] \quad (3.10)$$

From the calculated phase shift  $\alpha$  a histogram may be plotted of all the phase values in the interferogram. If the phase modulating device is properly calibrated to perform phase shifts of 90 degrees the histogram should look similar to that of figure 3.6

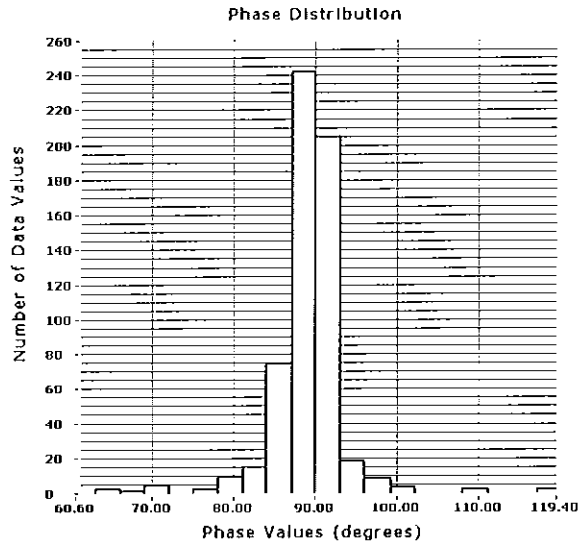


Fig 3.6 Histogram of phase value from one interferogram.

The phase shifter should be adjusted so that the centroid of the histogram appears at the desired value of  $90^0$ . Skewness or spread of the histogram indicates a tilt of the phase shift or poorly collimated beams of light.

### 3.8 Phase Shifting using White Light

The output intensity from a polychromatic light source may be written as equation 3.11:

$$I(z) = I_0(1 + v g(z) \text{Cos } \phi) \quad (3.11)$$

$I_0 = I_1 + I_2$ , background intensity.

$v$  = fringe visibility.

$\phi(z) = 4\pi\sigma z + \phi$ , phase term.

$g(z)$  = fringe envelope or coherence function.

From the equation it is seen that there are four unknown terms while in the case of using a monochromatic source there are only three unknown terms. This may be explained by

the fact that when using a monochromatic source the degree of mutual coherence term  $g(z)$  is equal to one. In the past white-light interferometer has been shown unsuitable for use with phase-shifting algorithms. However the algorithm proposed by Sandoz<sup>75</sup> overcomes the fact that the phase gradually changes over the region of the coherence envelope. The modification of transforming the standard four-point method to a seven-point algorithm with a  $90^\circ$  phase shift is made.

$$\phi = \tan^{-1} \frac{3I_{-1} + I_3 - I_{-3} + I_0}{4I_0 - 2I_{-2} + 2I_2}$$

The algorithm is based on the assumption that the coherence envelope is linear over a phase variation of  $3\pi$  (or 1.5 of a fringe). From this calculation the relative phase may be calculated though this value is not sufficient in the calculation of the surface height as the absolute phase must be known. To ascertain the absolute phase the fringe order is considered, though this calculation is only possible with white light interferometer and must be determined from the coherence function. The fringe order is found by calculating the visibility relative to the phase and this visibility value is then used in conjunction with the reference table to deduce the position of the fringe order to where it belongs. By combining the visibility and the relative phase it is possible to calculate the absolute phase, thus making it possible to determine the surface height. It has been shown that for a white light source, the error in the phase measurement is lower than 0.1rad for the four central fringes.

## CHAPTER 4: DEVELOPMENT OF WHITE LIGHT PROFILOMETER.

### 4.1 Optical setup

The optical setup of the white light system that was designed and developed is shown below in figure 4.10. All data acquisition is controlled and processed by several LabVIEW sub-programs that were specially developed for the white light profiler. These programs perform three major functions; the control and movement of the DC Motor and PZT; the capture of the fringe data from the camera and finally the processing of these to produce the final 3D map of the surface. The programs and algorithms will be discussed in more detail in the following section. The system is relatively portable though it is fastened to an optical bench, to reduce the amount of vibration that the system is subjected to. Specifications of all the main components that are used in the system can be seen in Appendix A.

The setup is based on a Michelson interferometer with one of the mirrors being replaced by the sample that is to be scanned. A tungsten filament light source with a coherence length of approximately 1-2 $\mu\text{m}$ , produces a stable illumination that is then launched into a multimode optical fibre. The main reason for using the optical fibre is that the light source does not need to be directly mounted on the system thus making it portable. The aperture stop hinders all stray light from reaching the collimation lens and aids in the collimation of the light beams. The lens is an achromatic lens with a focal length of 16 mm. Collimation of the light is accomplished by placing a mirror at a slight tilt in the path of the light beam, as collimated light is reflected from the mirror the rays pass back through the lens and focus back off centre onto the aperture stop. By changing the lens position one changes where the rays focus. Once a focus point is located the light beam entering the system should be properly collimated. The interference filter (bandwidth  $\approx 80$  nm) serves the purpose of decreasing the bandwidth of the light source thus increasing the coherence length of the source that makes it easier to detect white light fringes. Proper alignment of the two mirrors of the system is critical for accurate scans to be taken. Alignment is achieved by replacing the tungsten filament with a laser. The system is built in such a way that it is an easy process to detach the white light arm and replace with a beamsplitter to project the laser beam into the system. As the laser beam is split by the beamsplitter in the interferometer it travels both arms

of the interferometer and is reflected from the surfaces of the mirrors. If the mirrors are properly aligned then the reflected laser beams should overlap and if this is not the case both mirrors should be adjusted by tilting the mirrors in relation to one another until the beams overlap.

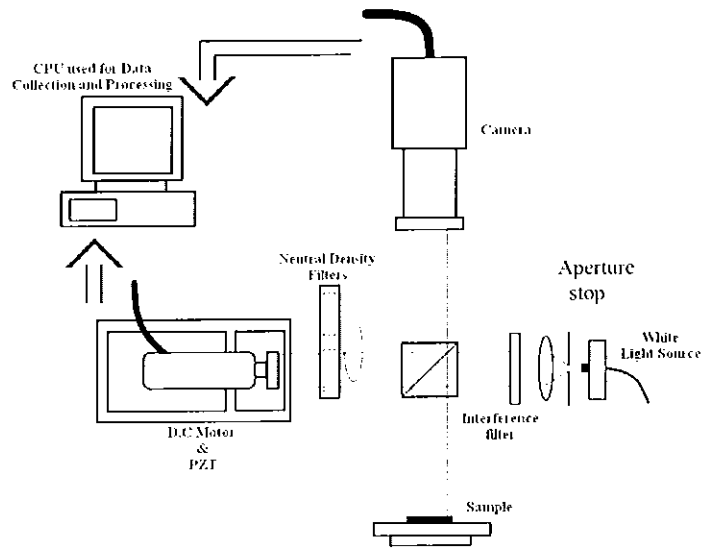


Fig 4.1 Optical setup of white light interferometer using LabVIEW.

When the two reflecting beams overlap, slight interference may be observed. With the mirrors aligned by overlapping the beams the alignment of the mirrors is checked over the full range of 2.5 cm for the DC motor. This is accomplished by placing an objective lens into the system that has the effect of diverging the laser beam, producing concentric fringes in the viewing plane of the interferometer. The reference mirror is then scanned over the full range of the DC motor with the fringe pattern of the laser being used to guarantee alignment in the z-direction. This is achieved by centering the concentric fringes produced by the laser and if the system is aligned correctly then as the DC motor translates across its range the centre fringes should remain in the same location across the scan. Once the mirror alignment is checked, the mirror is then returned to its original position where scanning for an optical path difference of zero between the two mirrors may commence. As the DC motor changes the optical path between the mirrors, the concentric fringes move towards the centre or away from the centre of the fringe pattern. If the mirror is moving towards an optical path difference of zero the fringes will appear to move into the centre of the pattern, until finally a position is



reached where the central fringe covers the entire field of view. If the mirror continues in its movement further fringes appear to grow out from the centre. If the system is properly aligned for an optical path difference of zero, one fringe should be seen to cover the entire field of view. If the laser is then replaced with the white light source, fringes can be seen to fill the CCD array and each pixel will modulate as the optical path changes. These fringes are then digitised by the frame grabber and analysed by the computer. The fastest procedure for achieving optical path difference of zero using white light will be outlined below.

Firstly the object mirror, the mirror on which the sample will be placed should be placed in the focal plane of the camera lens. As the camera lens has a small depth of focus care must be taken in the focusing of the mirror. This is achieved by scattering light off the surface and focusing the camera on any dust particles that may be present. The reference mirror is then moved into the focal plane of the camera lens, again focusing on dust particles that may lie on the surface. As the two mirrors are now positioned at the focal plane of the lens the location of interference fringes is made easier. Once the two mirrors have been positioned in such a way, the optical path difference of zero is found in a region of  $600\mu\text{m}$  either side of its centre. Using the interference filter at this stage makes the location of the coherence envelope much easier as it decreases the bandwidth of the white light source, thus increasing the coherence region where interference should occur.

To profile a surface, the sample is placed on the sample mirror and the focus position for the sample is found in the same way as above. The reference mirror is then moved to a position that is just outside the coherence envelope of the source. Once this position is reached the coherence peak detection program is started and the scanning process continues until the end of the scan. These frames are quickly gathered and analysed, the interference region is located for every pixel in terms of the frame number in which it occurred. The algorithm and the program in general will be discussed in greater detail later in this chapter.

The lateral resolution of the system will depend on the magnification of the imaging optics. The current profiling system has a field of view of  $3\text{mm}^2$  that is projected onto an array size of  $5\text{mm} \times 4\text{mm}$ . This results in a magnification of approximately 1.7X, the CCD array comprises an array of  $768 \times 576$  pixels each with dimensions of  $6.5\mu\text{m} \times 6.2\mu\text{m}$ . Therefore an

area of  $5\text{mm} \times 4\text{mm}$  will provide a lateral resolution of  $4\mu\text{m}$ . The current white light interferometer (WLI) is a development of a system that was constructed by Bove<sup>76</sup> and shown in figure 4.2.

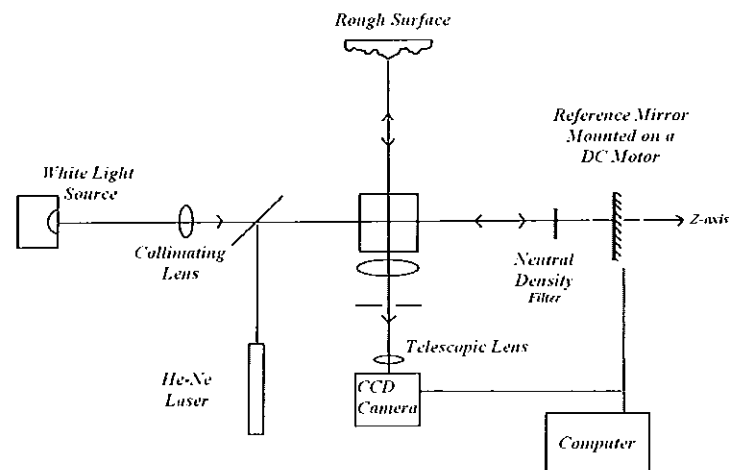


Fig 4.2 Optical configuration of original WLI.

The current completed system shown in figure 4.1 has several improvements on the previous setup in figure 4.2. These improvements include a more compact system, increased vertical and lateral resolution, the incorporation of a PZT and the development of both a coherence peak detection program and phase shifting program which were executed using LabVIEW.

## 4.2 Algorithms

Due to the phase ambiguity problems associated with surface profiling while using phase shifting interferometry with monochromatic light, it is impossible to profile a step height that is greater than a quarter the wavelength of the light source. As white light has such a short coherence length, fringes of varying contrast may be observed as two beams interfere and as a result this property may then be used to obtain a 3D profile of a sample.

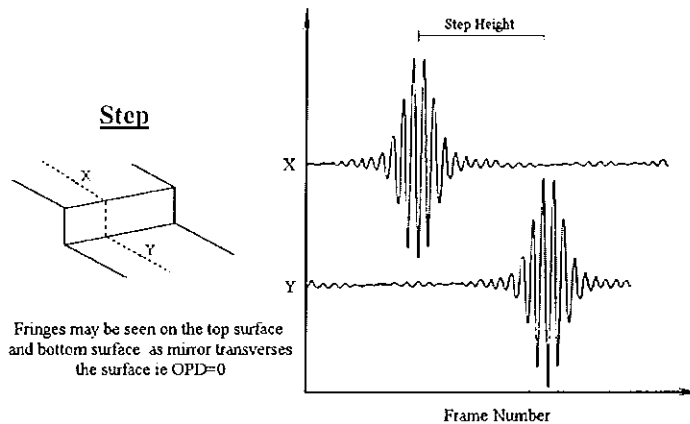


Fig. 4.3. Intensity pattern produced by reflective optical step.

If the step in figure 4.3 is placed in one of the arms of the profiler and the sample is scanned, pixels X and Y will modulate with an intensity which is shown in the chart. By locating the frame in which the maximum or minimum intensity occurs it is possible to calculate the height difference between the two points if the step size of the motor between frames is previously known. For example if the step size is  $0.06 \mu\text{m}$  and the maximum modulation for point X occurs at frame location 50 and maximum modulation for point Y occurs at frame location 120. The height variation is found ( $70 * 0.06 \mu\text{m}$ ) to be  $4.2 \mu\text{m}$ . This principle may be applied to every pixel on the CCD array. Therefore it is possible to build up a three dimensional view of the surface.

The main coherence detection program works by locating the frame where the maximum and minimum intensity values occur for every pixel in the array. Before the scan takes place the step size of the scan must first be determined as in figure 4.4. There are many other means of defining the step size but the method used in the coherence detection program has two important advantages in minimising the duration of the scan and reducing the computation load on the CPU. The length of scan (LoS) is calculated by defining the region when fringes just appear (Startpoint) and disappear (Finishpoint) in the plane of view. The (Step size) required for the movement of the DC Motor is determined by dividing the LoS of scan by 255.

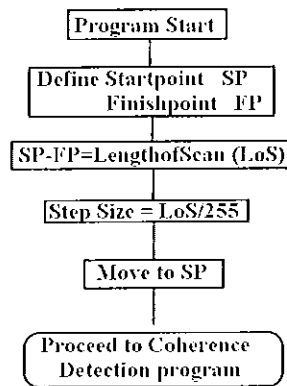


Fig. 4.4 Determination of the step size.

The disadvantage of using the above method is that if the calculated step size is greater than the region in which fringes may be seen, then the intensity values of the maximum and minimum location will appear to be under sampled. For example if a 1mm step is placed in the profiler the above method would calculate “LoS” to be 16667 steps ( $16667 \times 0.06 \mu\text{m} = 1 \text{ mm}$ ) as the minimum step of the DC motor is  $0.06 \mu\text{m}$ . From this the “Step Size” is calculated to be 66 and this means for the above method the DC motor will move a distance of  $3.96 \mu\text{m}$  ( $66 \times 0.06 \mu\text{m}$ ) between each incoming frame of data. When using the interference filter the coherence region exists for a movement of the DC motor of approximately  $18 \mu\text{m}$ , this means that between 4-5 frames of fringe data will be taken in the calculation of the location of maximum and minimum intensity values. The result of this is that much of the detail in the nature of the step will be lost when the profiled step is large. Another disadvantage is that the resolution changes depending on the length of scan. This can be easily changed by manually setting the step size in the program though the CPU takes longer to calculate the coherence peak for each pixel and the length of scan is increased. The reason for the 255 is that the frame number location is defined as 1-byte integer thus reducing storage and increasing calculation speed. Consequently the program runs faster and the computation burden is kept to a minimum.

### 4.2.1 Coherence Peak Detection

Ideally to extract the coherence peak all sampled data points on the coherence envelope should be stored and analysis carried out after the scan is complete. The 768\*576 array requires approximately 0.4MB to be stored in the shift register, and a further 255 frames at least would need to be collected to obtain the coherence envelope. Therefore to calculate the coherence peak a file size in excess of 11MB would be generated which is not practical. With an indexed array that contains 442368 elements it is essential to run the program as quickly as possible. A simpler method would be to use shift registers in which temporal values of the intensity maximum and minimum are stored, together with the frame numbers at which these extremities occurred.

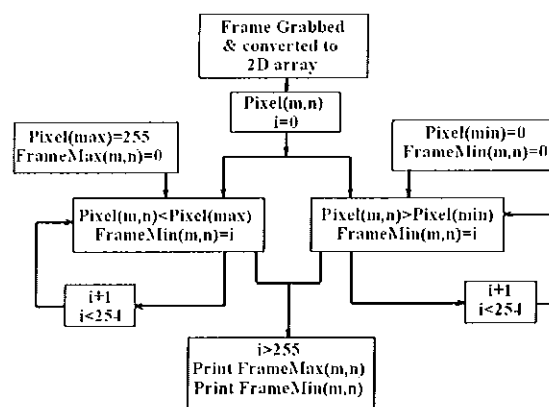


Fig 4.5 Flow diagram for coherence peak detection program.

Initially just four shift registers were used in the calculation of the position of the maximum and minimum intensity values. These four registers can be seen in the flow diagram in figure 4.5 where Pixel(max) stores the maximum pixel intensity, FrameMax(m,n) stores the location of the frame to where the maximum pixel intensity occurred, Pixel(min) stores the minimum pixel intensity and finally FrameMin(m,n) stores the frame location of where the minimum pixel intensity occurred. Once the program starts the intensity values are grabbed by the CCD camera and converted to a 2D array of greyscale values ranging from 0-255(black-white). As the DC motor is stepped to the required distance, the incoming frames of intensity values are compared with the previously stored data values. i.e. for the first iteration for “i=0” the pixel (max)=255 and the framemax=0, and if the incoming pixels at that point are less than

the start value(255-white) they are replaced and the frame number recorded as to where the pixel max occurred. If the incoming values are not greater than the maximum value, no change is made to the register.

At the end of the scan a 2D array of values corresponding to the frame location of both the maximum and minimum values is obtained. Either of these arrays may then be used to obtain a 3D view of the surface distance in relation to the frame location of both the maximum or minimum array values. The program runs relatively fast but the main concern is the period of time in finding the coherence region as it usually takes approximately 5-6 minutes. It was originally thought that the reason for such a slow scan was to do with the movement of the DC motor.

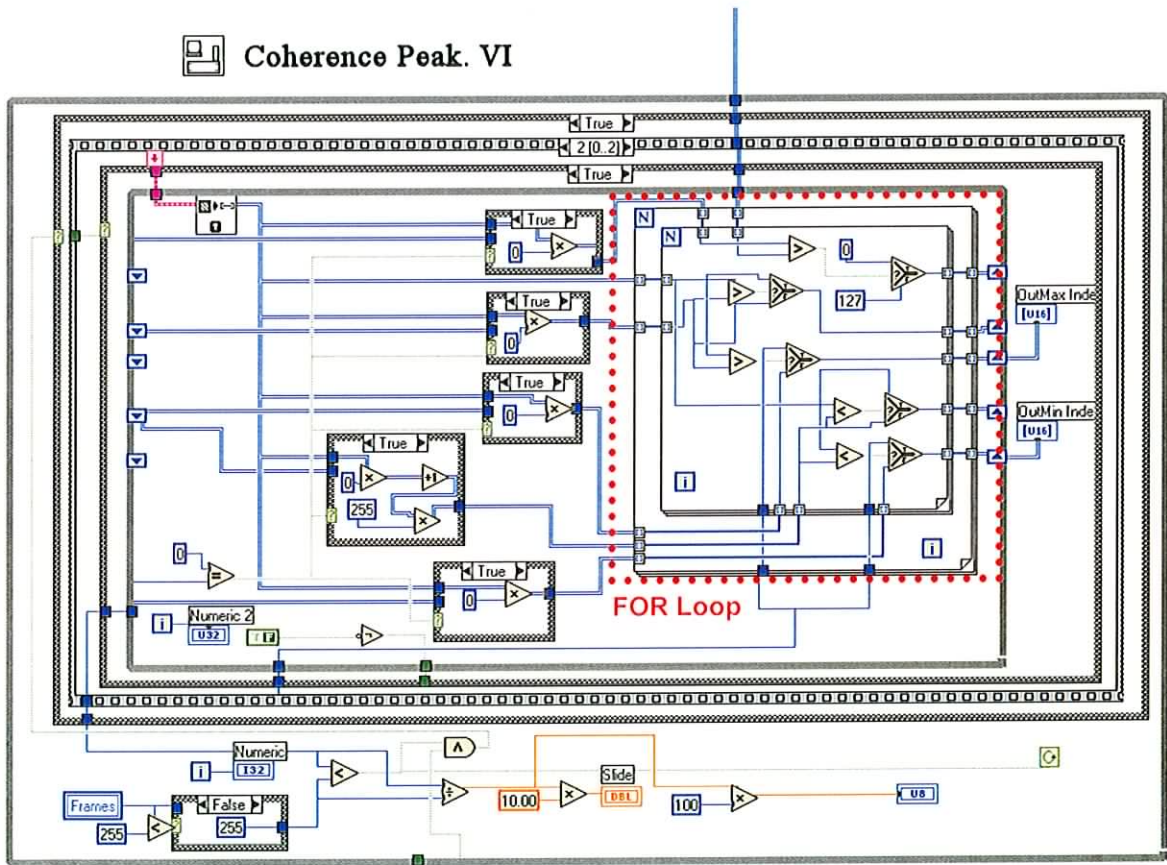


Fig. 4.6 LabVIEW program, coherence peak detection.

To determine the effect of the computation load on the overall speed of the program the shift registers are omitted from the program to analyse the speed of acquiring the frames and the movement of the DC motor was analysed. By removing the FOR loop from figure 4.6

the computation speed was assessed and it was found that the program ran 5 times faster. One means of improving the speed of the coherence peak detection program would be to reduce the number of data points but this reduces the field of view or sampling every tenth point in the array. However the disadvantage of sampling is that the spatial resolution of the profiler is also reduced.

The DC motor mounted on the profiler has a range of 2.5 cm, a quoted minimum increment of 0.06  $\mu\text{m}$  and a repeatability of 2  $\mu\text{m}$ . Therefore it is possible to measure step sizes in the range of 4  $\mu\text{m}$  to 2.5 cm with an error of  $\pm 2 \mu\text{m}$ . The VI or the programming interface that is used to control the DC motor may be seen in figure 4.7.

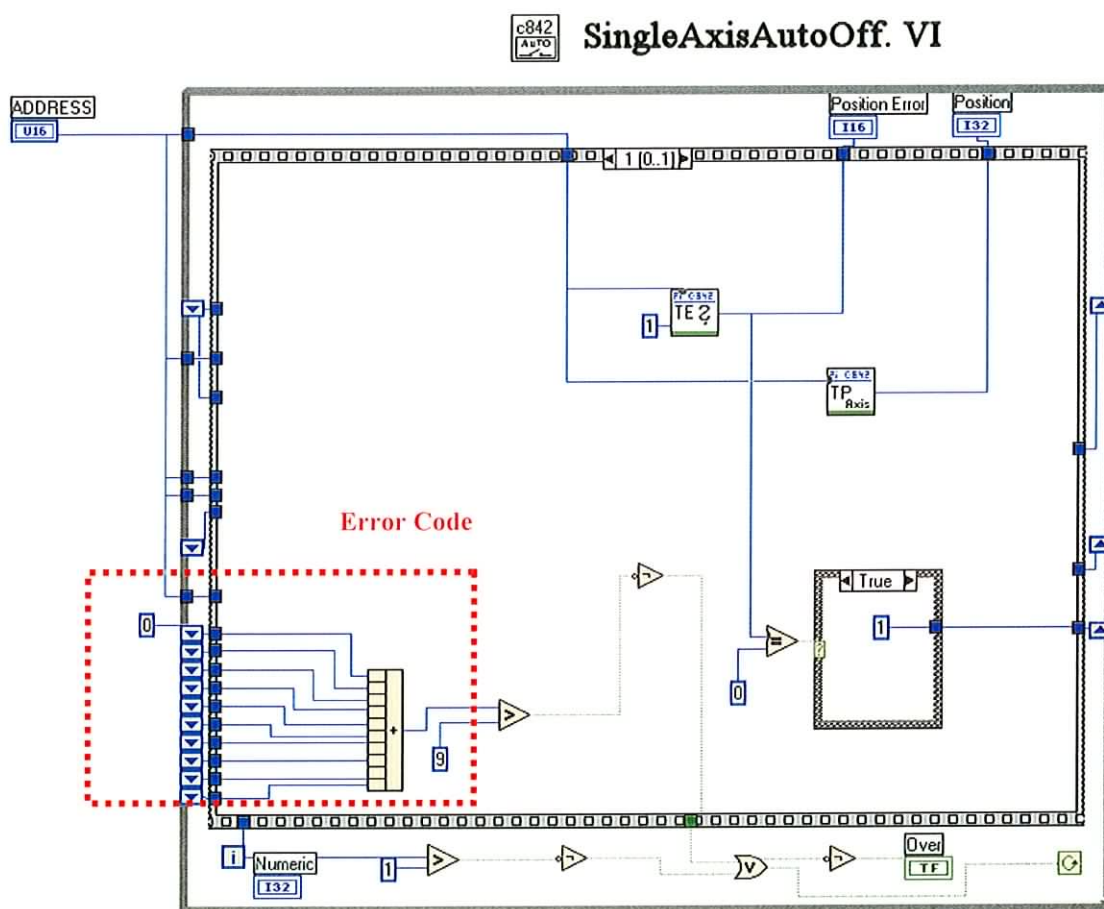


Fig 4.7 Back panel of VI used to control the DC motor.

The DC motor is controlled by an ISA interface card that slots into the back of any PC and is controlled using a computer program, in this case LabVIEW. Customised LabVIEW

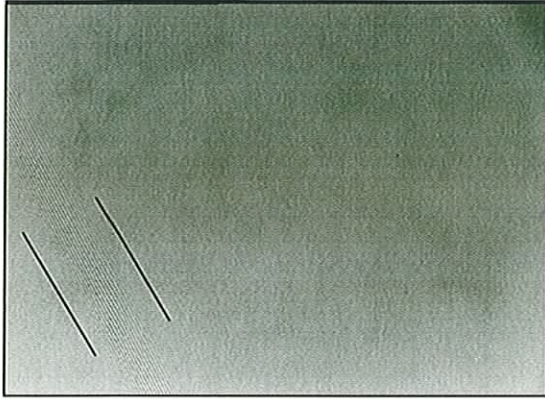
drivers to control the device had already been supplied with the device, therefore it was a matter of amending these to suit the needs of the application.

It was noted that when the motor arrived at its final position location the values seemed to float and did not settle immediately. An extra segment of code was added to counter this, by examining the position error of the motor and checking that it was zero for a length of time. This extra piece of code may be seen in figure 4.7 labelled “error code”. In this way it was assured that the value had settled to its final reading before the program proceeds to capturing a frame of data.

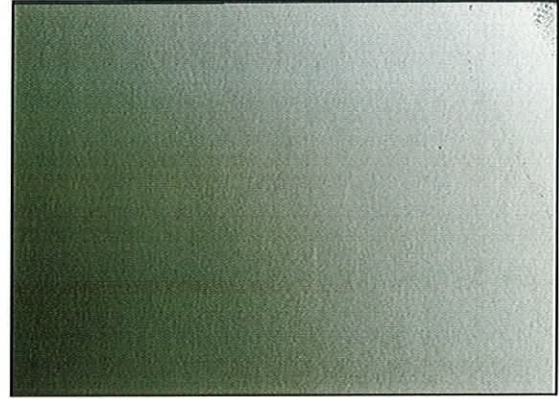
### **4.3 Results**

One of the first experiments that was carried out on the system was in calculating the maximum amount of tilt that the profiler could be subjected to before fringes were lost. This would show the maximum slope surface that the profiler could measure.





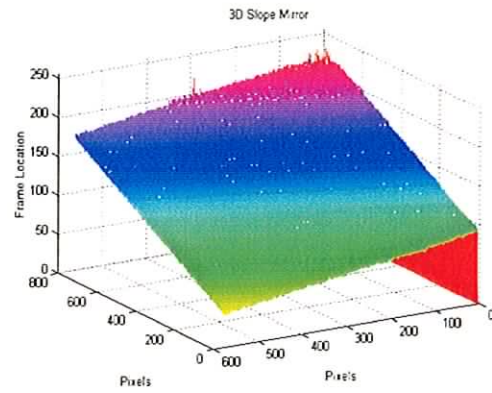
**A. Fringes taken before scan.**



**B. Frame location, Maximum Location.**



**C. Frame location, Minimum Location.**



**D. 3D Plot, Maximum location set.**

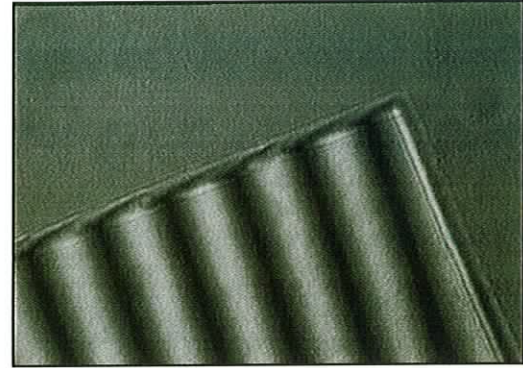
**Fig. 4.8. Scan of sloped mirror.**

In figure 4.8A fringes just about visible in the bottom left of the image. These fringes transverse the screen in a left to right direction and were used to find the maximum and minimum frame location. With a step movement of 6 or  $0.36 \mu\text{m}$  ( $6 \times 0.06\mu\text{m}$ ), the total scan length ( $6 \times 0.06 \mu\text{m} \times 255$ ) is  $92\mu\text{m}$ . Working with these values the maximum tilt that the profiler can measure is  $0.904^\circ$ . Also from figure 4.8B and figure 4.8C the maximum and minimum frame location are seen when they are plotted as a grey scale image.

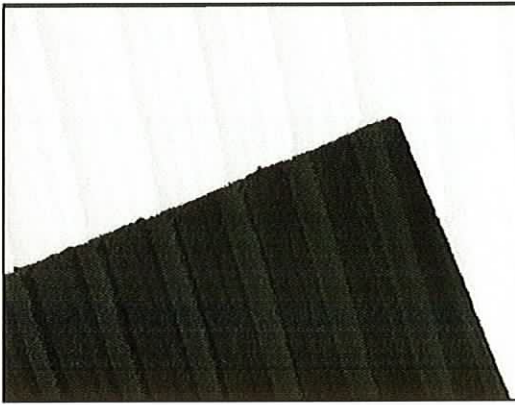
### 4.3.1 Optical Steps



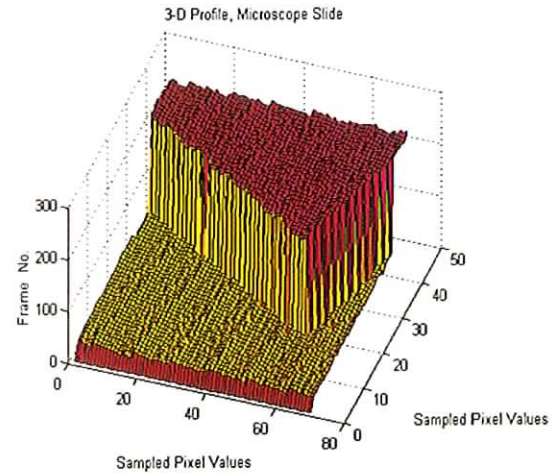
A. Fringes seen on mirror surface.



B. Fringes seen from top of glass slide.



C. Grey scale map of frame position



D. 3-D plot of optical step.

Fig 4.9 Coherence peak detection using an optical step.

As the interferometer is capable of measuring the profile of a surface it is also possible to measure the optical thickness of transparent materials. By measuring the optical thickness of a sample it is possible to work out the physical thickness, if the refractive index of the material is known. The profiler may also be used in reverse to find the refractive index by knowing the actual thickness and the optical thickness. The equation that links all these quantities follows:

$$t_{Act.} = \frac{t_{Opt.}}{(n_1 - n_0)} \quad (4.1)$$

$t_{Act.}$  = thickness, where  $n_1$  and  $n_0$  refractive index of the material and air respectively.

Initially white light fringes were obtained and both mirrors were adjusted so that 7-8 fringes could be seen on the CCD camera. By placing a microscope slide on the surface of the object mirror, partially covering the image had the effect of changing the optical path in the arm of the interferometer. If the optical path created by the material is greater than the coherence length of the light source fringes will not be seen as in figure 4.9A. By moving the mirror to correct for this optical path change it is possible to obtain the thickness of the mirror by solving equation 4.1. Figure 4.9B shows fringes that exist when the object arm is moved to compensate for the change in the optical path distance. This example shows the main problem with the program in its current form, arising as a result of the step height being calculated from the start and finish points of a scan. As a result it is possible that the interference region will be under sampled, with the loss of data at some of the pixels in figure 4.8C. The grey scale map for the frame locations represents the locations where maximum modulation was recorded for the coherence peak detection program. From the 3D plot (note that the graph is sampled for every 10<sup>th</sup> point) the step height is approximately equivalent to 177 frames. The optical thickness may be calculated by multiplying the height in frames by the distance moved between each frame. With a step size of 0.48 $\mu\text{m}$  ( $8 \times 0.06\mu\text{m}$ ), an optical step of 84.96  $\mu\text{m}$  is calculated. By applying equation 4.1 the actual thickness on the step may be calculated to be 56.06  $\mu\text{m} \pm 0.24\mu\text{m}$  if a refractive index of the glass is assumed.

### 4.3.2 Silica Steps

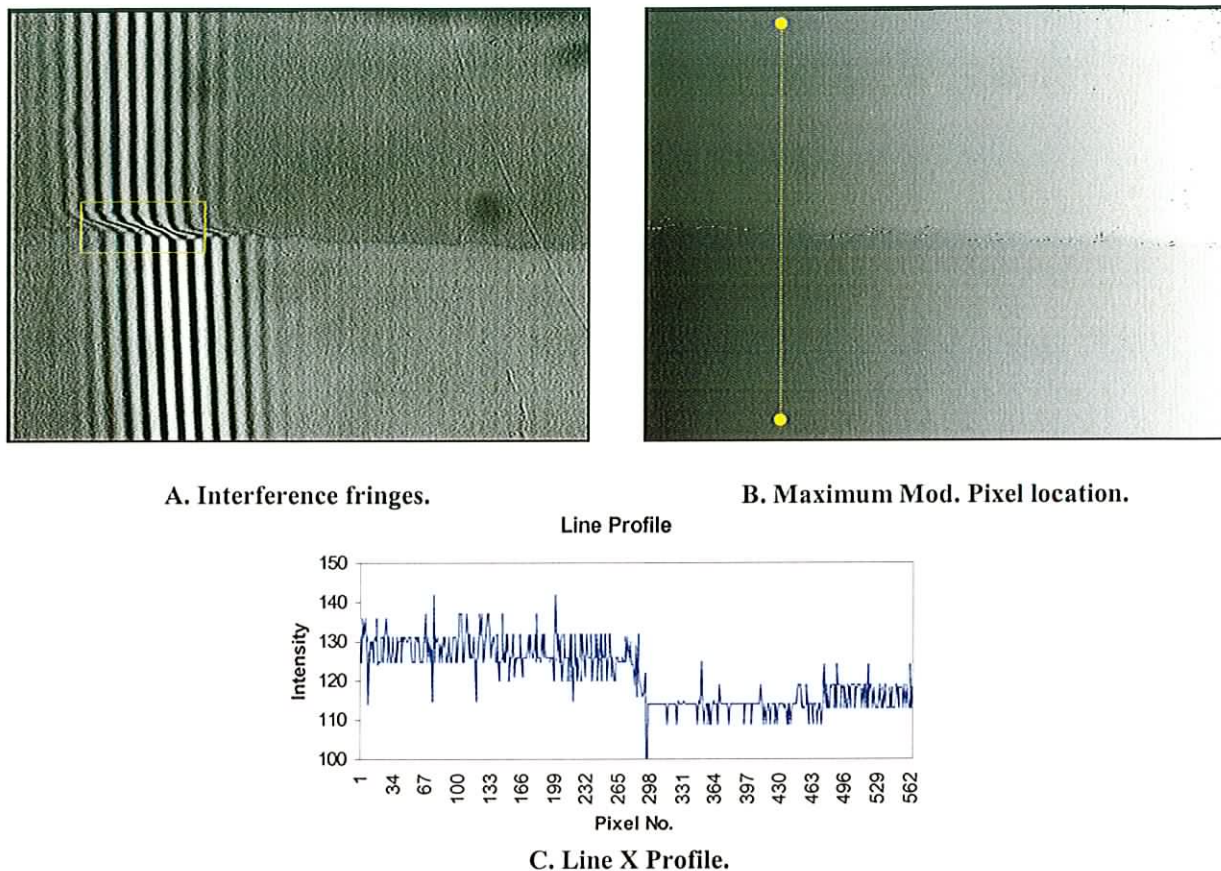


Fig 4.10 Fringes plus profile of Silica Step.

By replacing the mirror in the object arm with a stepped silica sample it is possible to profile the step on the surface. By placing the sample on the object mirror of the profiler the optical path is changed in the arm of the interferometer. By moving the reference mirror to compensate for the difference in optical path it is possible to locate the position of the interference fringes, and then using the coherence peak detection program it is possible to obtain a surface profile for the sample. The silica sample is comprised of silicon dioxide which has a layer of silica nitrate deposited onto its surface. Part of the silica nitrate layer is then etched away to produce a surface step on the surface of the wafer. The surface of the silica may be profiled using the coherence peak detection program. As may be seen from the silica sample of figure 4.10A the interference fringes are displaced by the variation in the height of the step. It is important to note that though the interference filter was used to find the location of the interference fringes, it wasn't used in scanning the profile of the silica and was

replaced with a bandpass 500 nm filter to obtain the set of fringes. The fringes move in a left to right direction and two sets of frame locations were obtained both maximum and minimum though only the maximum is displayed in figure 4.10B. A line profile, figure 4.10C, was taken across the image of maximum pixel modulation location, yellow line. The variation in the two surfaces can be seen to be approximately 14 pixels, with a step of  $0.06\mu\text{m}$ , corresponding to a surface height of  $0.84\mu\text{m} \pm 0.06\mu\text{m}$ . This compares favourably with a calibrated step size of  $0.81\mu\text{m}$ .

From the silca sample in figure 4.10 it can be seen that there are some pixels at the boundary of the step that are of a much greater or lower intensity in comparison to the sum of their neighbouring pixels. These non-modulating pixels are caused mainly because of light from that region, not being reflected back to the CCD array. This is caused when the step is gradual and not clear and sharp, light is reflected away from the array. Other sources of error include diffraction effects at the edges, shadows on the surface and dirt on the surface or array, all of which contribute to non-modulating pixels.

These modulation errors may be removed by image processing. An approach would be to isolate the non-modulating pixel then sum the surrounding 8 pixels and find their average value i.e. median filter. This average value would then be substituted into the non-modulating pixel.

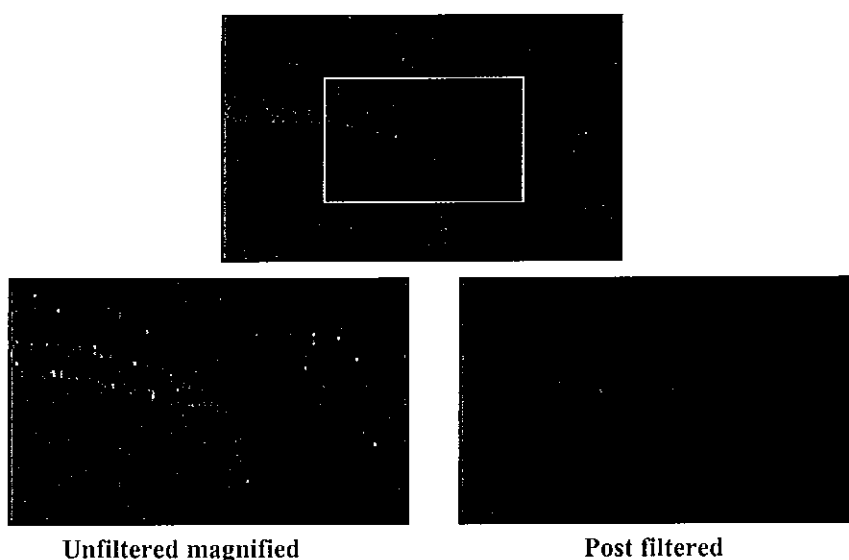
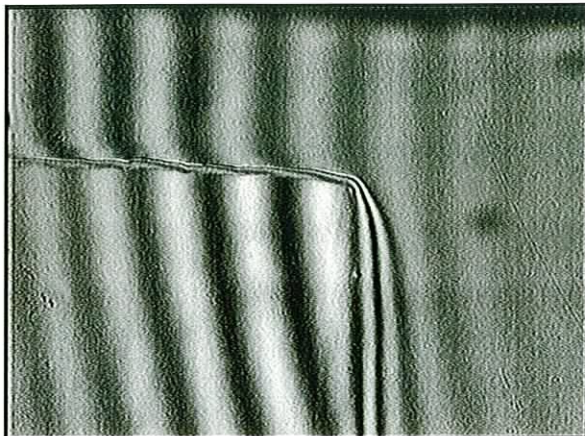


**Fig. 4.11. Median filter applied to a noisy image.**

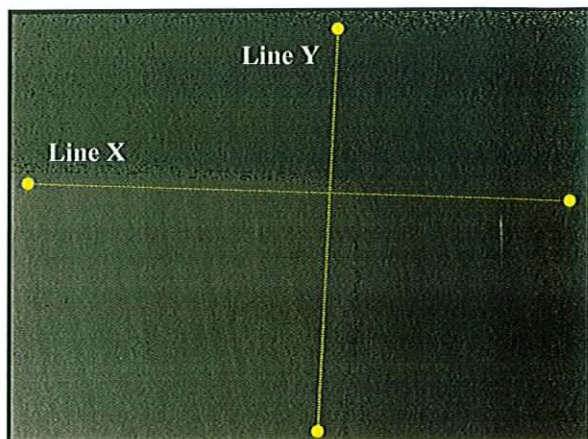
This process would then proceed to the remaining pixels in the array removing pixel errors. The one drawback is that the filter does not perform efficiently in areas where large amounts of errors occur but may be improved though not eliminated by a median filter. Due to the fact that noise appears as “salt&pepper” or random variation in white and black pixels it was found that using a modified median filter that had a kernel size of 5×5 gave best results in removing non-modulating pixels. In the above case a 5 kernel size was used, the intensity values of the 25 pixels are sorted and the 13<sup>th</sup> value is replaced in the centroid of the kernel. The effect of the median filter on image may be seen in the figure 4.11.

A second silica sample was profiled in the same way as the first sample by placing it in the object arm of the interferometer. Once the mirrors are properly aligned one or both of the mirrors are tilted so the fringes appear on the surface of the silica sample. From figure 4.12B it is seen that the fringes transverse in direction from a right to left. This may be determined from the fact that the dark region or frame values from 0-50 appear on the right side of the image figure 4.12B with the bright region 0-255 on the left side of the image.

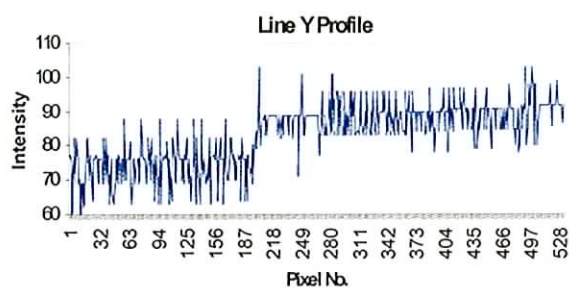
As may be seen from the image of figure 4.12C a much more pronounced step may be seen than in figure 4.11. By looking at the two profiles X, Y it might first be thought that the step is not uniform across the two surfaces. A gradual step is seen in the X profile while at discrete step of approximately 11 pixels exist along the line of profile Y. This apparent gradual step is in fact due to the tilt applied to the mirrors in making the fringes visible in a vertical direction. With a minimum step of the DC motor of 0.06µm a step of 0.66 µm exists between both surfaces. A 3D view of the silica step may also be observed in the figure.



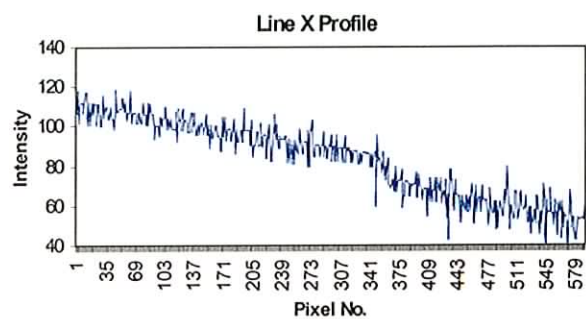
A. Fringes observed on silica step.



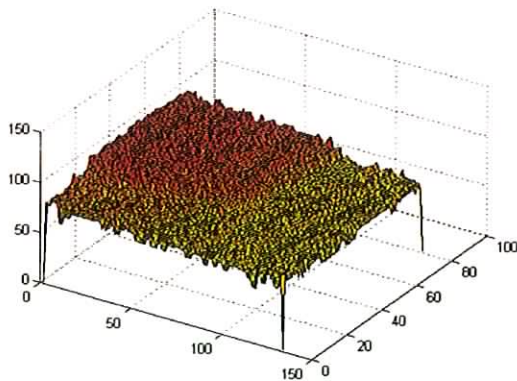
B. Maximum intensity frame location.



C. Line Profile.



D. Line Profile.



E. 3-D View of silica step

Fig 4.12. Profiles and 3-D views of silica steps.

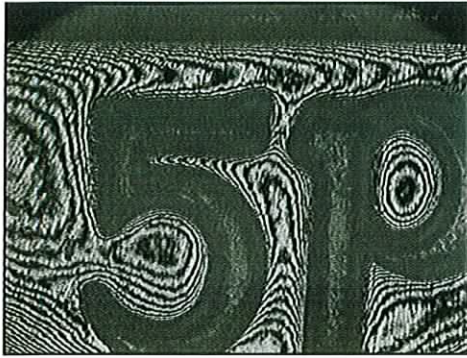
As silica is highly reflective it is a straight forward process obtaining profiles using the white light profiler. In the following example illustrated in figure 4.13 the capabilities of the profiler are demonstrated by profiling steps on coins. The sample under test is an Irish 5 pence piece and again before the scan takes place fringes are found on the surface, in this case the bottom surface of the step as in figure 4.13A. One problem that became evident when profiling coins was the quality of the imaging optics used to focus the rays of reflected light onto the CCD array. By looking at the sample image of the 5 pence piece figure 4.13B, it is seen that there are regions where the image appears defocused. Several alterations were made to improve the focusing including changing the orientation of the profiler so that the camera focused on the arm of the interferometer that contains the DC motor, though none of the alterations made any major improvement to the defocus nature of the image acquired from the CCD. As may be seen from figure 4.13C a good frame location map was obtained, as fringes moved from the top surface to the bottom surface. The scan was repeated though this time the fringes transverse from the bottom surface of the coin to the top surface and the resultant frame location map may be seen in figure 4.13D. A line profile was taken along the same path for both images C & D and shown in figure 4.13E and figure 4.13F respectively. From the line profile across the sample, a step of approximately 150 pixels exists. The step size for the scan was 8 or  $0.48 \mu\text{m}$ , and this corresponds to a step of  $72 \mu\text{m}$ .

Factors that affect the performance of the profiler when profiling coins include the amount of light reflected back to the camera and the effect of shadows in reducing the contrast of the image. It is very important to maximise contrast between the surface and the intensity of the fringes to obtain a profile that contains as few non-modulating pixel values as possible. Note that the 3D view of the coin in figure 4.13G is a sampled for every 5<sup>th</sup> point; this is why the image appears as a  $120 \times 150$  image. Also note that the z-axis represent the frame location of maximum modulation in the fringes and not the actual height of the sample under test.

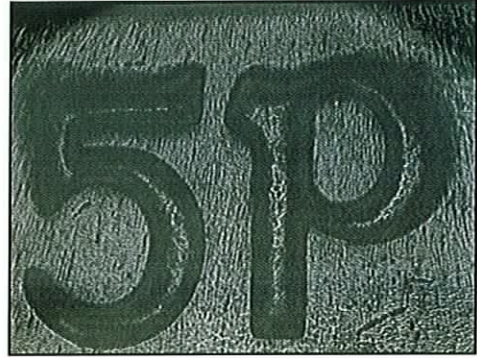
As may be seen from the results, the profiler has shown adequate results for steps greater than approximately 40 nm when a step size on  $0.06 \mu\text{m}$  is used. This is due the fact that it is difficult to differentiate a variation of 10 pixels. This limitation is due to the minimum step size of the DC motor and also the signal to noise ratio of the camera. The disadvantage of the current program setup is poor vertical resolution, this is due to the fact



that the step size is variable depending on the length of the scan. Also, due to the narrow depth of focus of the imaging lens for the CCD array, steps of greater than 1 mm may prove difficult to profile. It has been shown the coherence peak detection program is adept at profiling discontinuous surfaces though due to the minimum step size of 0.06  $\mu\text{m}$  smooth continuous surfaces are virtually impossible to profile correctly. This is overcome with the incorporation of a piezo electric transducer into the system and using phase shifting interferometry in obtaining the surface profile.



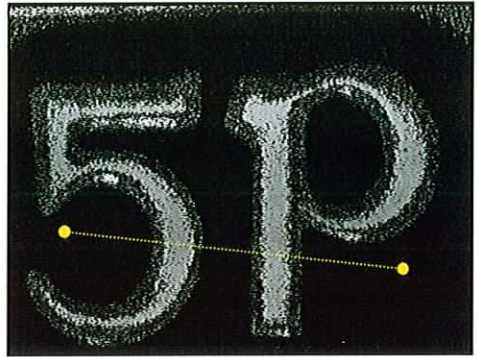
A. Interference fringes.



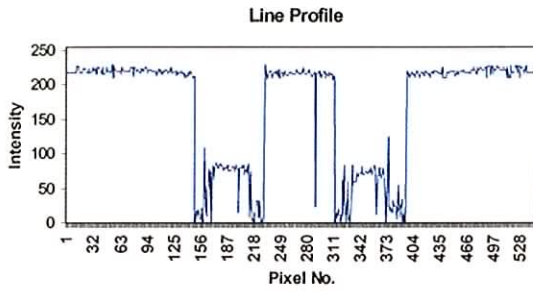
B. Sample image of scan.



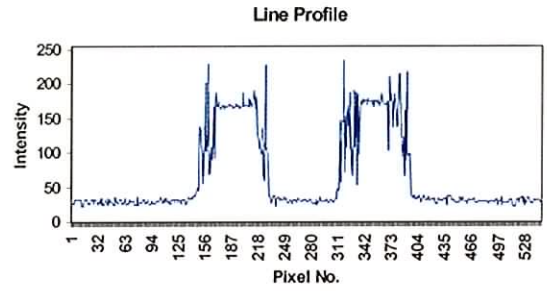
C. Max modulation fringes move top to bottom.



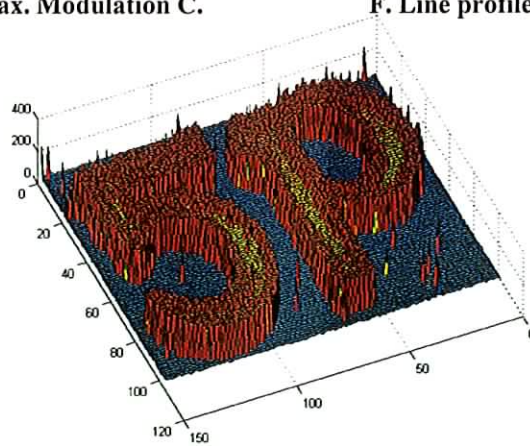
D. Max modulation fringes move bottom to top.



E. Line profile of Max. Modulation C.



F. Line profile of Max. Modulation D.



G. 3-D view of 5p piece.

Fig 4.13 Demonstration of the Coherence peak detection program on 5p piece.

## **CHAPTER 5: PHASE STEPPING INTERFEROMETRY**

### **5.1 Introduction**

The optical setup for phase stepping interferometer remains the same as for the coherence peak detection program as outlined in the last section. As mentioned in the previous section phase stepping is based on the fact that if the phase is varied by a predicted amount in one of the arms of the interferometer it is possible to calculate the original phase difference between the two interfering beams. The phase difference may be calculated by taking a minimum of three intensity readings and from this phase value it is possible to calculate the height of the surface. As mentioned earlier, there are many different approaches to modulating the phase in the reference arm of the interferometer though the most common method is using piezo-electric transducers (PZT). With the current system a mirror was placed on a PZT and mounted on the DC motor. Therefore fine movements of the mirror could be accomplished using the PZT with a minimum movement of 5nm while the DC motor was used for much coarser displacements with a minimum movement 0.06 $\mu$ m.

### **5.2 PZT Calibration**

Due to the hysteresis error that is found in piezo-electric transducers it was important to characterise the amount of error that is inherent in the device. To calibrate the transducer, a mirror is placed on top of the ceramic stack and placed in one arm of an interferometer. As the voltage across the PZT is gradually stepped, it has the effect of changing the optical path difference between the mirrors. The result of changing the optical path in the interferometer is that the fringes transverse across the plane of observation, the inherent hysteresis is quantified in figure 5.1.

By counting the number of fringes that move across a point, it is possible to determine the calibration chart for the PZT. It was found that to achieve the full displacement of 15  $\mu$ m for the PZT a voltage of 145V needed to be applied across the device. It was decided for the phase stepping application that the full scale of the PZT would not need to be used. If the full scale were to be used more sophisticated electronic components would be required in the amplification of the computer signal output to reach the required 140 volts across the PZT.

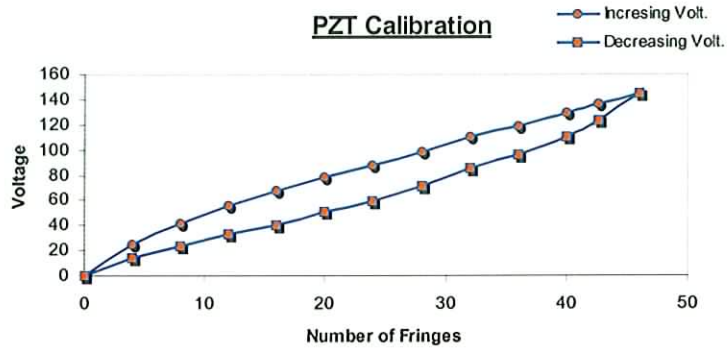


Fig 5.1. Calibration of the piezo-electric transducer.

When using phase stepping in a Michelson it is adequate that the phase shifting device can move a displacement  $\lambda/8$  to achieve an optical path difference change of  $\lambda/4$  remembering that for a Michelson interferometer that  $2 \times \text{OPD} = \lambda/2$ . The problem becomes one of finding the voltage required to move the PZT this distance. It was determined that to extend the PZT to its full range, 145 volts must be applied across the transducer, in the process this had the effect of displacing 46 fringes, for one wavelength; this corresponds to a voltage of 6.304 Volts ( $290/46$ ).

For the current phase stepping application, it is assumed that the response of the PZT is linear over such a small voltage range of 10-15 Volts. The voltage was supplied via a Thurby Thandar TSX3510P, the reason to use the Thurby Thandar was that the instrument was compatible with GPIB and serial connections allowed the instrument to be controlled automatically with the help of LabVIEW drivers.

### 5.3 Calibration Program Design

Before commencing the phase stepping program, the value of the incremented voltage must be determined for the current set of fringes. The reason for this is to achieve a step size as close as possible to the required step of  $90^\circ$ . It is important to note at this stage that the beams of interfering light must be collimated as closely as possible. If the beams are not properly collimated, there will be regions on the viewing plane where the phase values will stray greatly from the  $90^\circ$  shift. Three separate programs were written for the calculation of the step voltage.

Two of the programs that are used to determine the calibration voltage, fringe modulation and peak detection are based around the principle used in figure 5.2 above. Sixteen individual points are located on the pixel image and at each of these pixels, the intensity variation is measured.

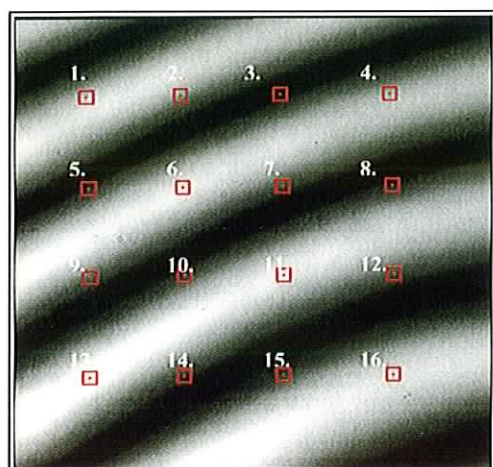


Fig 5.2 Position of 16 pixel points.

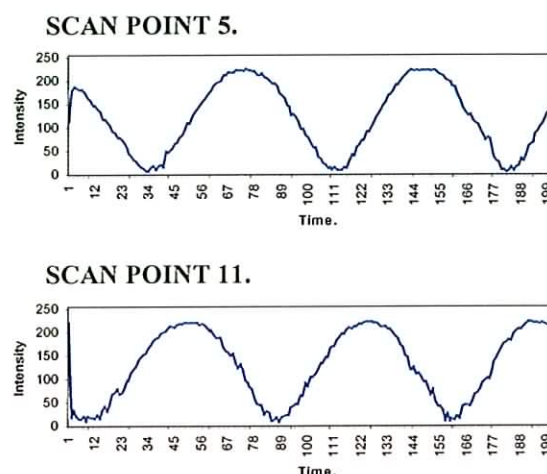
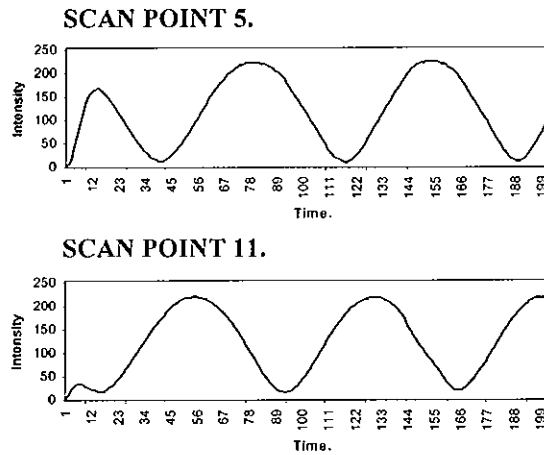


Fig 5.3 Profile of scan points.

### 5.3.1 Program No. 1: Voltage Calibration Fringe Detection

The calibration fringe program is set up so that the starting voltage and the finish voltage are variable but usually set to 5 volts and 15 volts respectively. From the starting voltage the voltage is incremented in steps of 0.05 volts, though this value is also changeable, until the finish voltage is reached when the program terminates. After each increment the intensity values of the sixteen pixels are recorded and stored. Therefore, in a complete scan of the pixel intensity 200 values are stored for each of the sixteen pixels as illustrated in figure 5.3.

Once the scan has taken place the user is given the option as to which of the 16 pixel variations will be used to calculate the increment voltage for the phase stepping program. The reason for this is that some of the pixels may not modulate due to dead pixels on the CCD array or dust or dirt on the mirror or array.



**Fig 5.4. Modulation points after filtering.**

The incremental voltage value for  $2\pi$  is then calculated by obtaining the frequency of the pixel modulation. As may be seen from figure 5.4 a deviation may be observed this is due to the high pixel variation over the i.e. region in figure 5.3. Due to this filter fluctuation the period of the wave may be calculated over a predefined range i.e. position 45 and position 177. The period of the wave may then be obtained and expressed as a voltage. This voltage is the step required to obtain a  $2\pi$  shift.

An average value for the  $2\pi$  shift is then obtained for the sixteen-pixel points and a  $90^\circ$  phase shift is found by dividing by 4. Two intensity modulations are shown in figure 5.4 which have been filtered to remove any noise on the signal. When the function is sampled between points 23 and 199 it is found that the signal has a period of  $75.18 \text{ sec}^{-1}$ . With a step of 0.05 Volts between measurement frames it is found that the  $2\pi$  voltage to be 3.76 volts. Therefore, to obtain a  $90^\circ$  phase shift a voltage of 0.94 volts must be used. Note that as mentioned earlier the shift voltage is dependent on the degree of collimation of the interfering beams. See figure 5.5 for the LabVIEW back diagram of the program.

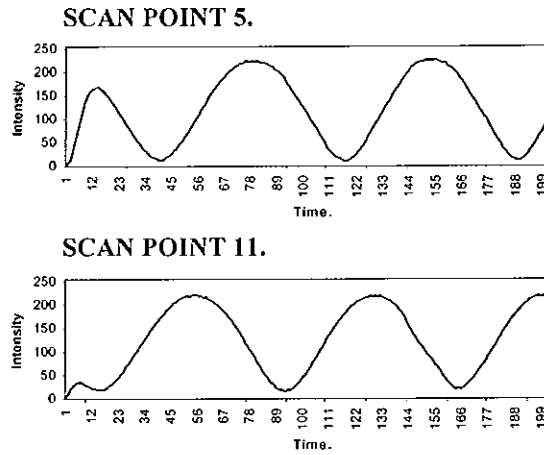


**Fig 5.4. Modulation points after filtering.**

The incremental voltage value for  $2\pi$  is then calculated by obtaining the frequency of the pixel modulation. As may be seen from figure 5.4 a deviation may be observed this is due to the high pixel variation over the i.e. region in figure 5.3. Due to this filter fluctuation the period of the wave may be calculated over a predefined range i.e. position 45 and position 177. The period of the wave may then be obtained and expressed as a voltage. This voltage is the step required to obtain a  $2\pi$  shift.

An average value for the  $2\pi$  shift is then obtained for the sixteen-pixel points and a  $90^\circ$  phase shift is found by dividing by 4. Two intensity modulations are shown in figure 5.4 which have been filtered to remove any noise on the signal. When the function is sampled between points 23 and 199 it is found that the signal has a period of  $75.18 \text{ sec}^{-1}$ . With a step of 0.05 Volts between measurement frames it is found that the  $2\pi$  voltage to be 3.76 volts. Therefore, to obtain a  $90^\circ$  phase shift a voltage of 0.94 volts must be used. Note that as mentioned earlier the shift voltage is dependent on the degree of collimation of the interfering beams. See figure 5.5 for the LabVIEW back diagram of the program.

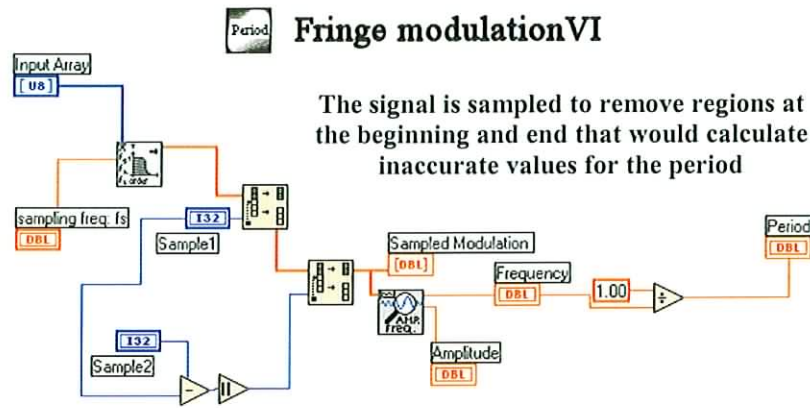


Fig 5.5. Back panel diagram for the Fringe modulation program.

### 5.3.2 Program No. 2: Voltage Calibration Peak Detection

For the peak detection method the original 16-pixel intensity modulations are used from figure 5.2 in detecting the period though the signal is not filtered in this case. The program may be seen in figure 5.6 and the algorithm is based on the principle that if the peaks of the signal may be detected, the period may be found and hence the calibration voltage calculated.

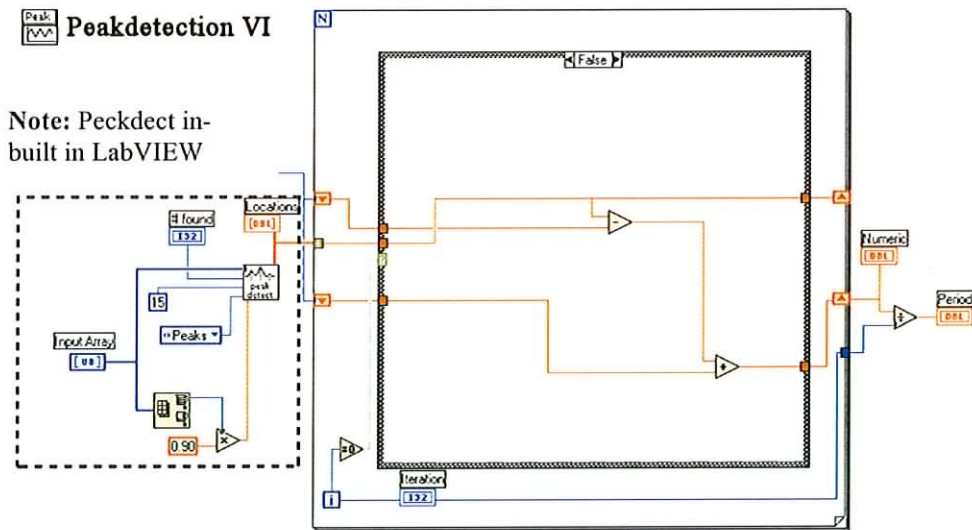


Fig 5.6. Back panel diagram for the Peak detection program.

From the diagram in figure 5.6 the original signal of the intensity modulation is represented by the input array. This array is then sent to the peak detect VI, which in turn



outputs the locations of peak values of the sine wave. These location values are placed on a shift register and processed to calculate the average period of the input array.

### 5.3.3 Program No. 3: Voltage Calibration Fringe Subtraction

Unlike the previous two approaches in obtaining the calibration voltage, frame subtraction offers a novel means of acquiring the voltage step. Imagine a set of fringes that may be observed on the image plane, if the optical path is changed the fringes shall move from their original position. If the optical path is changed by an order of the wavelength of the source the fringes shall appear unchanged from their starting position. Also if the optical path changes by half the order of the wavelength the fringes shall appear complementary to the starting fringes. Using this fact it is possible to construct an algorithm that can calculate the voltage step. The block diagram for the algorithm may be seen in figure 5.7 below with the LabVIEW diagram in figure 5.8.

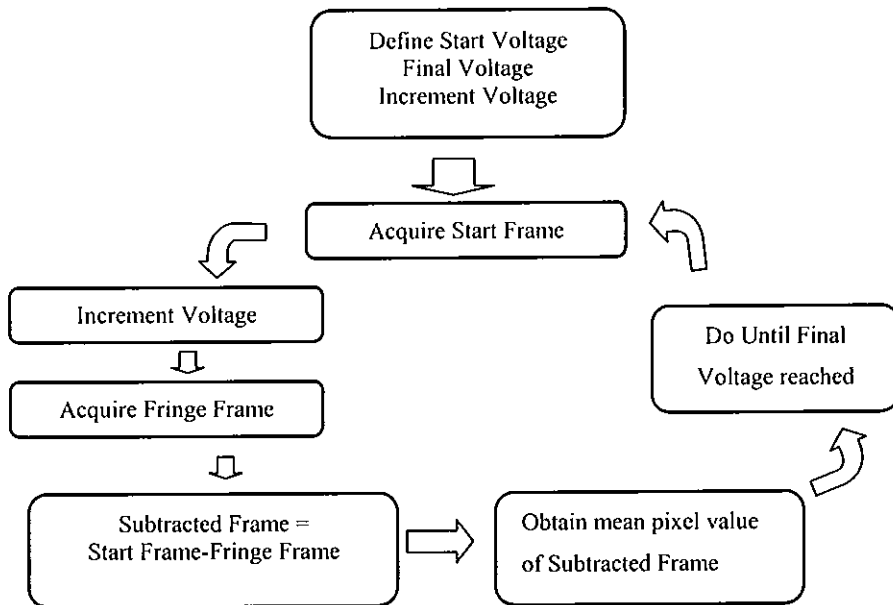


**Fig 5.7 Block diagram for Frame Subtraction Algorithm.**

Once the start, final and increment voltages have been defined on the user interface of the program an image is acquired of the fringes called the “start frame”. Due to the signal to noise (S/N) ratio of the camera five frames are grabbed and averaged to produce one frame.

This has the effect of reducing the S/N ratio by a factor of  $1/\sqrt{5}$ . The PZT steps the increment voltage and another five frames are averaged, the subtraction of the two averaged frames takes place and the mean pixel value of the resulting frame is calculated. Further fringe frames are acquired and the mean pixel value found for each subtraction from the “start frame” until the final voltage is reached. When the program terminates an array of values for the mean pixel values of the resulting frame is produced. When this array is plotted, it is seen that a sine function results. Again as described earlier by finding the period of the function, it is possible to calculate the calibrated voltage step.

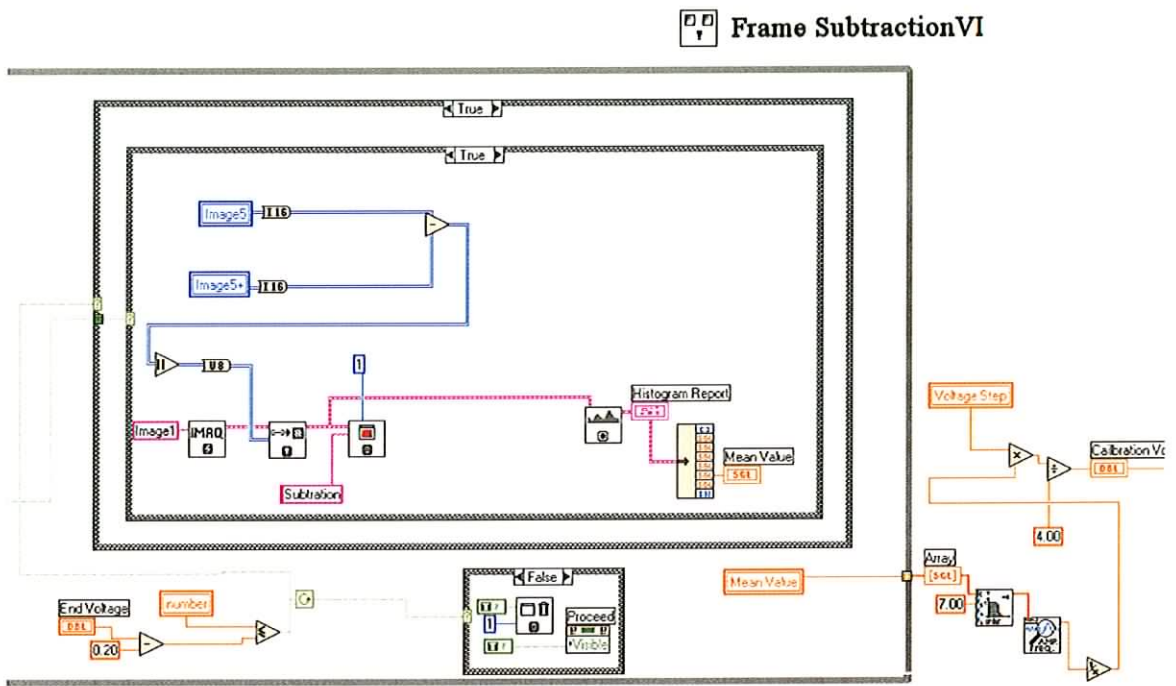


Fig 5.8. Back panel for Frame Subtraction Algorithm

Once the calibration voltage has been established for the optical setup, initialisation of the phase shifting program may take place. The back panel of the program may be seen in figure 5.9.

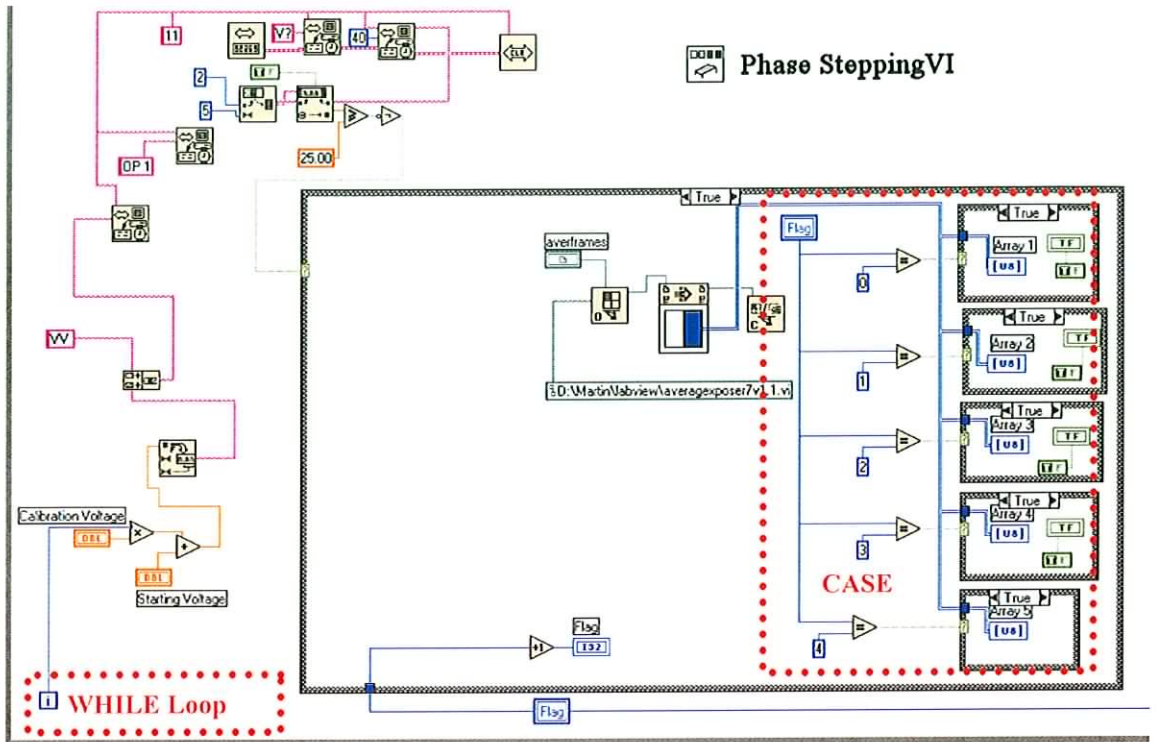


Fig 5.9. Back panel for the phase shifting program.

From the diagram it is seen that the program is based around a while loop. Each time there is an iteration of the WHILE loop, a voltage call is sent to the GPIB to set the output to a multiple value of the step voltage. Once this call is completed the case structure is activated and a frame is obtained from the CCD array depending on the value of the FLAG variable. This FLAG is important, with every iteration of the while loop the CASE structure is also activated, each time this case is activated the flag increment its current value by one, thus storing the incoming intensity values that will be used in the phase calculation.

The intensity frames are placed in arrays 1 to 5; the flag thus prevents the array 1-5 from being overwritten with new data from incoming data grabbed with each iteration of the WHILE loop.

Once the frames have been gathered the phase values may be calculated from the Hariharan<sup>64</sup> algorithm (equation 3.9) in the second part of the phase stepping program figure 5.10.

**Phase Stepping VI**

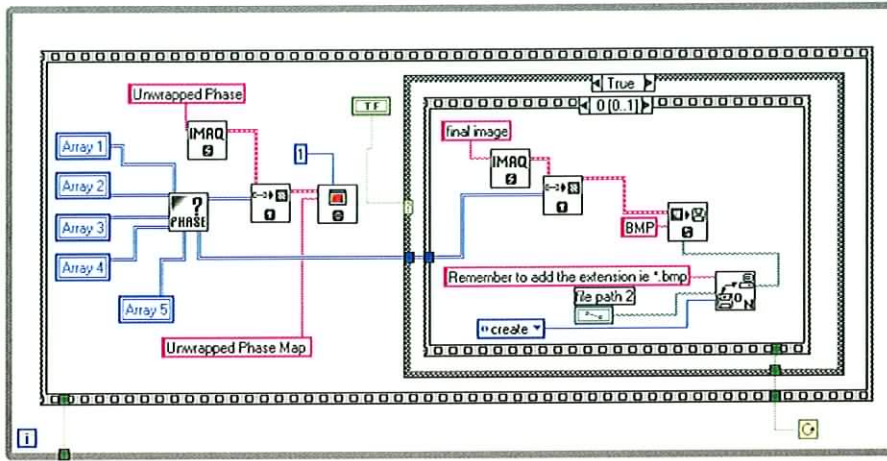


Fig 5.10. Phase value calculation.

The five intensity arrays, array1 to array5 are sent to the phase VI. The output for the phase VI, the unwrapped phase map is displayed on screen as an 8-bit image.

**Phase Calculation Han. VI**

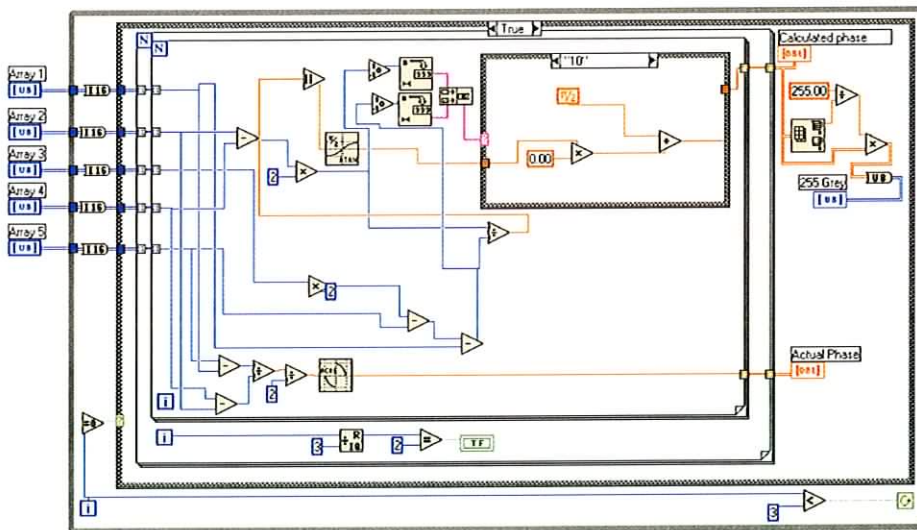


Fig 5.11 Back Panel for the Hariharan phase calculating VI.

Two VI's were written in calculating the phase map, the VI in figure 5.11 is based on the  $90^\circ$  shift and using five intensity reading to calculate the phase using the Hariharan method as outlined in Chapter 3. The second VI is based on using four images to calculate the phase, i.e. the standard four-bucket algorithm. As the calculated phase values are in the region of  $-\pi$  to  $\pi$  they must be modified to produce them in the region of 0 to  $2\pi$ . This is accomplished by the case structure and once calculated the phase values are converted to grey scale 8-bit for viewing.

### 5.4 Phase Stepping Results

Due to the limitation of phase stepping only samples that are continuous and that do not have steps greater than half the wavelength of the source may be profiled. Figure 5.12 contains the phase maps of multiple mirror measurement. These phase maps were obtained over a certain period of time; once one scan was completed the profiler was allowed to stand idle for no less than 1 minute before the next scan took place.

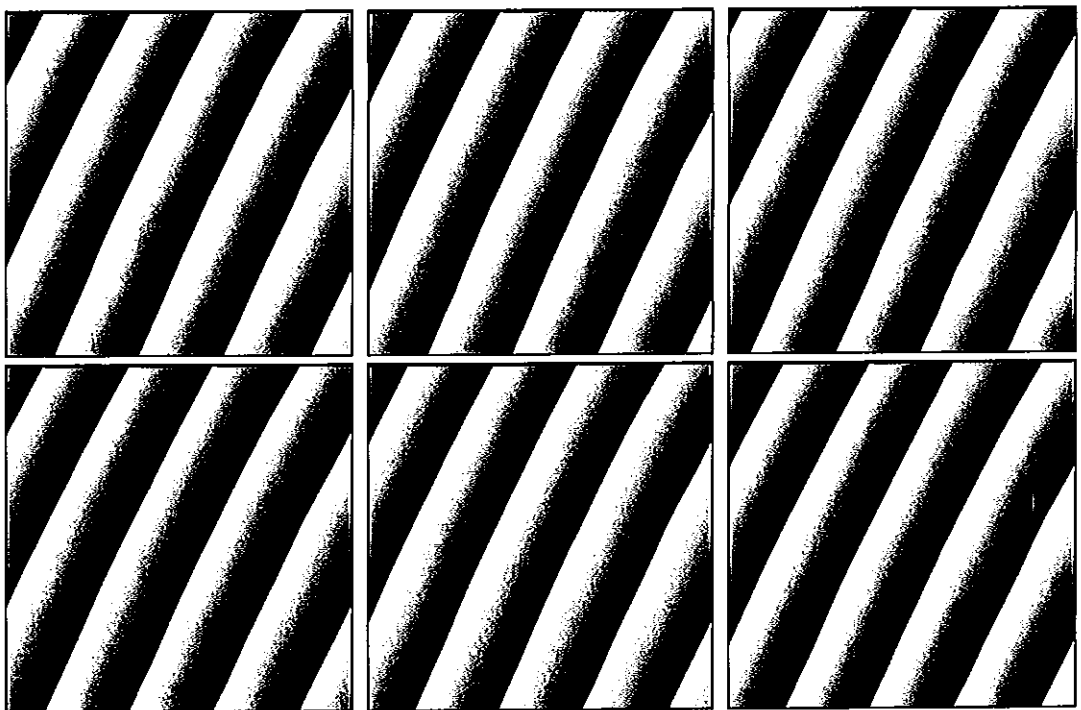
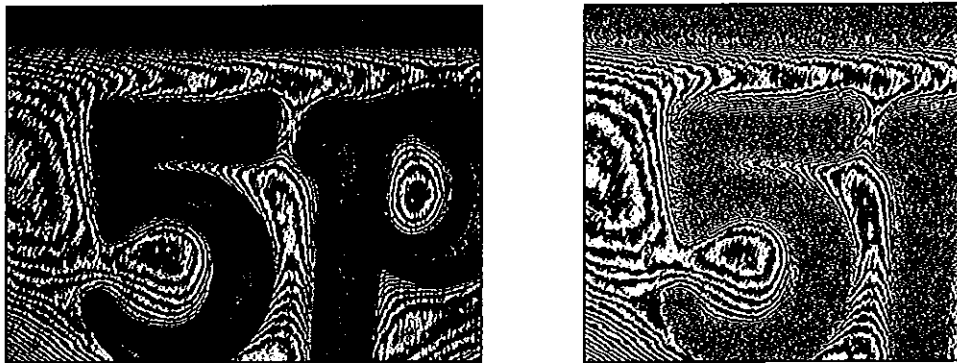


Fig 5.12 Phase maps of mirror surface.

One point to note is how the fringes tend to travel in a left to right direction after each progressive measurement, this may be due to capacitance in the PZT after each measurement. Successive measurements were taken over a time varying from 1 hour to 1 day and it was found that no drift in the phase maps occurred. Though it can be seen that the distance between the corner points is approximately equal.

From figure 5.13 below it is seen that it is impossible to use PSI to profile an optically rough surface with a step height greater than half the wavelength of the source, in this case the surface of a 5 pence piece. It must be noted that it is difficult to properly unwrap the image due to the regions of the image not having fringes.



**Fig 5.13** Sample image with frames on left plus wrapped phase values on right.

As may be seen from the figure above it is important that fringes cover the entire image to properly obtain a surface profile using PSI. In the following figure 5.14, three samples are shown including a mirror and two steel samples of calibrated roughness. Also included in the figure are the wrapped phase maps and unwrapped phase maps plus a 3-D view of the test area.

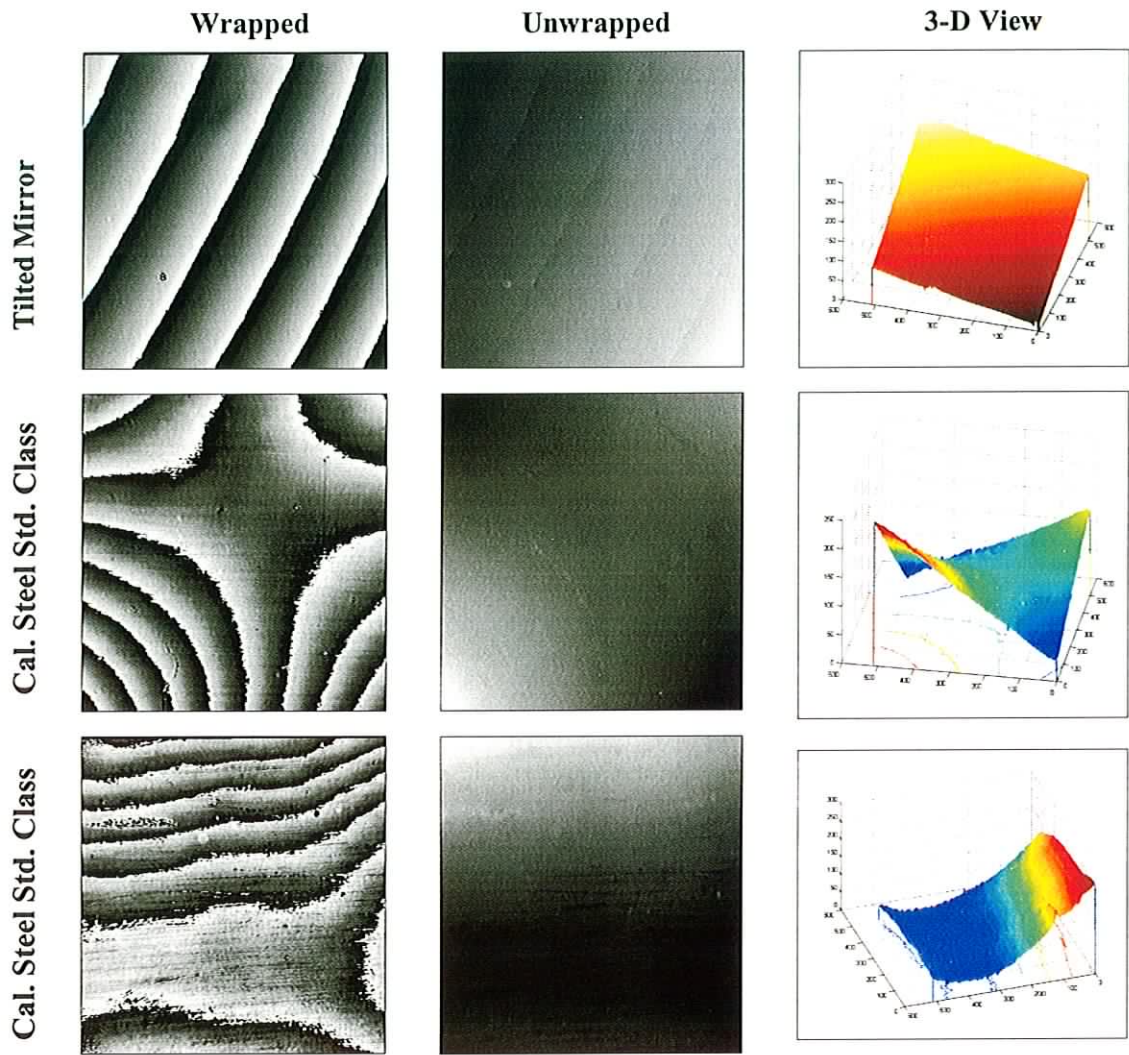


Fig 5.14 Collection of surfaces that were profiled using PSI.

The set of results in figure 5.14 were obtained by profiling using white light phase stepping, three samples were scanned that increased in surface roughness. The figure consists of the wrapped phase map, unwrapped phase map a 3-D view for each of the three samples. The surface roughness (Ra) of the two calibrated steel samples are  $0.0125 \mu\text{m}$  “class 0.5” and  $0.025 \mu\text{m}$  for “class 1.0”. The fringes obtained are due to the tilt subjected to the mirrors. No quantitative measurements could be taken though it was observed how the surface roughness of the samples varied.

## 5.5 Contact Lens

One application of the profiler in industry is in profiling of a contact lens. It is important to be able to quantify edge thickness although manufacturers and researchers usually quote centre thickness and not edge thickness values. Edge thickness is a significant factor when considering the peripheral corneal protection afforded by a contact lens. As it was possible to determine the change in the optical path with the introduction of an opaque material as in figure 4.9, a similar calculation may be accomplished on a contact lens. Though in determining the optical path change introduced by the glass slide coherence peak detection was used, for the contact lens phase stepping was used. Phase stepping may be performed on the lens due to the continuous nature of the fringes in figure 5.16A. It has already been stated that to obtain a suitable profile using PSI it is important that interference fringes cover the entire array of the CCD. Though this is possible with white light it can prove difficult at times and is unsuitable for phase shifting due to the inconsistent phase across the coherence envelope. To combat this problem a laser has been incorporated into the system. The optical configuration remains the same though now it is possible to easily attach the laser onto the stage seen from figure 5.15. With the laser installed it allows fringes to appear across the entire image plane. Therefore, as long as the gradient change is continuous across the surface it is possible to obtain profiles of the sample.

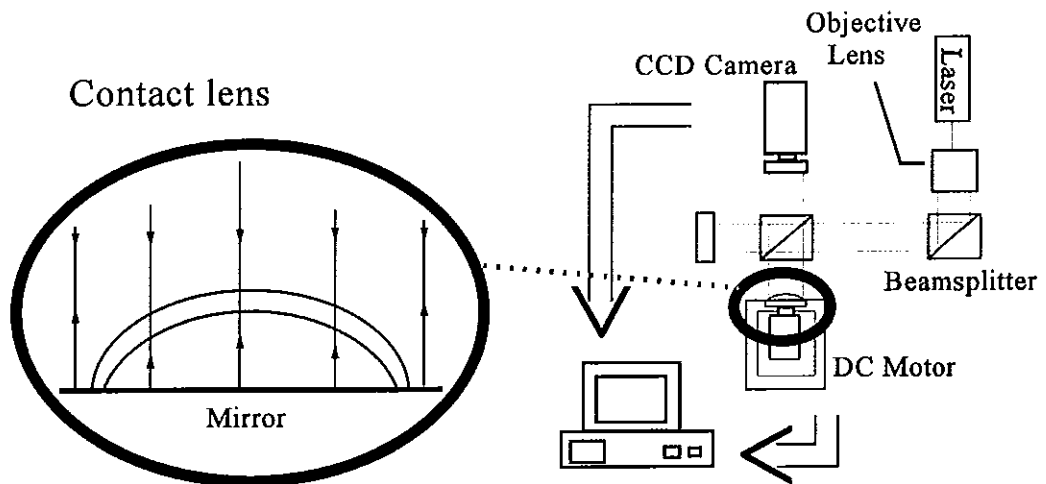
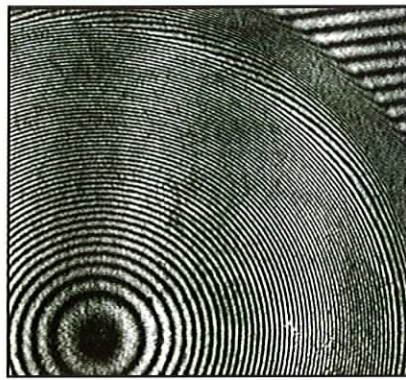


Fig. 5.15. Diagram for the profiling of a contact lens.

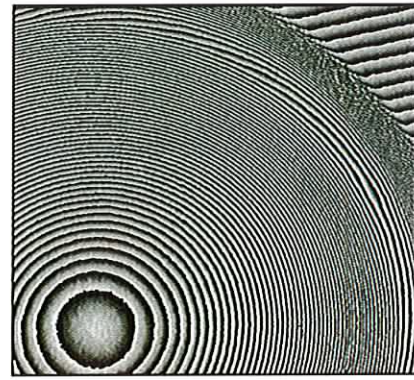


Such an example is seen in figure 5.16. In this example information about a contact lens is being extracted. Variation in the fringes occurs as a result of the change in the optical path introduced by the thickness on the material used in the manufacture of the lens. With a continuous distribution of fringes it is possible to obtain an unwrapped phase map which is used to show the profile of the optical thickness in figure 5.16C.

One important consideration in using phase stepping for profiling the contact lens is the position of the centre of the circular fringes. By placing the centroid fringe in the centre of the contact lens misalignment errors are reduced and the phase stepping program may be started. The problem is overcome by asking the user to select at least three points on the circumference of the contact lens. From these 3 points it is possible to find the centre of the contact lens. By placing the centroid fringe in the centre of the contact lens misalignment errors are reduced and the phase stepping program may be started.



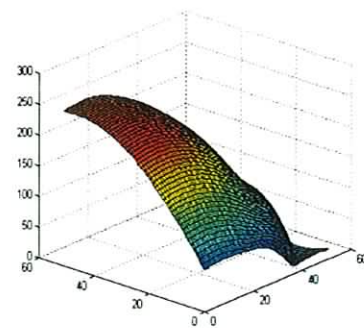
A. Fringes produce by Contact lens.



B. Wrapped map of Phase values



C. Unwrapped map of Phase values.



D. 3D view.

Fig 5.16 PSI application to the profiling of contact lenses

From figure 5.16A it is observed that the fringes have a high spatial frequency with no discontinuities. As the observer moves further from the centre there is an increase in the spatial frequency of the pattern with a low spatial frequency towards the centre. This conforms to the shape of a contact lens, as the surface is relatively flat and thick near the centre and is thinner with a more pronounced slope towards the edges of the lens. Once the unwrapped phase values for the image have been calculated, figure 5.16B, it is noted that a diffraction effect may be observed in the image. The lens was orientated to a different position, with the diffraction effects remaining in both the horizontal and vertical direction. From the unwrapped phase values figure 5.16C it is possible to obtain a 3-D profile for the optical thickness of the contact lens. Using this method it is possible to compare the dimensions of several lenses if the centre has been determined.



Fig 6.1 Main Screen for the profiling system.

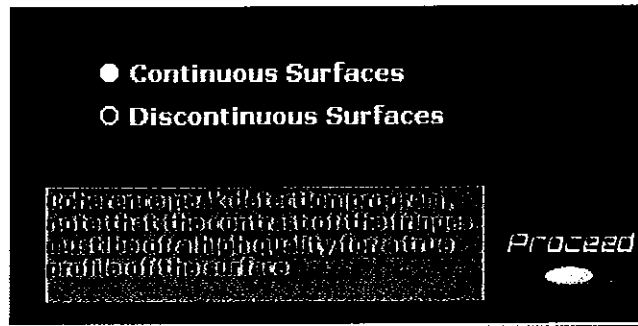


Fig 6.2 Dialog box.

The LabVIEW program that was used for the profiling setup will be discussed in detail in the following section. All user interfaces and controls will also be discussed. The structure of the program is different from many windows based programs as it is sequence based. Once the program has loaded into memory the front panel of figure 6.1 may be seen. By pressing the start button located in the bottom right of the screen a dialog box similar to that of figure 6.2 will be displayed. From this dialog box it is possible to select the type of program that will be used by the profiler in acquiring a profile of the surface. If the surface is a continuous surface with no variations in height greater than  $\lambda/2$  of the illuminating light source the phase stepping program may be used. If there are discontinuities greater  $\lambda/2$  the coherence peak detection program must be run. When the coherence peak detection program has been selected, the panel of figure 6.3 will be displayed from this interface, the start and finish point of the scan will be defined, this may be accomplished by moving the DC motor to the relevant position. It is best to select the finish point followed by the start point as the DC Motor will not have to move far to the start position to commence a scan. Note that once both controls have been pressed the program will continue to the scanning segment of the program. The step size, velocity and acceleration of the DC Motor may be defined by their individual controls. If for any reason the Motor does not seem to be responding to the Movement control "Move(+)" or "Move (-)". The "Init Table" control should be pressed, all start up configuration settings will be set to default and the motor should work as a result.

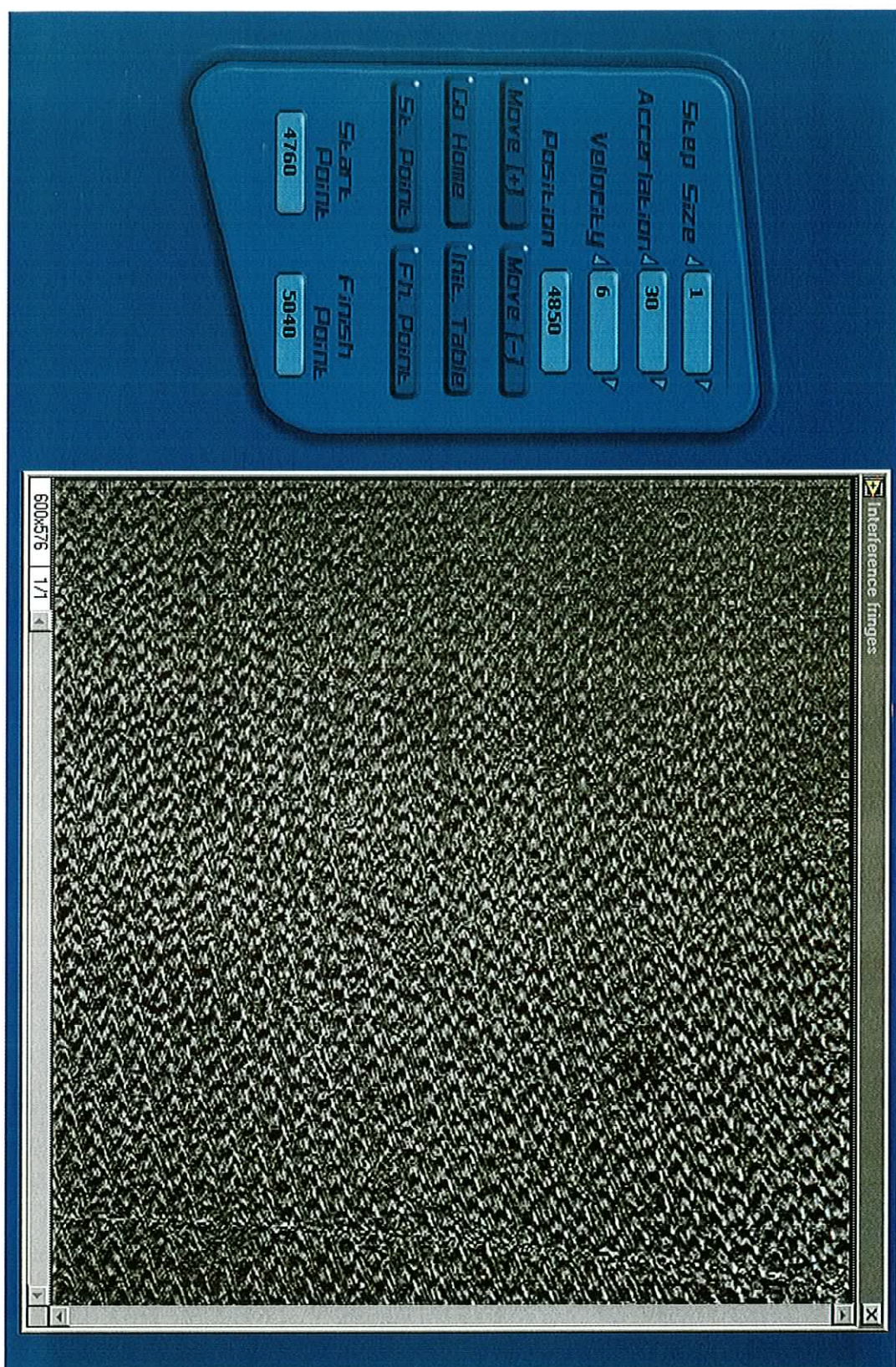


Fig. 6.3 Coherence Peak Detection program, defining start and finish points.

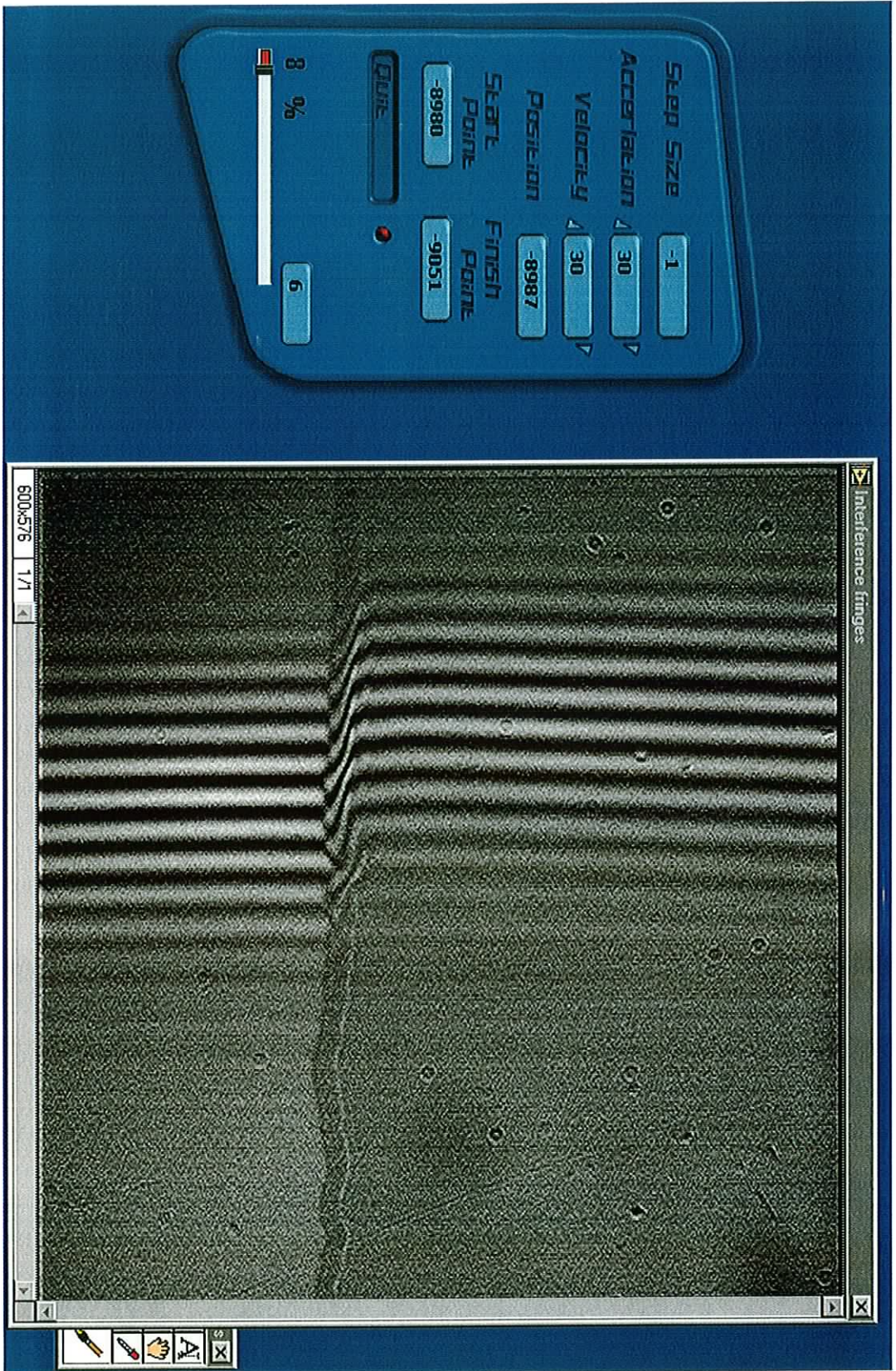


Fig 6.4. User interface for Coherence Peak Detection program.

Once the start and finish positions have been defined for the scan the coherence-scanning interface will appear figure 6.4. The program will scan between the start and finish position with a step size that has been calculated, "Step Size". The position of the DC Motor will also be displayed with a progress bar to show the amount of scan completed. Once the scan is completed two images will be displayed, the maximum modulation frame location and minimum modulation frame location. The user then has three options, to save the maximum modulation frame locations, to save the minimum modulation frame locations or to quit the program without saving.

If the phase stepping program is to be used continuous surfaces must be selected, as in figure 6.5.

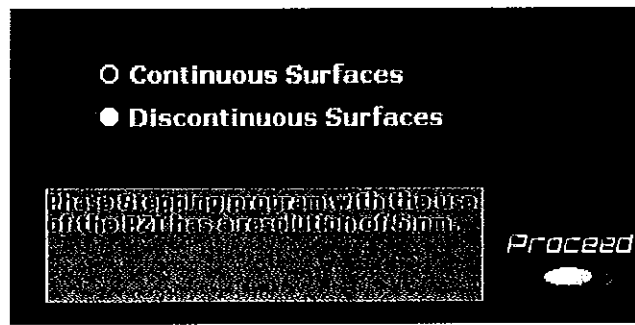


Fig 6.5 Dialog box for phase stepping selection.

After the selection of the continuous surface the user is given two options as in figure 6.6 to calibrate the system to find the step voltage to move  $\lambda/4$  or to proceed to the phase stepping program as in figure. 6.7 if the step voltage is known already.

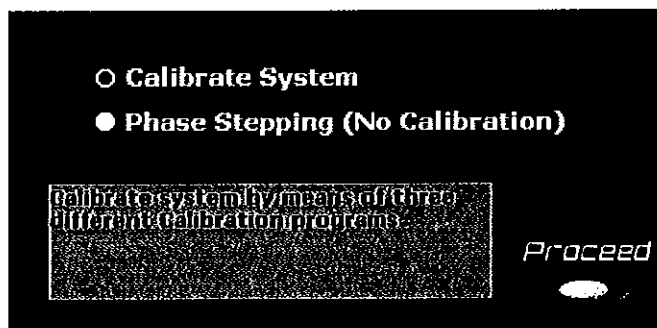


Fig 6.6 Dialog box to calibrate the profiler

By calibrating the system the user has the choice of three-calibration programs fringe detection (peak) as in figure 6.8, fringe detection (curve) as in figure 6.9, frame subtraction as in figure 6.10. By selecting one the calibration program will load into memory and proceed in obtaining the calibration voltage.

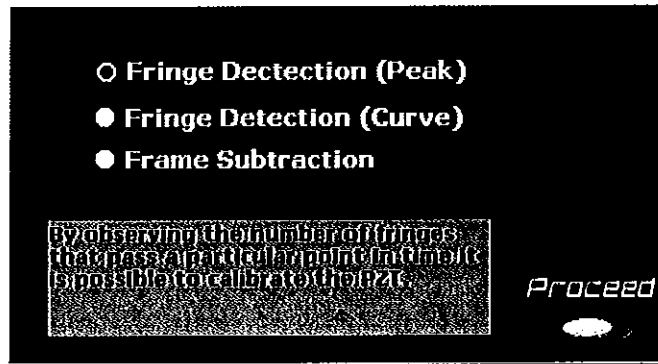


Fig 6.7 Calibration Methods.

For all three methods the voltage step, starting voltage and final voltage may be defined and once these parameters are entered the start control must be pressed for the program to continue scanning for the calibration voltage. Once the process is complete and the voltage step determined the control process must be activated for the program to start the phase stepping part. Note that in the program peak detection and fringe modulation the charts that appear to the right of the program determine the calibration voltage. By selecting one of the LED's to the right of the chart, figure 6.8 or figure 6.9, the value of the calculated voltage will be used to find an average value for the calibrated voltage.

The other control to note is the "first sample" and "second sample" that appear on the interface for the fringe modulation program. These controls select the region on the chart that is to be taken as the sample region in calculating the calibration voltage.



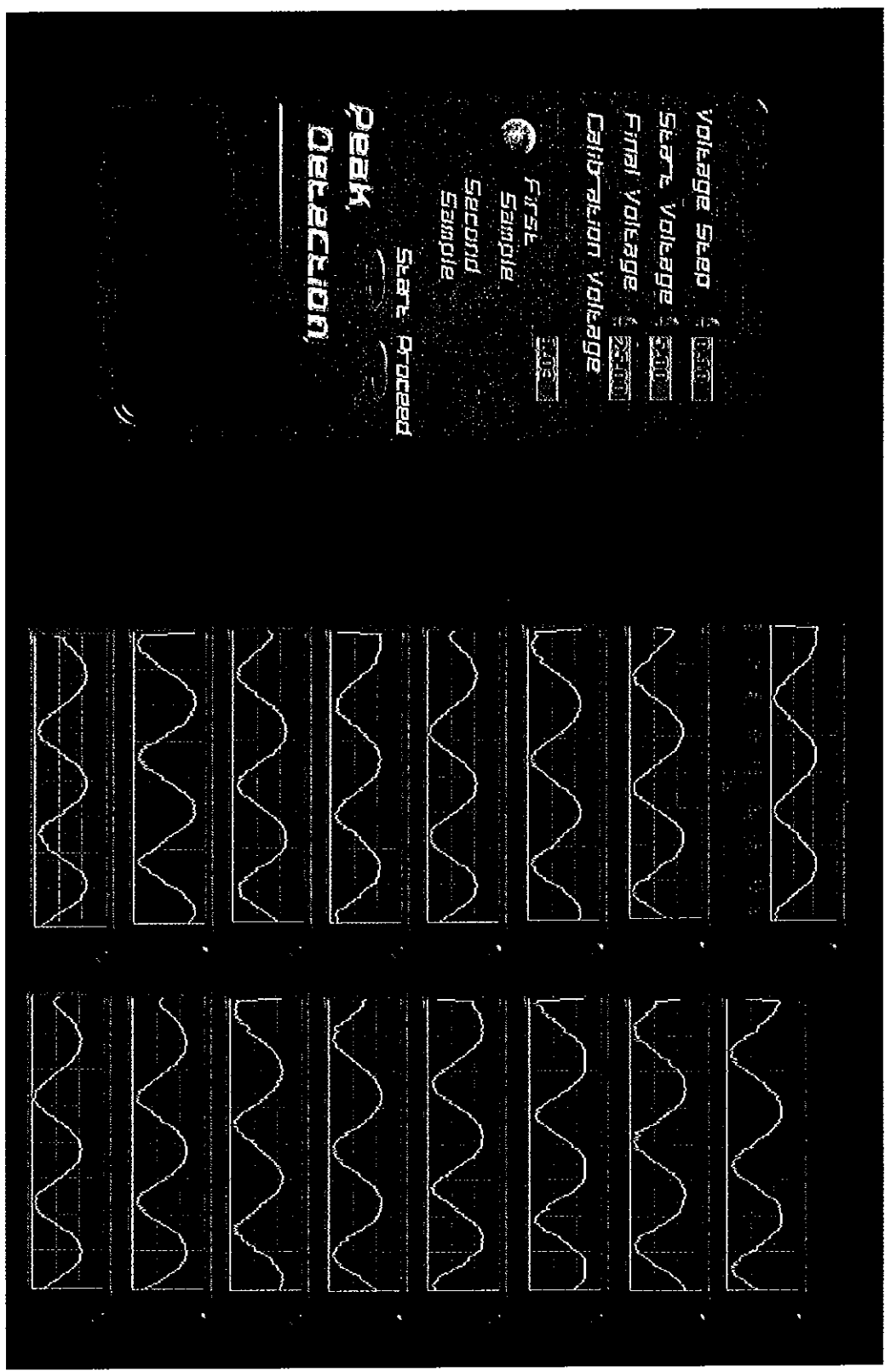


Fig 6.8 User interface for Peak Calibration.

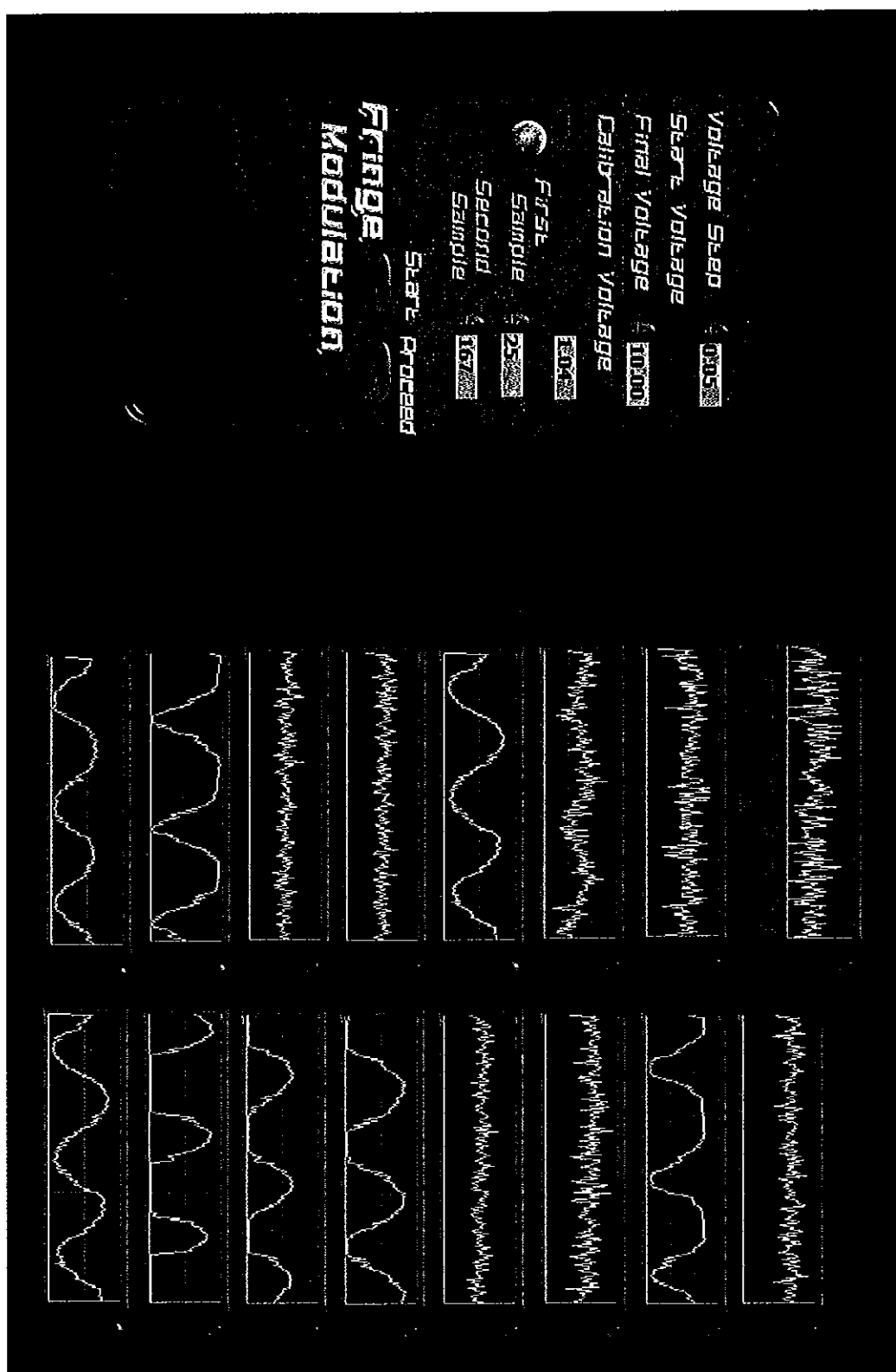


Fig 6.9 User interface for Fringe Modulation.

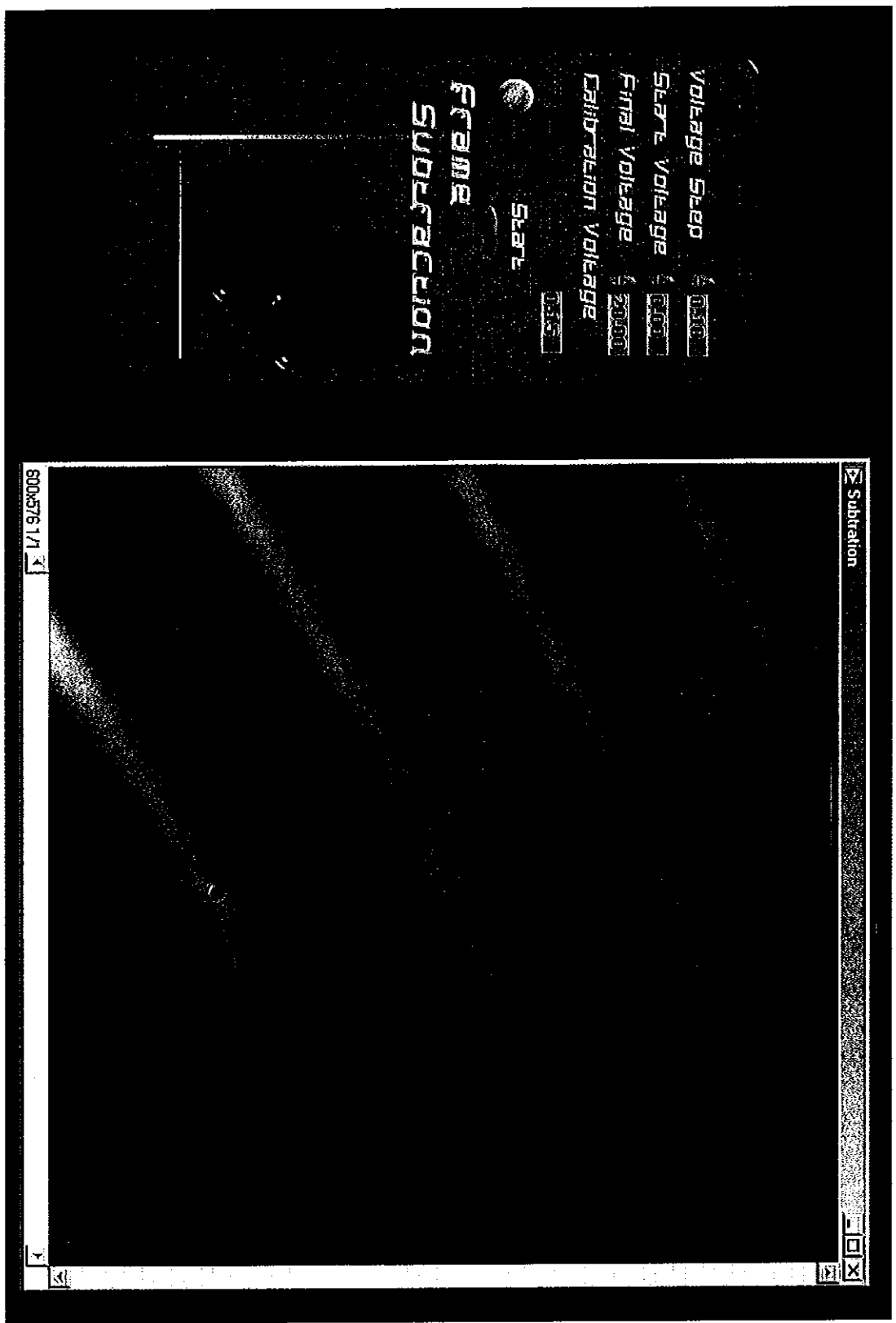


Fig 6.10 User interface for Frame Subtraction.

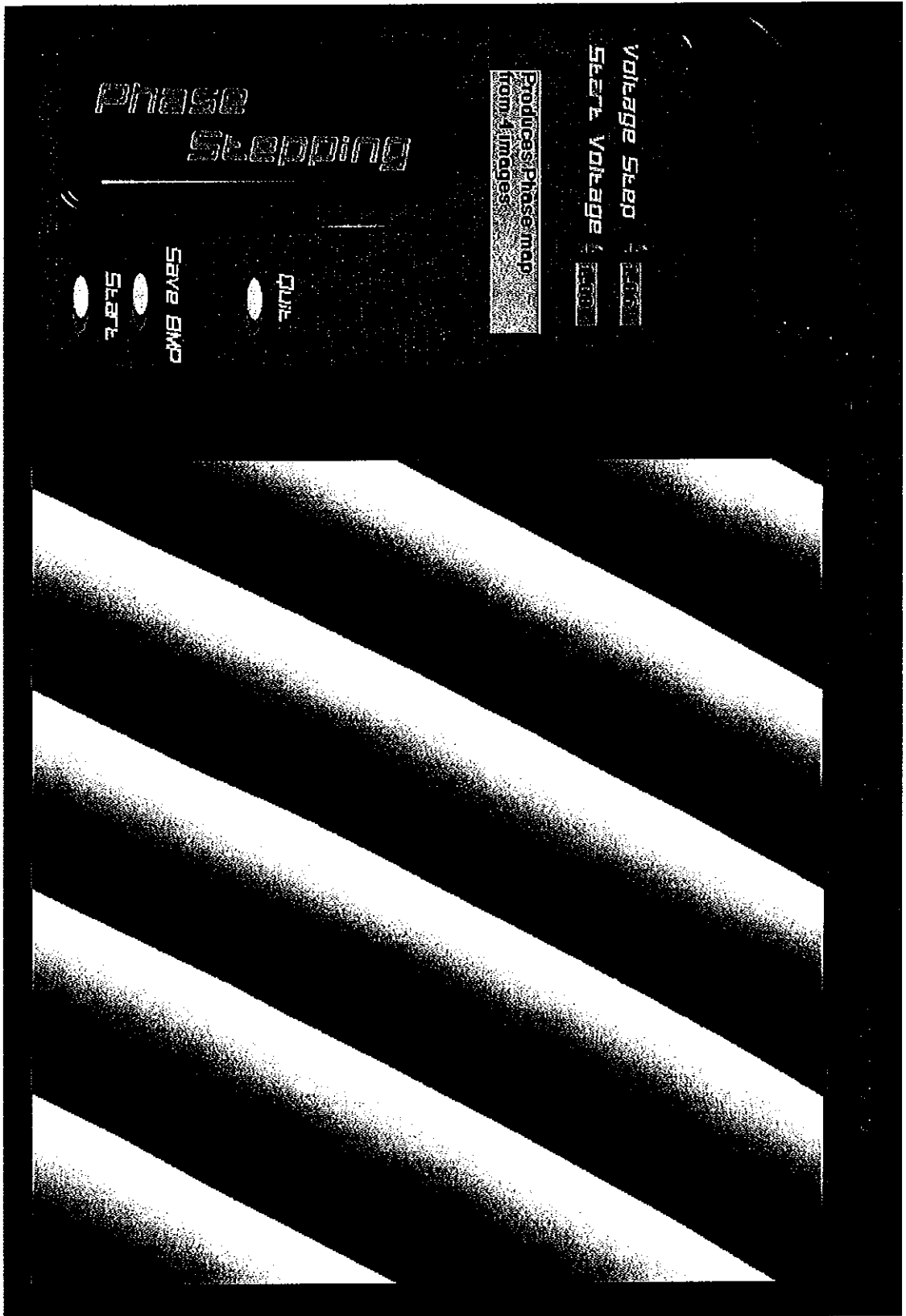


Fig 6.11 User interface for Phase Stepping program.

Once the calibration voltage has been determined the phase stepping program is loaded, note that the calibration voltage may be changed to any desired value before the scan is to take place as in figure 6.11. Though this value may be no greater than 6.25 volts as the program will terminate when the voltage reaches 25 volts. When the program has finished the phase map may be displayed with a histogram of the phase values obtained by the PZT. The user is then given the option to save the phase map as a grey scale map and text file.

One other program was written to make data analysis of step heights much easier to measure. From figure 6.12 the interface of the program may be seen, the user may make a line profile measurement or a histogram measurement to determine the height of a step or discontinuity. Once a line profile has been acquired the profile may be seen in the upper left corner of the screen. By moving the green and red spacers to location of the step it is possible to find the height in pixels. This measurement may also be carried out as an area measurement if 2 rectangular areas are defined. Using the histogram the average intensity is calculated for all values inside the confines of the rectangles. By subtracting the two values from one another is also possible to determine the height difference in pixels between the two regions.



Fig 6.12 User interfaces for Data Analysis program.

## CHAPTER 7: CONCLUSIONS

One of the objectives of this research project was to develop a system for industrial use, further improvements and amendments would need to be introduced for the system to become a viable solution for industry. One of the distinct advantages of the current system is its' portability, however, to bring the system out of the laboratory and into industry an isolation platform would need to be designed to ensure that the profiling system would be immune to external influences such as vibrations and fluctuation in the air temperature surrounding the instrument. Ideally the isolation platform would incorporate the white light profiling system and a mounting platform that could hold the test pieces as they are being scanned by the instrument. Vibration effects would be reduced as the mounting platform and profiling system are isolated and experience equivalent vibrations from the local environment. To limit external influences another improvement would be to construct an enclosed shell surrounding the optics of the profiler to reduce thermal currents. This would help to reduce fringe flicker though would not eliminate the effect as one of the arms of the interferometer would still be exposed to the environment.

At the moment the system has a magnification of  $\sim 1.7X$  with a working distance of 60mm though with a smaller beamsplitter and the beamsplitter positioned closer to the camera lens this range could be extended to 80mm. The vertical resolution of the system is 5nm for phase stepping with a minimum resolution of  $0.06 \mu\text{m}$  possible using the coherence peak detection. The system is fully automatic using programs designed and written in LabVIEW in acquiring the profiles of surfaces though fringes must be in the plane of view for these profiles to be obtained. Due to the inherent magnification of the imaging optics the system has a lateral or spatial resolution of approximately  $4 \mu\text{m}$  which corresponds to a field of view of  $3\text{mm}^2$ . The objectives laid out at the beginning stated that a lateral resolution of  $1 \mu\text{m}$  and a working range of approximately 100 mm were needed. With the current optical setup these specifications would not be possible though with the addition of a CCD camera with a chip size  $< 2\mu\text{m}$  a lateral resolution of  $1 \mu\text{m}$  would be achievable. The current CCD chip size is  $6.50 \mu\text{m}$ . From tests carried out on the instrument it was shown that it would not be possible

to profile a slope not greater than  $0.904^0$ . This is due to the amount of light that is reflected back onto the array of the CCD camera.

Though no quantitative analysis of results were shown for the instrument in its laboratory setup it was shown that the instrument was more than capable of measuring surface heights. Using the profiler a step height of a silica sample was found to be  $0.84\ \mu\text{m}$ , this compares well as the calibrated sample had a step of  $0.81\ \mu\text{m}$  though there is a difference of approximately 3 % in the measured reading and the actual value. One of the reasons for this difference is that the DC motor repeatability is  $2\ \mu\text{m}$ . In its laboratory setup no quantitative results were carried out on the profiler though if the instrument were being modified for industry more quantitative analysis would need to be carried out using standard profiling equipment such as the stylus profiler or the scanning tunnelling microscope.

With the programs that I have designed and constructed using the LabVIEW programming language it is now possible to acquire profiles of the surfaces in a matter of minutes. The LabVIEW programs controls all aspects of the process involved in acquiring a profile including the acquisition of the intensity values from the frame grabber, the analysis of the acquired data and the displaying of the data in a visible form. In addition to LabVIEW performing data filtering and analysis it carries out the important tasks of controlling the DC motor and controlling the voltage source that drives the piezo-electric transducer.

It can be seen from the results section that the profiler has produced good results on both continuous and discontinuous surfaces, though it is important to add that the quality of the fringes used in the measurement affect the quality of the obtained profiles. With the system in its working setup final alterations to the LabVIEW programs have been made in creating fully executable files. By using LabVIEW it was possible to program the system much faster than using another programming language as all of the programs functions can be quickly and easily modified or changed.

When profiling the contact lens with the white light source it was not possible to obtain fringes across the entire field view of the camera as the slope at the edge of the contact lens was greater than the coherence region of the source. This minor difficulty was overcome



by incorporating a laser source into the white light system, thus making it possible to achieve fringes across the entire field of view of the camera and by using phase stepping interferometer to obtain an optical thickness on the contact lens. The contact lens results show a variation in the optical thickness as the viewer moves from the center to the outer edges of the lens. Two conditions must be met before quantitative results can be given for the lens. Firstly the centre thickness of the lens must be known and secondly the CCD camera would have to be calibrated for distance measurements in the x-y plane.

Improvements that could be made to the current system are few, though an improved imaging system would need to be included on the camera to improve the focus quality of the image under test. Ideally it would be a major benefit if LabVIEW could carry out the unwrapping of the phase maps; by integrating an unwrapping algorithm into the program the entire procedure of profiling would exist in one complete and compact program. All phase maps had to be transferred to a remote machine and be individually unwrapped which was a time consuming process.

As outlined in chapter 4-phase stepping interferometer has the drawback that harmonic vibrations due to movement i.e. piezo-electric transducer affect the system and time must be allowed to elapse to dampen these vibrations. Therefore the preferred option in all modern phase measuring systems is the phase shifting interferometer technique.

## REFERENCES

1. F. A Jenkins, H. E. White, "Fundamentals of Optics" Fourth Ed., McGraw-Hill International Editions.
2. Hecht Optics Second Edition, Addison Wesley Publishing Company 1987.
3. S. Tolansky, "An Introduction to Interferometer", Longmans, Green & Co. London (1955).
4. Chunli Bai "Scanning Tunnelling Microscopy and its Application," Shanghi Scientific & Technical Publishers
5. D. J. Whitehouse, "Surface Metrology," Meas. Sci. Tech.
6. H. Takasaki, "Moiré Topography", Applied Optics, 9, 1467-1472, (1970).
7. J.C Wyant "Interferometric Optical Metrology : Basic Principles and Systems" Laser Focus May (1982).
8. H. J. Caulfield, "Handbook of Optical Holography" (New York: Academic Press) 1979.
9. M. Kujawinska, D.W Robinson "Multichannel phase-stepped holographic interferometer" Applied Optics, 27, 2 (1988).
10. C. Wykes, "Use of Electronic Speckle Pattern Interferometer(ESPI)in the measurement of Static and Dynamic Surface Displacements," Opt. Eng. 21, 400 (1982).
11. Binnig, G., et al., Surface studies by scanning tunnelling microscopy, Physical Review Letters, 49 (1), p. 57-61 (5 July 1982).
12. G. Binnig, C. F. Quate, and Ch. Gerber, Phys. Rev. Lett. 56, 930 (1986).
13. J.C Wyant "Optical Profilors for the surface roughness" SPIE Measuremnt and Effects of Surface Defects and the Quality of Polish Vol. 525 174-180 (1985).
14. G. Makosch, B. Drollinger, "Surface profile measurement with a scanning differential ac interferometer" Applied Optics Vol. 23(24) 4544-4553 (1984).
15. J. H. Bruning, D. R. Herriot, J. E. Gallaghe, D. P. Rosenfield, A. D. White, D. J. Brangaccio, "Digital Wavefront Measuring Interferometer for Testing Optical Surfaces and Lens" Applied Optics 13, 11, 2693-2703 (1985).
16. J. C. Wyant, K, Creath, "Recent advance in interferometric optical testing" Laser Focus/Electro-Optics 11 (1985).

17. Bhushan B, Wyant J.C, Koliopoulos C. L," Measurement of surface topography of magnetic tapes by Mirau Interferometer" *Applied Optics*, Vol 24 No 10 1489-1497 1985.
18. G. S. Kino, S. C. Chim "Mirau correlation scope" *Applied Optics*, 29, 26, 3775-3783 (1990).
19. M Davidson, I Kaufman, "An application of interference microscopy to integrated circuit inspection and metrology," *SPIE*, 775, 233-247 (1987).
20. Obtain the Wyko Specs.
21. J. Schmit, K. Creath "Extended averaging technique for derivation of error-compensating algorithms in phase-shifting interferometer," *Applied Optics* 34, 3610-3619 (1995).
22. P. de Groot , "Derivation algorithms for phase-shifting interferometer using the concept of data sampling window" *Applied Optics* 34,4723-4730 (1995).
23. <http://www.optik.uni-erlangen.de/horst/limit/#2>. Physical limitations
24. Y.Y Cheng J.C Wyant, "Two-wavelength phase-shifting interferometer," *Applied Optics* . 23,4539-4543 (1984).
25. P. J. Caber, "Interferometric profiler for rough surfaces," *Applied Optics*, Vol.32,No.19,3438-3441,(1993).
26. B. Bhushan, J. C. Wyant, C. L Koliopoulos, "Measurement of the surface topograph of magnetic tapes by Mirau interferometer," *Applied Optics*, Vol.24,No.10,1489-1497(1985)
27. G. S. Kino, S. C. Chim "Three-dimensional image realisation in the interferometer microscopy" *Applied Optics*, 31, 14, (1992).
28. P. de Groot , L. Deck "3D Imaging by Sub Nyquist sampling of white light interferogram", *Optical Letters*, Vol 18, 1462-1462. 1993.
29. Seung-Woo Kim, Gee-Hong Kim, "Thickness-profile measurement of transparent tin-film layers by white-light scanning interferometer," 38, 28, 5968-5973, (1999).
30. P. J. Caber, J Stephens, J. Martinek, R. J. Nieman, "A new interferometric profiler for smooth and rough surfaces" *SPIE*, Vol.2088, 195, 1993.
31. P. de Groot, L. Deck "surface profiling by analysis of white-light interferograms in the spatial frequency" *J. Mod Opt.* 42, 389-401 (1995).
32. K. G. Larkin "Efficient nonlinear algorithm for envelope detection in white light interferometer" *J. Opt. Soc. Am. A* 13 832-843 (1996).

33. P. Sandoz, "An algorithm for profilometry by white-light phase-shifting interferometer," *J. Mod. Opt.* 43, 8, 1545-1554 (1996).
34. P. Sandoz, "Wavelet transform as a processing tool in white-light interferometer," *Opt. Lett.* 22, 1065-1067 (1997).
35. A Harasaki, J. Schmit, J.C. Wyant, "Improved vertical-scanning interferometer" *Applied Optics*, 39, 13, 2107-2115 (2000).
36. A. Bartoli, P. Poggi, F. quercioli, B. Tiribilli, "Fast one-dimensional profilometer with a compact disc pickup," *Applied Optics*, 40 7 1044-1048 (2001).
37. K. J. Stout, ed., " three Dimension Surface Topograph : Measurement Interpretation and Application" (Penton Press, London, 1994).
38. Ji-hua Zhang, Lilong Cai, "Profilometry using an optical stylus with interferometric readout" *Meas. Sci. Technol.* 8 (1997) 546-549.
39. M.J. Downs, W.H McGiven, H.J Ferguson, "Optical system for measuring the profiles of super-smooth surfaces" *Precision Engineering* 7 4 211-215 (1985).
40. Lianhua Jin, "Shadow Moiré profilometry using the phase-shifting method," 39, 8, (2000).
41. H.A Gardner and G.G Sward, "Paint testing Manual, Physical and Chemical Examination : Paints, Varnishes, Lacquers and Colors"
42. G.S Spagnolo, D Ambrosini, "Diffractive optical element based profilometer for surface inspection" *Opt. Eng.* 40(1) 44-52 (January 2001).
43. Interferogram analysis D. W. Robinson, G. T. Reid, "Interferogram analysis", Bristol, Institute of Physics Pub., c1993.
44. R. Rodriguez-Vera, M. Servin, "Phase locked loop profilometry," *Opt. Laser Tech.* 26, 393-397 (1994).
45. J. Kozlowski, G. Serra, "Complex phase tracing method for fringe pattern analysis," *Applied Optics*, 38, 11, 2256-2262 (1999).
46. Carrie P, *Metrologia* 2 13-23 1966.
47. Bruning J H, Herriott D R , Gallagher J E, Rosenfeld D P, White A D, and Brangaccio D , *Applied Optics* 13 2639-703 1974.
48. Wyant J C, Creath K, *Laser Focus/Electro-Optics* Nov 118-32 1985.
49. Wyant J C, Shagam R N, *Proc ICO-11 Madrid* 659-62 1978.

50. Y. Surrel, "Design of algorithms for phase measurement by the use of phase stepping," *Applied Optics*, 35,1, 51-60, (1996).
51. Stahl P H, "Review of Phase-measuring Interferometer" *Optical Testing and Metrology III: Recent Advances in Industrial Optical Inspection*, SPIE Vol. 1332 704-719 1990.
52. K. Creath, "Comparison of phase-measuring algorithms in Surface Characterisation and testing," *Proc. Soc. Photo-Opt. Instrum. Eng.*, 680, 19-28, (1986).
53. C. Joenathan, "Phase-measuring interferometer new methods and error analysis," *Applied Optics* 33, 19, 4147-4155, (1994).
54. C. T Farrell, M. A Player, "Phase step insensitive algorithm for phase-shifting interferometry," *Meas. Sci, Technol.*, 5, 648-652, (1994).
55. A. Dobroiu, D. Apostol, V. Nascov, V. Damian, "Self-Calibrating algorithm for three-sample phase-shift interferometer by contract levelling," *Meas. Sci, Technol.*, 9, 744-750 (1998).
56. B. K. A. Ngoi, K. Venkatakrishnan, N. R. Sivakumar, "Phase-shifting interferometer immune to vibration," *Applied Optics*, 40, 19, 3211-3214, (2001).
57. H. van Brug, "Phase-step calibration for phase-stepped interferometer," *Applied Optics*, 38, 16, 3549-3555, (1999).
58. P. L. Wizinowich, "Phase shifting interferometer in the presence of vibration a new algorithm and system," *Applied Optics*, 29, 22, 3217-3279, (1990).
59. P. de Groot, "Deviation of algorithms for phase-shifting interferometer using the concept of a data-sampling window" *Applied Optics*, 34,22, 4723-4730, (1995).
60. C. T Farrell, M. A Player, "Phase step measurement and variable step algorithm in phase-shifting interferometer," *Meas. Sci, Technol.*, 3, 953-958, (1992).
61. K. Creath, "Phase measuring interferometer techniques," *Prog. Opt.* 26, 349-93, (1988).
62. J. van Wingerden, H. J Frankena, C Smorenburg, "Linear approximation for measurement errors in phase shifting interferometer," *Applied Optics*, 30, 2718-2729, (1991).
63. Q. Kemaο, S. Fangjun, W. Xiaoping, "Determination of the best phase step of the Carre algorithm in phase shifting interferometer," *Meas. Sci, Technol.*, 11, 1220-1223, (2000).
64. Hariharan P, Oreb B. F, Eiju T, "Digital Phase Shifting interferometer: a simple error-compensating phase calculation algorithm", *Applied Optics*, 26, 13, 2504-6, 1987.

65. Schwider J, "Homogeneity testing by phase sampling interferometer," *Applied Optics*, Vol. 24, 3059-61, 1985.
66. Vikhagen E, "Nondestructive testing by use of TV holography and deformation phase gradient calculation," *Applied Optics* 29 137-44
67. Creath K, "Phase-shifting speckle interferometry", *Applied Optics* 24, 3053 (1985).
68. D. W. Robinson, "Phase unwrapping methods" in *interferogram analysis Analysis: Digital Fringe Pattern Measurement Techniques*, D. W. Robinson and G. T. Reid eds. (Institute of Bristol 1993).
69. K. Itoh, "Analysis of phase unwrapping program," *Applied Optics*, 21, 2470, (1982).
70. A. Spik, D. W. Robinson "Investigation of cellular automated method for phase unwrapping and its implimentation on an array processor," *Opt. Laser Eng.*, 14, 25-37, (1991).
71. Huntley J.M. and Saldner, H.O. "Error reduction methods for shape measurement by temporal phase unwrapping", *J.Opt. Soc. Am. A* 14 (12) 3188-3196 (1997).
72. R. J. Green, J. G. Walker, "Phase unwrapping using a prior knowledge about the band limits of a function," *Proc. Soc. Photo-Opt. Instrum. Eng.*, 10, 26-43, (1988).
73. J. Strand, T Taxt, "Performance evaluation of two-dimensional phase unwrapping alorithms" *Applied Optics*, 38, 20, 4333-4344, (1999).
74. P. Ettl, K Creath, "Comparison of phase-unwrapping algorithm by using gradient of first failure," *Applied Optics*, 35, 25, 5108-5114, (1996).
75. Sandoz, "An algorithm for profilometry by white-light phase-shifting interferometer," *J. Mod. Opt.* 43, 8, 1545-1554 (1996).
76. B. Bove, "Development and optimisation of optical intererometric techniques for surface metrology" Thesis submitted to the department of pure and applied physics university of Dublin, June 1999.
77. T. Dresel, G. Hausler, H Venzke, "Three-dimensional sensing of rough surfaces by coherence radar", *Applied Optics*, 31, 7, 3919-3925, (1992).

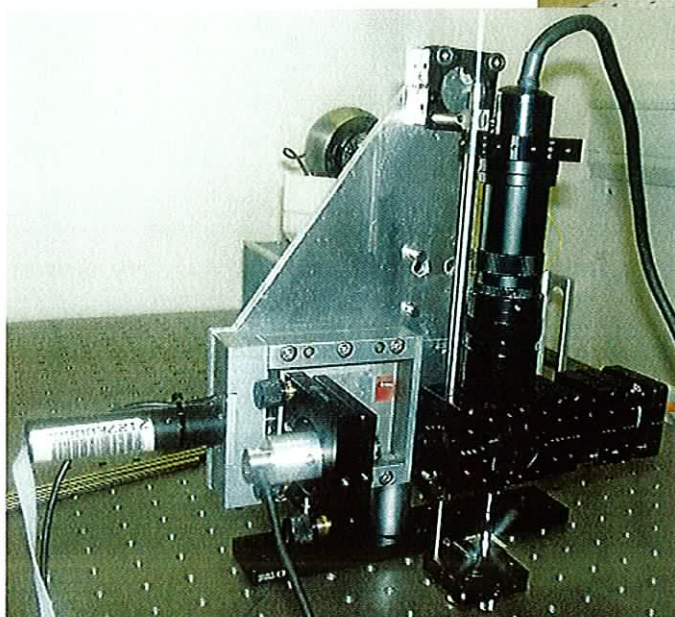
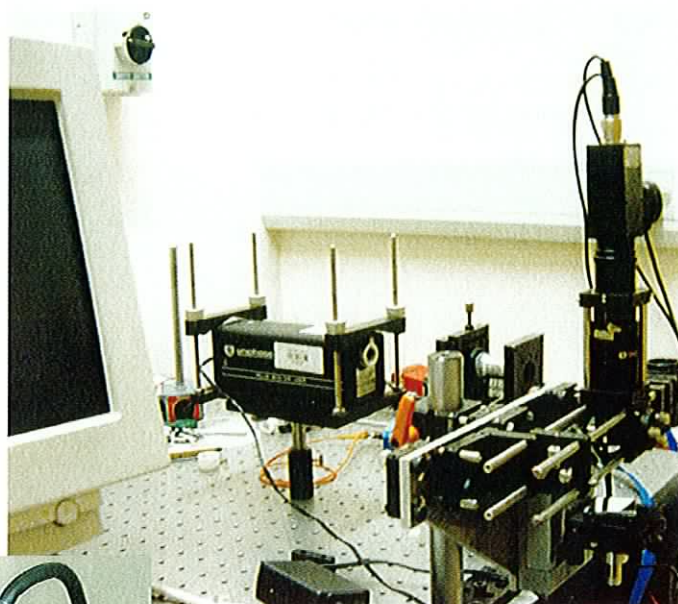
## APPENDIX A- EQUIPMENT

DC M-125.10 motor  
25mm Travel Range  
Resolution 0.06 $\mu$ m

C-842.40 DC Motor Controller Board  
ISA Bus Compatible  
Simultaneous Control of up to 4 DC  
Servo Motors

Piezo-electric Transducer  
Maximum Limit 15  $\mu$ m-145 Volts

PZT Driver  
Thurby Thandar Programmable  
TSX3510P  
Range 0-35 Volts  
Resolution 0.01mV



Camera- Pulnix, Model No.  
PE2013/PE2013L  
Imaging format-CCIR  
Pixel Array-752(H) $\times$ 582(V)  
Pixel Chip Size(mm)-  $\times$ 6.50(H) $\times$ 6.26(V)  
Pixel Cell Size( $\mu$ m)-  $\times$ 4.88(H) $\times$ 3.63(V)

Silver Plane Mirrors  
Front surface rectangular  
Surface roughness  $\lambda/100$

Interference filter  
Transmittance 40%  
Spectral Line - d/D  
Element Laser – He/Na

The above diagram shows two different orientations that the system was tested in. Also included is a list of all the major components that were used in its construction. The image in the top right shows the DC motor in the object arm of the interferometer with the image in the bottom left showing the DC motor in the reference arm of the interferometer. Included in the setup of the top right image is a laser and objective lens that were used in characterising the surface of the contact lens.